Alternative Fuels and Combustion Strategies for Emissions Reductions: Experimental Studies of C3 Fuel Kinetics

by

Miles Burnett

A dissertation submitted in partial fulfillment
of the requirements for the degree of
Doctor of Philosophy
(Mechanical Engineering)
in the University of Michigan
2022

Doctoral Committee:

Professor Margaret S. Wooldridge, Chair
Dr. Nabiha Chaumeix, Centre National de la Recherche Scientifique (CNRS)
Professor Venkat Raman
Professor Angela Violi

Miles Burnett

maburn@umich.edu

ORCID iD: 0000-0003-4870-6283

Dedication

To my parents,
for their unwavering love and support,
and setting an example that made me the man I am today.

Acknowledgements

I would like to begin by expressing my deepest appreciation to my advisor, Professor Margaret Wooldridge, for her guidance and support through research challenges, in my professional development, and as a personal mentor. I could not have asked for a better advisor as I worked through my doctoral studies, and I am incredibly grateful for the opportunity she provided me to join her lab and have experiences that allowed me to grow immensely as both a researcher and person. I would also like to thank Dr. Nabiha Chaumeix, who graciously welcomed me into her lab, oversaw my work conducted at the Centre National de la Recherche Scientifique – Institut de Combustion, Aérothermique, Réactivité et Environnement (CNRS-ICARE) in Orléans, France, and helped me navigate the difficulties in both returning to the U.S. at the start of the COVID-19 pandemic and coordinating my return in 2021 to complete our work. I was incredibly lucky to work as a researcher at CNRS-ICARE twice, and my wonderful experience there would not have been possible without her support. Additionally, I would like to thank Professor Angela Violi and Professor Venkat Raman for serving on my committee and providing valuable insight and feedback in refining my research and its presentation in this dissertation.

No research is conducted in a vacuum (especially when leak checking the RCF), and none of this work would be possible without my many lab mates and mentors that have helped me along the way. I would like to recognize the support and friendship of my lab mates at the University of Michigan: Dr. Rachel Schwind, Dr. Mario Medina, Dr. Luis Gutierrez, Dr. Ripudaman Singh, Dr. Cesar Barraza-Botet, Dr. Dimitris Assanis, Shannon Clancy, Sylvia Meng, John Kim, Varun Chakrapani, Nanta Sophonrat, Jenna Stolzman, Chenyi Zhu, and Aksel Ahituv. I would also like to recognize my lab mates and friends at CNRS for being incredibly welcoming to me during my time there: Ayan Mousse-Rayaleh, Alka Karan, Letícia Piton, Fabián Cano, Anthony Roque, Alaa Hamadi, Ricardo Castro, Antoine Mouze-Mornettas, and Héctor Campos. I also owe several thanks to those who have given me valuable mentorship and research advice throughout my doctoral program: Prof. Andrew Mansfield, Dr. Scott Wagnon, Dr. Andrea Comandini, and Dr. Said Abid. I would also like to thank the additional contributors to portions of this work: Charles

Daniels for his work on the two-zone model development and Liu Wei and Professor Zhi Wang for their experimental contributions from Tsinghua University. Additional thanks to the wonderful staff throughout the UM ME department in the ASO office, ME-IT, and facilities for their support.

Thank you to all the incredible friends that I have made from Mississippi, at the University of Oklahoma, and during my doctoral studies at the University of Michigan for their friendship outside of the lab, willingness to help me work through any problem, big or small, and always being there for an entertaining conversation.

Finally, I would not be who I am or where I am today without the endless love of my family. My mother and father, Cindy and Bill, and younger brother, Drew, have always been there for me and provided guidance and support throughout every stage of my life. I love you and would not be where I am today without you. Mom and Dad, thank you for being the best parents Drew and I could have possibly asked for.

Funding Acknowledgements

I would like to acknowledge the generous financial support of the U.S. Department of Energy Basic Energy Sciences, Award Number DE-SC0019184; the National Science Foundation, Award Number 1,701,343; and the National Science Foundation INTERN program. Additionally, I would like to acknowledge the generous support of the lab at CNRS-ICARE for funding my transportation costs to Orléans, France.

Table of Contents

List of Tables

List of Figures

List of Appendices

Abstract

Identification of alternative fuel sources and combustion strategies are crucial to realizing emissions reductions in the global power and transportation sectors necessary to combat climate change. The use of alcohols produced from biomass, low temperature (<1300 K) combustion, and propulsion systems driven by detonation are three potential emissions reduction strategies driving recent research topics in combustion science. Each faces specific implementation challenges requiring improved understanding of the underlying combustion science to achieve their long-term emissions reduction potential.

This dissertation presents fundamental studies of the chemical and physical mechanisms of three fuels of interest to advanced power and propulsion sectors. The studies leverage novel experimental methods to fill gaps in the knowledge of each fuel's chemistry or gas dynamics. The first study focuses on understanding the reaction pathways important during *iso*-propanol (a potential biofuel with advantages in low-carbon transportation applications) pyrolysis at low temperatures and moderate pressures. The technical approach used the University of Michigan rapid compression facility (UM-RCF) to achieve desired state conditions while fast-gas sampling and gas chromatography quantified concentrations of *iso*-propanol and seven stable intermediate species at temperatures of 965 – 1193 K and pressures of 4.4 – 10.0 atm. The results validated dominant decomposition reactions but identified discrepancies in expected rate of *iso*-propanol decomposition at the highest temperature and in the expected branching pathways producing and consuming ethane at the lowest temperature.

The second and third studies focused on ignition characteristics of propane at low temperatures and moderate pressures. Propane is an important fuel for heating and processing and an important alkane for developing hierarchical combustion chemistry. Two studies on propane ignition behavior within the UM-RCF and Tsinghua University rapid compression machine (TU-RCM) were conducted to measure the impacts of localized thermal gradients and thermal boundary layers on ignition characteristics both within and outside of the negative temperature coefficient (NTC) region for temperatures from 744 – 1070 K and pressures from 8.9 – 25.4 atm at equivalence ratios of ϕ = 0.25, 0.5, and 1.0. High speed imaging and pressure measurements were used to identify ignition characteristics and their impact on ignition delay times (IDT). Inhomogeneous, or “weak/mixed”, ignition exhibited meaningful differences between observed IDT and model predictions. Imaging data of thermal boundary layers spanning the NTC region appear to show a stratification of ignition behavior within the reaction chamber but did not demonstrate notable irregularities when compared to model predictions. The results reveal the complexity of interpreting experimental data in weak ignition regimes and complications introduced by NTC behavior.

Lastly, the study of *iso*-propyl nitrate (IPN) as a sensitizer for detonation of propane focused on quantifying the detonation transition characteristics of IPN and propane mixtures, which is important for development of practical pressure-gain engines. The experiments were conducted using the detonation tube at the Centre National de la Recherche Scientifique (CNRS) in Orléans, France. Wave speeds, detonation cell sizes, and critical conditions required for detonation were quantified over a range of conditions. The data showed the addition of 10% IPN increased sensitivity to detonation of propane-oxygen mixtures in both dilute and non-dilute mixtures by decreasing the critical conditions by ~5% and ~10% respectively and decreasing the cell size observed in non-dilute mixtures by ~20%, demonstrating that IPN is a promising detonation sensitizer for applications relevant to the development of pulse and rotating detonation engines.

Chapter 1: Introduction

1.1 Background and Motivation

The reduction of carbon emissions in the global power and transportation sectors is one of the most urgent changes necessary to combat climate change [1]. Global energy use is expected to increase by nearly 50% in the coming decades, with much of the growth concentrated in non-OECD (Organization for Economic Co-operation and Development) developing economies, and, despite the rapid growth in renewable energy expected in the coming decades, the energy and transportation sectors are expected to remain reliant on carbon emitting, combustible fuel sources during that time [2,3]. The continued reliance on combustible fuels creates a demand for alternative fuels and combustion strategies that operate at higher efficiency while reducing emissions of CO_2, particulates, and harmful pollutants [4].

The requirements for next generation combustible fuels and energy generation systems that will meet these demands are being investigated by a robust community of combustion scientists examining a wide range of potential emissions reduction and efficiency improvement strategies. Research topics within the field of combustion are incredibly wide ranging but with the same end goal of creating a more sustainable global energy generation system. Advances being explored include research on fuel production methods [4,5], combustion behavior [6], engine design and optimization [7], fundamental kinetics [4,8], and improving computational simulations of combustion systems [9], among many others. Each of these areas include associated topics that cannot all be adequately addressed in this dissertation but provide valuable results and guidance for future energy generation system recommendations and research topics.

A key area of combustion research focuses on understanding the chemical kinetics of fuels at typical operating conditions for energy generation systems, such as gas turbines or internal combustion engines. Chemical kinetics, in combination with thermodynamics, control key aspects of combustion behavior, including fuel ignition properties, flame speeds, and pollutants formed during the ignition process [10]. A detailed understanding of the kinetics driving combustion of different fuels is important to developing chemical kinetic mechanisms that are used to predict fuel behavior under a range of thermodynamic conditions. The accuracy of these mechanisms is particularly important for simulations when designing combustion systems using reactivity-controlled kinetics, such as homogenous charge compression ignition (HCCI), reactivity controlled compression ignition (RCCI), and premix charge compression ignition (PCCI) [11], where the fuel kinetics are the main driver of the combustion process through autoignition. Additionally, it is important to predict the products that may be formed during the combustion process such as NO_x, CO, CO_2, and unburned hydrocarbons. Therefore, a robust collection of experimental data that can inform the design of accurate chemical kinetics mechanisms for a wide range of fuels and thermodynamic conditions is essential fundamental knowledge needed to design efficient, low polluting energy generation systems that can meet required emissions reduction goals.

While combustion as a science has been studied for centuries, there are still gaps in our knowledge that require further study. A major area of interest is on the reactions controlling fuel consumption at low temperature conditions that are critical to high efficiency/low emission combustion. At low temperature conditions, combustion behavior can exhibit unusual characteristics that make it difficult to study such as negative temperature coefficient (NTC) behavior where an increase in temperature counterintuitively leads to a decrease in reactivity due to changing reaction pathways. In addition to the complex chemistry, the longer test times associated with LTC studies make the experimental work more susceptible to effects from heat loss to the surrounding area and thermal gradients within the test chamber [6] and additional challenges for the application of low temperature combustion (LTC) are outlined in Agarwal et al. [11].

The work contained in this dissertation contributes to the experimental literature on low-to-intermediate temperature combustion kinetics for three C3 fuels at conditions relevant to pyrolysis, ignition, and detonation. The experimental work was conducted using three facilities: the University of Michigan rapid compression facility (UM-RCF), the Tsinghua University rapid compression machine (TU-RCM), and the Centre National de la Recherche Scientifique – Institut de Combustion, Aérothermique, Réactivité et Environnement (CNRS-ICARE) detonation tube. Each of these experimental setups allowed for detailed study of different aspects of combustion behavior and provided valuable insights into fuel behavior at LTC conditions. A brief description of each chapter and the experimental facilities used are provided here.

1.2 Low Temperature Combustion: From Pyrolysis to Detonation

1.2.1 iso-Propanol Pyrolysis Chemistry

There is significant interest in utilizing alcohols produced from biomass as alternative fuels that can offset carbon emissions from the transportation sector as neat fuels and in fuel blends [12]. The production of alternative liquid biofuels from lignocellulosic material (biomass not used for food production) has the potential to significantly reduce food feedstock competition and CO_2 emissions, issues faced by first generation biofuels [13]. Currently, ethanol is by far the most widely used biofuel [14], but larger alcohols have garnered interest recently as viable alternative biofuels, with the U.S. Department of Energy's Co-Optimization of Fuels and Engines initiative (Co-Optima) program identifying both *n*-propanol and *iso*-propanol as top 10 candidates for use in boosted SI engines and top six blendstocks with the fewest barriers to adoptions [15].

As mentioned in the previous section, understanding the combustion kinetics of alternative fuels is key to designing accurate mechanisms that can test their feasibility in applied energy generation concepts, with finite rate chemistry impacting heat release rates, combustion efficiencies, and pollutant emissions. For *iso*-propanol, while there have been several experimental studies on viability as a fuel additive in various engine configurations, there are limited experimental data on the underlying kinetics. The initial thermal decomposition of a fuel is an important step in the combustion process because pyrolysis reactions are one of the classes of initiation reactions that start the fuel consumption process and produce the free radicals that sustain combustion. Therefore, the objective of the research presented in **Chapter 2** was to quantify the reaction pathways of *iso*-propanol pyrolysis at a range of temperature and pressure conditions. The pyrolysis speciation data, in combination with ignition studies, are critical experimental measurements to define *iso*-propanol reaction rates. Beyond the feasibility of *iso*-propanol as an alternative fuel or fuel additive, the hierarchical nature of combustion modeling makes accurate descriptions of *iso*-propanol combustion chemistry key to producing accurate chemical kinetic mechanisms for larger alcohols as well.

The work presented in **Chapter 2** contributes to the understanding of thermal decomposition of *iso*-propanol by providing the first experimental data on *iso*-propanol pyrolysis at low-to-intermediate temperatures (965 – 1193 K) and moderate pressures (4.4 – 10.0 atm). The technical approach used the UM-RCF, a fast-gas sampling system, and gas chromatography to measure the production of seven stable intermediate species and the consumption of *iso*-propanol. The experimental results are compared with model predictions using a recently developed chemical kinetic mechanism for *iso*-propanol by Saggese et al. [16]. The comparisons demonstrate the importance of speciation data as tests of our predictive understanding of pyrolysis chemistry of this important reference fuel.

1.2.2 Ignition Characteristics of Propane

Experimental measurements of ignition delay time (IDT) are another method of characterizing fuel reactivity and reaction rates and validating chemical kinetic models across a range of temperature and pressure conditions important for design of energy generation systems that utilize combustion. IDT measurements are global descriptions of experiments that define the amount of time a mixture of fuel and oxidizer takes to ignite a specific temperature and pressure conditions. IDT studies are typically conducted using shock tubes, which can achieve high temperatures and pressures by rapidly heating a test gas using a shock wave, or rapid compression machines, which are better suited for low-to-intermediate temperature studies and typically use a piston to heat and pressurize the test gas. With increased interest in LTC strategies to increase efficiency and reduce emissions of the transportation and stationary power generation systems [17], accurate understanding of LTC chemistry is essential to advancing these applications [18], making IDT data at low temperature conditions especially valuable.

While LTC strategies show promise for next-generation combustion applications, there are challenges to experimental studies at lower temperatures (e.g., for T<1200 K, longer test times increase the impact of facility effects on IDT data) and LTC applications (increased propensity for misfire and reduced control of heat release rates) [17]. In addition to the low reaction rates, certain fuels exhibit NTC behavior adding a layer of complexity to interpreting experimental data at LTC conditions. The impact on experimental measurements is concerning, given the important role of IDT data on characterizing fuels and their reactivity.

Major drivers of facility effects on IDT data are temperature gradients within the reactor chamber including thermal boundary layers. Temperature gradients can lead to localized ignition and propagation of reaction fronts. In shock tubes, thermal gradients are introduced by non-idealized shock behavior and boundary layer effects, and in rapid compression machines, thermal gradients are created by fluid motion induced by the compression process and thermal boundary layers. At some experimental conditions, formation of reaction fronts can affect the autoignition process of the bulk gas region leading to ignition behavior known as "weak" or "mixed" ignition in contrast with "strong" ignition where the bulk gas autoignites homogeneously [19,20]. Moreover, thermal boundary layers created between the heated core of a test gas and the surrounding walls of the reaction chamber (typically at room temperature) can create conditions where an NTC fuel exhibits greater sensitivity to autoignition in the boundary layer.

The nuanced effects of thermal gradients are likely a significant source of the scatter observed in IDT data within the NTC region [21,22]. The objectives of the studies presented in **Chapters 3** and **4** were to characterize the effects of thermal gradients, quantitatively and qualitatively, on IDT data. The work in **Chapter 3** focuses on the impact of autoignition regimes on ignition data and **Chapter 4** focuses on the impact of thermal boundary layers on ignition of NTC fuels. Propane was chosen as the fuel of interest for both studies due to its prevalence in natural gas blends, its importance as a primary fuel and intermediate for the combustion chemistry of larger fuels, the robust literature available for propane combustion chemistry, and its role as the smallest alkane to exhibit NTC behavior at low temperatures [23]. In addition to the experimental results, **Chapter 3** validates an *a priori* method for predicting autoignition behavior known as the Sankaran Criterion [24] as a method for interpreting existing experimental data in the literature. **Chapter 4** presents computational results from a two-zone model used to identify conditions where boundary layer effects are expected to have the largest impact on ignition data of NTC fuels and associated experimental data from the UM-RCF and the TU-RCM.

1.2.3 iso-Propyl Nitrate as a Detonation Sensitizer

Detonation within a conventional IC engine is a highly undesirable event that can result in "super-knock" and cause severe engine damage due to high peak pressure and pressure oscillations within the engine [25]. However, controlled detonation as a propulsion method (in both pulse detonation engines (PDEs) and rotating detonation engines (RDEs)) has higher theoretical efficiency compared with conventional combustion engines due to the higher thermodynamic efficiency of energy released during the detonation process (termed pressure-rise or pressure-gain combustion) [26,27]. The emissions reductions potential from utilizing detonation within propulsion systems has led researchers to investigate the feasibility of these engines and address issues of consistency in the detonation initiation process and stability once a detonation wave has been formed. Beyond interest in controlled detonation for propulsion, detonation research is motivated by the importance of identifying critical conditions that can lead to detonation to ensure proper risk-mitigation strategies when using and storing combustible materials [28].

Initiation of detonation within PDEs and RDEs is accomplished through deflagration-to-detonation transition (DDT) processes, where the combustion wave begins as a deflagration wave (i.e., a flame) that transitions to detonation through induced turbulence leading to overpressure waves until critical conditions are reached for the formation of a detonation wave. The importance of size and weight considerations for engine designs mean that methods increasing the sensitivity of fuels to detonation are an important research topic to reduce the length needed for this transition to occur within the engine [26]. JP-10 and kerosene are fuels suitable for use in PDE and RDE applications but have large and complex kinetics making numerical studies on these fuels challenging. Propane has similar detonation properties to these fuels, making it a useful surrogate fuel for detonation studies [29] and for understanding how larger hydrocarbons are expected to react to the addition of detonation sensitizers. The fuel sensitizer and monopropellant hydrazine has been used for decades in propulsion applications but is expected to be heavily restricted in Europe in the next decade due to its high toxicity [30] leading to the search for "green" alternatives. Alkyl nitrates have emerged as possible alternative monopropellants and sensitizers, and *iso*-propyl nitrate (IPN) specifically is of interest due to its low cost and low toxicity [31,32].

The objective of the study presented in **Chapter 5** is to quantify the impact of the addition of 10% IPN on stoichiometric propane mixtures with and without additional nitrogen dilution on the critical conditions required to initiate detonation. The experiments were conducted using a detonation tube at the Centre National de la Recherche Scientifique – Institut de Combustion, Aérothermique, Réactivité et Environnement (CNRS-ICARE) in Orléans, France with a goal of identifying whether IPN is an effective detonation sensitizer for propane mixtures. The results report detonation wave speed and cell sizes measured in shock-to-detonation transition (SDT) experiments used to determine critical conditions for post-shock pressure and temperature required to initiate a detonation and how these critical conditions are impacted by the addition of IPN.

The final chapter of the thesis summarizes the conclusions of the C3 studies and provides recommendations for future work. In particular, areas where combustion and pyrolysis chemistry could benefit from additional studies are identified. Overall, the thesis contributes significantly to fundamental reaction chemistry and novel experimental methods to improve core knowledge of important reference fuels.

1.3 References

[1] Intergovernmental Panel on Climate Change. (2015). Climate Change 2014: Mitigation of Climate Change: Working Group III Contribution to the IPCC Fifth Assessment Report. Cambridge: Cambridge University Press.

[2] U.S. Energy Information Administration, Annual Energy Outlook 2021 (AEO2021), 2021.

[3] U.S. Energy Information Administration, International Energy Outlook 2021 (IEO2021), 2021.

[4] W. Leitner, J. Klankermayer, S. Pischinger, H. Pitsch, K. Kohse-Höinghaus, Advanced Biofuels and Beyond: Chemistry Solutions for Propulsion and Production, Angew. Chem. Int. Ed. 2017, 56, 5412.

[5] Vineet Singh Sikarwar, Ming Zhao, Paul S. Fennell, Nilay Shah, Edward J. Anthony, Progress in biofuel production from gasification, Progress in Energy and Combustion Science, Volume 61, 2017, Pages 189-248.

[6] Kevin P. Grogan, S. Scott Goldsborough, Matthias Ihme, Ignition regimes in rapid compression machines, Combustion and Flame, Volume 162, Issue 8, 2015, Pages 3071-3080.

[7] Singh R, Han T, Fatouraie M, Mansfield A, Wooldridge M, Boehman A. Influence of fuel injection strategies on efficiency and particulate emissions of gasoline and ethanol blends in a turbocharged multi-cylinder direct injection engine. International Journal of Engine Research. 2021;22(1):152-164.

[8] Cesar L. Barraza-Botet, Margaret S. Wooldridge, Combustion chemistry of *iso*-octane/ethanol blends: Effects on ignition and reaction pathways, Combustion and Flame, Volume 188, 2018, Pages 324-336.

[9] Modeling and Simulation of Turbulent Combustion. Singapore: Springer Singapore, doi:10.1007/978-981-10-7410-3.

[10] Yuan, Wenhao, Li, Yuyang, Qi, Fei, Challenges and perspectives of combustion chemistry research, Science China Chemistry, Volume 60 (11), Beijing: Science China Press, p. 1391–1401.

[11] Avinash Kumar Agarwal, Akhilendra Pratap Singh, Rakesh Kumar Maurya, Evolution, challenges, and path forward for low temperature combustion engines, Progress in Energy and Combustion Science, Volume 61, 2017, Pages 1-56.

[12] International Energy Agency, World Energy Outlook 2020 (WEO2020), 2020.

[13] T. Damartzis, A. Zabaniotou, Thermochemical conversion of biomass to second generation biofuels through integrated process design—A review, Renewable and Sustainable Energy Reviews, Volume 15, Issue 1, 2011, Pages 366-378.

[14] J.M. Bergthorson, M.J. Thomson, A review of the combustion and emissions properties of advanced transportation biofuels and their impact on existing and future engines, Renew. Sustain. Energy Rev., 42 (2015), pp. 1393-1417.

[15] D.J. Gaspar, B.H. West, D. Ruddy, T.J. Wilke, E. Polikarpov, T.L. Alleman, et al., Top ten blendstocks derived from biomass for turbocharged spark ignition engines: bio-blendstocks with potential for highest engine efficiency, Pacific Northwest National Lab (PNNL); 2019. PNNL-28713.

[16] Chiara Saggese, Charlotte M. Thomas, Scott W. Wagnon, Goutham Kukkadapu, Song Cheng, Dongil Kang, S. Scott Goldsborough, William J. Pitz, An improved detailed chemical kinetic model for C3-C4 linear and *iso*-alcohols and their blends with gasoline at engine-relevant conditions, Proceedings of the Combustion Institute, Volume 38, Issue 1, 2021, Pages 415-423.

[17] G.A. Richards, M.M. McMillian, R.S. Gemmen, W.A. Rogers, S.R. Cully, Issues for low-emission, fuel-flexible power systems, Prog. Energy Combust. Sci. 27 (2) (2001) 141-169.

[18] S. Saxena, I.D. Bedoya, Fundamental phenomena affecting low temperature combustion and HCCI engines, high load limits and strategies for extending these limits, Prog. Energy Combust. Sci. 39 (2013) 457-488.

[19] S.M. Walton, X. He, B.T. Zigler, M.S. Wooldridge, A. Atreya, An experimental investigation of *iso*-octane ignition phenomena, Combust. Flame 150 (3) (2007) 246-262.

[20] A.B. Mansfield, M.S. Wooldridge, High-pressure low-temperature ignition behavior of syngas mixtures, Combust. Flame 161 (9) (2014) 2242-2251.

[21] J.F. Griffiths, D.J. Rose, M. Schreiber, J. Meyer, K.F. Knoche, Novel features of end-gas autoignition revealed by computational fluid dynamics, Combustion and Flame, Volume 91, Issue 2, 1992, Pages 209-212.

[22] Gaurav Mittal, Mandhapati P. Raju, Chih-Jen Sung, CFD modeling of two-stage ignition in a rapid compression machine: Assessment of zero-dimensional approach, Combustion and Flame, Volume 157, Issue 7, 2010, Pages 1316-1324.

[23] T. Goyal, D. Trivedi, O. Samimi Abianeh, Autoignition and flame spectroscopy of propane mixture in a rapid compression machine, Fuel 233 (2018) 56-67.

[24] R. Sankaran, H.G. Im, E.R. Hawkes, J.H. Chen, The effects of non-uniform temperature distribution on the ignition of a lean homogeneous hydrogen–air mixture, Proc. Combust. Inst. 30 (1) (2005) 875-882.

[25] Kalghatgi GT, Bradley D. Pre-ignition and ‘super-knock’ in turbo-charged spark-ignition engines. International Journal of Engine Research. 2012;13(4):399-414.

[26] G.D. Roy, S.M. Frolov, A.A. Borisov, D.W. Netzer, Pulse detonation propulsion: challenges, current status, and future perspective, Progress in Energy and Combustion Science, Volume 30, Issue 6, 2004, Pages 545-672.

[27] Frank K. Lu and Eric M. Braun, Rotating Detonation Wave Propulsion: Experimental Challenges, Modeling, and Engine Concepts, Journal of Propulsion and Power 2014 30:5, 1125-1142.

[28] J.E. Shepherd, Detonation in gases, Proceedings of the Combustion Institute, Volume 32, Issue 1, 2009, Pages 83-98.

[29] O.G. Penyazkov, K.A. Ragotner, A.J. Dean, B. Varatharajan, Autoignition of propane–air mixtures behind reflected shock waves, Proceedings of the Combustion Institute, Volume 30, Issue 2, 2005, Pages 1941-1947.

[30] Naumann, Clemens, Kick, Thomas, Methling, Torsten, Braun-Unkhoff, Marina, Riedel, Uwe, Ethene/nitrous oxide mixtures as green propellant to substitute hydrazine: reaction mechanism validation, International journal of energetic materials and chemical propulsion, vol. 19, no. 1. pp. 65–71.

[31] Mark E. Fuller and C. Franklin Goldsmith, Shock Tube Laser Schlieren Study of the Pyrolysis of Isopropyl Nitrate, The Journal of Physical Chemistry A 2019 123 (28), 5866-5876.

[32] Anirudha Ambekar, Sheshadri Sreedhara, Arindrajit Chowdhury, Burn rate characterization of *iso*-propyl nitrate – A neglected monopropellant, Combustion and Flame, Volume 162, Issue 3, 2015, Pages 836-845.

Chapter 2: An Experimental Study of *iso*-Propanol Pyrolysis Chemistry

2.1 Introduction

There is an urgent need to reduce harmful pollutant and greenhouse gas emissions produced by the combustion of fossil fuel sources, which currently accounts for more than two-thirds of global energy production [1]. Alcohols produced from biomass are of significant interest as an alternative fuel to offset emissions and improve the sustainability of liquid fuel utilization in the transportation sector [2,3,4]. There have been extensive studies on short-chain alcohols, in particular because ethanol is currently the most widely used biofuel in the world [5]. There is also considerable interest in the viability of larger alcohols, including the propanol isomers, and the U.S. Department of Energy's Co-Optimization of Fuels and Engines initiative (Co-Optima) identified *n*- and *iso*-propanol as top 10 candidates for biofuels for use in boosted spark ignition (SI) engines and one of the top six blendstocks with the fewest barriers to adoption, specifically due to the high research octane number (RON) and octane sensitivity of propanol [6]. Due to these characteristics, several experimental studies on *iso*-propanol have been conducted using SI and homogenous charge compression ignition (HCCI) engines to investigate the viability of *iso*-propanol as a fuel additive [7,8,9,10,11,12]; however, experimental data specifically on the chemical kinetics of *iso*-propanol decomposition are currently limited [13,14,15].

Physical measurements of elementary rate coefficients and branching fractions are critical to accurate predictive understanding of combustion systems, particularly combustion applications operating at low-to-intermediate temperatures (e.g., 600 to 1200 K) where finite rate chemistry can play a large role on heat release rates, combustion efficiencies, and pollutant emissions. Direct measurements of rate coefficients at moderate temperatures are particularly challenging due to the relatively slow characteristic test times of the reactions in comparison with high temperature conditions (e.g., T> 1500 K). Moreover, reactions with multiple active product channels add complexity and the need to determine branching fractions, which are typically more difficult to determine using theory, modeling, or physical measurements. Experimental data that provide direct insight into the dominant reaction pathways at intermediate temperatures are vital for developing combustion chemistry theory and validating elementary rate coefficients and reaction mechanisms. As noted by Sarathy et al. [15] "Quantitative species profiles are the most challenging test case for kinetic models."

The objective of this study was to demonstrate a novel application of rapid compression experiments to identify and quantify the major intermediate species produced during *iso*-propanol ($2\text{-}C_3H_7OH$) pyrolysis (i.e., thermal decomposition) studies to inform and direct fundamental understanding of *iso*-propanol combustion chemistry at intermediate temperatures. While rapid compression experiments have been widely applied to ignition studies at temperatures ranging from 600 K – 1800 K, pyrolysis studies at these conditions using rapid compression remain relatively under-developed. The only previous work in the area is by Zhang et al. [16], who demonstrated a process for assigning rate coefficients using speciation data from rapid compression pyrolysis experiments for dimethyl carbonate decomposition. Thus, a key goal of this study is to demonstrate the protocol for effectively using the University of Michigan rapid compression facility (RCF) for pyrolysis studies that can inform theory and improve understanding with high-quality physical measurements. Ignition delay time (IDT) studies of *iso*-propanol, as both a neat fuel and in fuel blends, have predominantly been conducted in shock tubes (ST) at high temperatures (typically > 1300 K) and pressures of 1 to 14 atm [17,18,19,20] with the first rapid compression machine (RCM) data at temperatures of 700 to 1000 K and pressure of 20 to 40 atm being reported recently [21,22]. Laminar flame speed measurements of *iso*-propanol/air mixtures at a range of equivalence ratios and pressures of 1 atm have also been reported [23]. Speciation studies of *iso*-propanol oxidation (typically at atmospheric pressure) have also been conducted using diffusion flames [24,25], premixed flames [23,26,27], non-premixed flames [23,28], and a jet-stirred reactor [29]. The most directly relevant studies to this work are the speciation studies that focused on *iso*-propanol pyrolysis and were conducted in shock tubes and flow reactors. Jouzdani et al. [19] used laser diagnostics to measure CO production during *iso*-propanol combustion and pyrolysis in a shock tube at pressure conditions of 3.5, 5.0, and 11 atm over a temperature range of 1150 – 1550 K. Similarly, Cooper et al. [14] used laser diagnostics and a shock tube to measure H_2O production during *iso*-propanol pyrolysis at a pressure of 1.42 atm over a temperature range of 1127 – 1621 K. The only other speciation studies focusing on *iso*-propanol pyrolysis have been conducted using flow reactors. Li et al. [13] measured the concentration of sixteen profiles of *iso*-propanol and stable products of pyrolysis over temperatures ranging from 904 – 1333 K at pressures of 0.04, 0.2, and 1 atm. Heyne et al. [30] reported concentrations of nine intermediate species and *iso*-propanol at four temperature conditions (800, 978, 981, 999 K) with all experiments conducted between 12.5 – 12.6 atm. The results showed water, propene, acetaldehyde, ethene, methane, and acetone were key products formed during *iso*-propanol pyrolysis.

Multiple efforts have been made to determine rate coefficients for the key *iso*-propanol pyrolysis reactions. In 2002, Bui et al. [31] used first principles to calculate the potential energy surface of the *iso*-propanol system and, while there are many potential product channels (nine channels were considered in the study), Bui et al. [31] found the dominant channel for pyrolysis at temperatures in the range of 500 to 2500 K and for $P < 1$ atm was the dehydration reaction:

$$\text{2-}C_3H_7OH\ (+M) = CH_3C(H)CH_2 + H_2O\ (+M) \tag{1a}$$

For higher pressures and temperatures above 1200 K, the scission channel breaking the C-C bond was dominant:

$$\text{2-}C_3H_7OH\ (+M) = CH_3C(H)OH + CH_3\ (+M) \tag{1b}$$

Experimental data from Tsang [32] at 1080-1160 K and 0.52 – 0.66 atm agreed well with the recommended rate coefficient by Bui et al. [31] for the CH_3-producing channel (Reaction 1b). Trenwith [33] conducted a pyrolysis study of 2-C_3H_7OH at 720-801 K and 0.01-0.13 atm and derived rate coefficients for 2-C_3H_7OH thermal decomposition from measurements of stable intermediate species including acetone and propene. Trenwith [33] attributed the propene formation to direct production by Reaction (1a) and attributed the acetone to direct production by:

$$\text{2-}C_3H_7OH\ (+M) = CH_3COCH_3 + H_2\ (+M) \tag{1c}$$

Bui et al. [31] compared their recommendation for the rate coefficient for the H_2O channel (Reaction 1a) with the experimental data from Trenwith [33] for H_2O and found the predicted values were one to two orders of magnitude lower than the experimental data, which they attributed to interfering reactions in the experiments. Trenwith did not recommend rate coefficients for Reaction 1a, but updates for the rate coefficients of the dehydration reaction were made by Heyne et al. [30] with further revisions made by Cooper et al. [14].

Both Kasper et al. [27] and Li et al. [26] conducted extensive investigations of the combustion chemistry of the propanol isomers including high-fidelity species measurements in low-pressure flames. Kasper et al. [27] noted at the time of their publication (2009) no detailed chemical kinetic model for the combustion of either isomer had been published. Subsequently, several groups including Johnson et al. [17], Frassoldati et al. [28], and Veloo and Egolfopoulos [23] added experimental data on propanol combustion and proposed detailed chemical kinetic mechanisms for the propanol isomers, including estimates for the critical H-abstraction reactions from 2-C_3H_7OH by OH, H, and CH_3. These mechanisms and others are discussed in the comprehensive review of alcohol combustion chemistry by Sarathy et al. [15]. In Sarathy et al. [15], the authors note the only studies of the elementary rate coefficients of the H-atom abstraction reactions are of 2-C_3H_7OH+OH, and the studies were all conducted at temperatures below 745 K and pressures below 1 bar. There are no previous experimental measurements of the 2-C_3H_7OH+CH_3 and the 2-C_3H_7OH+H elementary reactions. Thus, this study was motivated to provide the first experimental data on 2-C_3H_7OH pyrolysis at intermediate temperature and moderate pressure conditions for the purpose of advancing the understanding of elementary combustion chemistry of *iso*-propanol.

2.2 Methods

2.2.1 Experimental

The University of Michigan rapid compression facility (UM-RCF) is a unique experimental apparatus used to create uniform state conditions at intermediate-to-high temperatures (600-2000 K) and high-pressures (1-40 atm) using an isentropic compression process [34]. The UM-RCF has previously been used for ignition studies of reference hydrocarbons [35,36,37,38,39,40,41,42], syngas mixtures [43,44,45,46], and oxygenated hydrocarbons [40,47,48,49,50]. Beyond ignition delay time (IDT) measurements, the UM-RCF has been used to measure intermediate species production during combustion using similar fast gas sampling and gas chromatography techniques described in the present work [40,47,51,52] and OH concentrations during ignition using laser absorption of a ring-dye OH laser [37]. The current work is the first attempt to conduct speciation studies of fuel pyrolysis using the UM-RCF.

As described in Donovan et al. [34], the UM-RCF consists of a driver and driven section separated by a fast-acting hydraulic globe valve. A free piston is used to rapidly compress the test gas mixture into a small volume at the end of the driven section, referred to in this work as the test section, to the desired thermodynamic conditions required for the chemistry studies of interest. Prior to each experiment, test gas mixtures are prepared in a stainless-steel mixing tank equipped with an automatic stirring mechanism. Mixture composition is determined by measuring relative partial pressures of each component gas while filling the mixing tank. Following mixture preparation, the tank is isolated and left to mix for a minimum of 10 hours.

For each experiment, two vacuum pumps (Varian DS 102) are used to evacuate the driven section. After evacuating to ~0.3 torr, the driven section is filled with the test gas mixture of interest, while the driver section is filled to high pressure with compressed air. The compression process occurs by opening the globe valve once both the driver and driven sections have been appropriately filled, causing the free piston to travel the length of the driven section and rapidly compress the test gas mixture into the small test section volume. At end-of-compression (EOC) the piston nosecone seats into an interface fit, trapping the test gas mixture in the test section at the desired temperature and pressure conditions. The compression process takes roughly 100 ms, with most of the pressure and temperature increases occurring within the last 10-20 ms. A pressure transducer (Kistler 4045A2) and charge amplifier (Kistler 5010) located in the test section are used to measure the pressure time history of each experiment with a 100 kHz sampling frequency, which is used to calculate temperature within the test section up-to and after EOC. A detailed study of the temperature uniformity within the UM-RCF at EOC conditions and validation of the isentropic calculations used to determine temperature within the test section can be found in Donovan et al. [34].

While the UM-RCF can be configured for optical diagnostics of ignition events, the focus of the present work is of fuel pyrolysis meaning optical diagnostics like high-speed imaging would be of no utility. As such, the end-wall of the test section was configured for fast gas sampling of the test gas mixture to be studied with gas chromatography. The sampling system consists of two sampling volumes connected to the chamber by a sampling probe and solenoid valve. Prior to the experiments, the sampling volumes are evacuated using a vacuum pump then isolated from the pump by a valve. The sampling chambers are monitored with pressure transducers (Kistler 4045A5) and charge amplifiers (Kistler 4618A0) to determine sampling time relative to EOC and in-chamber sampling pressure. Sample timing is controlled by a digital pulse generator (Stanford Research Systems, DG535) used to trigger each of the solenoid valves independently. A schematic of the UM-RCF test section configured for fast gas sampling is provided in **Figure 2.1**. In the present study, gas samples were taken at times ranging from 2 – 47 ms relative to EOC with a maximum sampling time uncertainty of ± 1.8 ms. This uncertainty is determined based on the pressure time histories of the sample volumes, with the assigned sampling time based on the maximum dP/dt of the sampling pressure signal. Additional uncertainty is considered based on the post-processing smoothing algorithm used to reduce noise in the sample pressure signal. Noise in the raw pressure trace is a result of mechanical vibrations caused by the compression stroke of the free piston and seating of the piston within the test section. The point number considered for the smoothing algorithm is varied by a factor of ± 2 to assign uncertainty in the pressure trace and associated temperature trace within the test section.

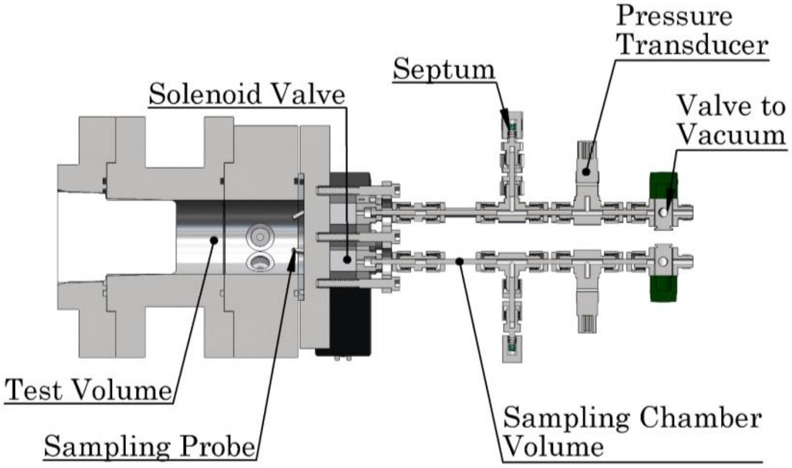

Figure 2.1: Schematic for the UM-RCF test section configured for fast-gas sampling and speciation analysis adapted from Karwat et al. [40]

Post-experiment, the samples were extracted using two syringes (Hamilton Gastight #1010) and were injected into a PerkinElmer gas chromatograph (GC) equipped with a CP-Porabond Q column and FID detector using ultra-high purity helium as the carrier gas. Specifics on the temperature program used in the GC are included in **Appendix A**. The GC was calibrated for methane (CH_4), acetylene (C_2H_2), ethene (C_2H_4), ethane (C_2H_6), acetaldehyde (CH_3CHO), acetone (CH_3COCH_3), propene (C_3H_6), and *iso*-propanol (2-C_3H_7OH) using high purity reference chemicals, which are listed in **Appendix A**. Dilution effects within the sampling system were accounted for based on pre-sample pressure transducer data. The two main sources of uncertainty for the species concentrations were the dead volume in the sampling system (~8%) and the calibration uncertainties for each species. These uncertainties were < 15% for the smaller hydrocarbons (CH_4, C_2H_2, C_2H_4, C_2H_6), < 25% for propene, acetaldehyde, and acetone, and < 40% for *iso*-propanol. The sampling and GC technique used in the present work has also been utilized in previous studies by Karwat et al. [40] and Barraza-Botet et al. [49].

2.2.2 Computational

Chemical kinetic modeling studies were conducted using the recently published mechanism for C3-C4 linear and *iso*-alcohols by Saggese et al. [53]. The mechanism was selected based on its validation against RCM and ST data at low-to-intermediate temperatures relevant to the present work. The mechanism is comprised of C0-C4 chemistry from the AramcoMech 2.0 mechanism published by Li et al. [54] with a revised version of alcohol chemistry from Sarathy et al. [15]. A detailed description of the mechanism and major revisions to alcohol chemistry are provided in Saggese et al. [53]. Briefly, revisions to the Sarathy et al. [15] mechanism focused on the H-atom abstraction reaction by both OH and HO_2. Rate coefficients for the *iso*-propanol + OH H-atom abstraction reactions were calculated by analogy based on rate coefficients for butanol isomers in McGillen et al. [55]. Similarly, rate coefficients for the *iso*-propanol + HO_2 H-atom abstraction reactions were calculated by analogy at the β- and γ-sites based on work by Mittal et al. [56] and Zhao et al. [57], with the remaining H-atom abstraction reaction taken from Johnson et al. [17]. Recent theoretical work on the initial kinetics of the pyrolysis process for H-atom abstraction reactions for a series of alkanes, alcohols, and aldehydes have been published by Elliot et al. [58] with ongoing work being conducted to integrate these reaction rates into existing mechanisms.

The modeling calculations were implemented in a zero-dimensional closed homogeneous reactor model in the CHEMKIN suite of programs (version 10131, x64) [59] to predict concentrations of the stable intermediate species measured during the UM-RCF experiments. The 0D reactor model used a volume-time history based on the pressure-time history measurements during a typical RCF pyrolysis experiment at each of the four experimental conditions studied. The use of a volume-time history allows for the calculations to account for both reactions occurring during the compression stroke prior to EOC and the effects of heat transfer between the UM-RCF test section and the surrounding area after EOC.

2.3 Results and discussion

2.3.1 Experimental Results

Average compositions of the three test gas mixtures of interest for this work are provided in **Table 2.1**, with the composition of each individual experiment provided in **Appendix A**. Typical pressure data from a pyrolysis sampling experiment in the UM-RCF are presented in **Figure 2.2**, which illustrates the compression stroke up to end-of-compression (EOC) defined as the point of maximum pressure. Post-EOC, there is an observed pressure decrease due to heat transfer from the heated gas within the test section to the test section wall. Additionally, the pressure within each of the two sampling valves are presented with their associated sampling uncertainties. Sampling times are defined as the amount of time from EOC to the midpoint of the sample acquisition time, defined at maximum rate of pressure change, dP/dt, within the sample chamber. The uncertainty associated with each sample time represents the duration of the gas sampling event and additional uncertainty from the smoothing algorithm used to reduce noise in the pressure signal. Average uncertainty in the assigned sampling times is ±1.6 ms with a maximum observed uncertainty of ±1.8 ms. While the sampling valves do remove a small amount of test gas from the test section, the volume is small enough to not have a significant impact on the pressure within the test section. Pressure and temperature states were assigned individually for each sample to account for the associated heat loss between EOC and the sampling event. As shown in **Figure 2.2**, the assigned pressure for sample 2 is slightly lower than that of the assigned pressure for sample 1 due to this heat loss over time. The experiments are expected to be endothermic, which would lead to an additional decrease of pressure in the test section; however, the mixtures are sufficiently dilute that endothermic reactions do not affect the overall pressure-time profiles, as shown in the comparison between the pressure traces from an inert mixture and the experimental results provided in **Appendix A**.

Table 2.1: Average temperature, pressure, and mixture composition for the test gas mixtures (mole basis) at each experimental condition studies. Standard deviations are listed for temperature and pressure conditions based on experimental data and assigned uncertainties for mixture composition are a result of uncertainty in the pressure transducers.

Temperature (K) ±σ	**Pressure (atm) ±σ**	**2-C_3H_7OH (%)**	**Ar (%)**	**N_2 (%)**
965 ± 12	5.2 ± 0.3	1.5 ± 0.01	9.6 ± 0.1	88.9 ± 0.1
1067 ± 15	4.4 ± 0.2	1.5 ± 0.01	29.1 ± 0.1	69.4 ± 0.1
1074 ± 13	10.0 ± 0.5	1.5 ± 0.01	29.2 ± 0.1	69.3 ± 0.1
1193 ± 20	5.1 ± 0.3	1.5 ± 0.01	50.7 ± 0.1	47.8 ± 0.1

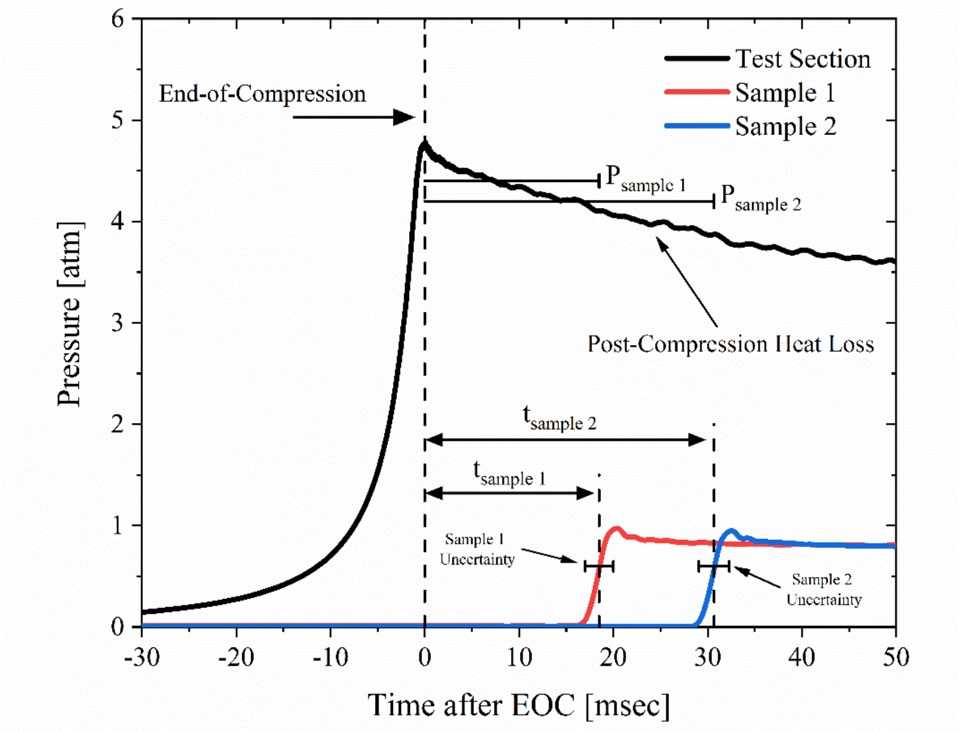

Figure 2.2: Typical experimental pressure-time history from a UM-RCF pyrolysis experiment for a mixture of 1.5% *iso*-propanol at EOC conditions of P = 4.8 atm and T = 1091 K, including assigned pressures for each sample to account for heat loss and sampling times with their associated uncertainties.

Test-section pressure measurements for all experiments conducted at the four conditions of interest are shown in **Figure 2.3**. The experiments overall show good repeatability with respect to state conditions and species measurements. The differences between the pressure time-histories are predominantly due to the slight variation of test gas compression that can occur during the seating of the nosecone in the UM-RCF at the EOC, as the polyethylene nosecone can deform slightly differently from experiment-to-experiment as it seals the test-gas. Standard deviations are provided for each of the four temperature and pressure conditions of interest based on variation in EOC conditions and heat loss between the individual experiments and are reported in **Table 2.1**. The largest standard deviation observed in the pressure was 0.5 atm, associated with the T = 1074 K, P = 10.0 atm condition, and the remaining conditions yielded standard deviations of 0.3 atm or less for pressure. Uncertainties in the individual experimental pressure and temperature measurements is a result of the pressure transducer resolution and smoothing algorithm used to process the pressure data. These uncertainties are reported for each run in **Appendix A**.

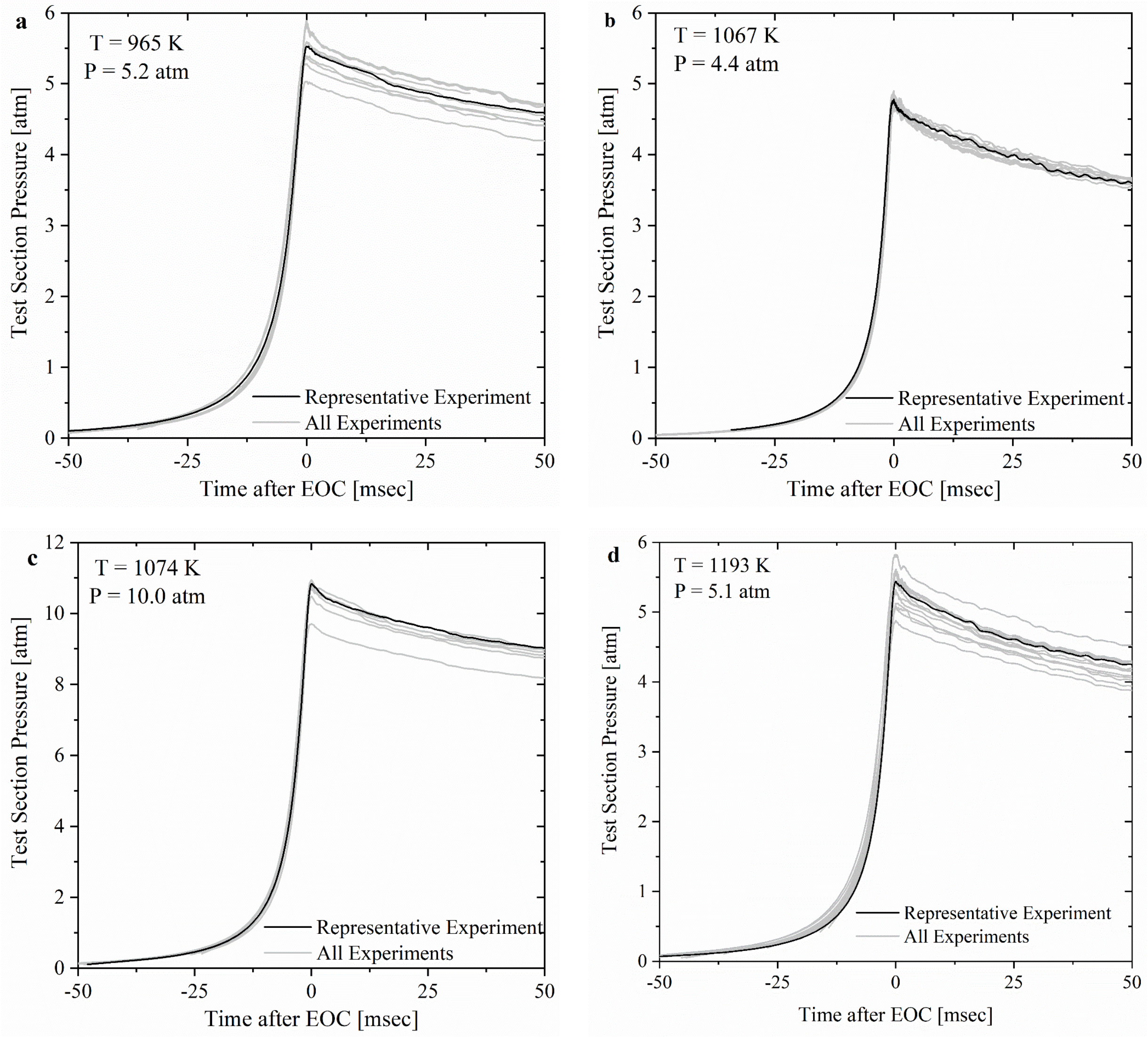

Figure 2.3: Pressure measurements for all experiments at the four conditions of interest. The highlighted pressure data were considered representative and were used in the model simulations. The average temperature and pressure conditions for each group of experiments are provided in the panels.

Figure 2.4 shows a typical gas chromatogram readout obtained from an *iso*-propanol pyrolysis sampling experiment and highlights which peaks correspond to each stable intermediate species and *iso*-propanol, with a single unidentified peak in between acetaldehyde and acetone. At the highest temperature data (T = 1193 K, P = 5.1 atm), an acetylene peak is also identified. The carbon balance for the measured species at the lowest temperature condition of T = 965 K, P = 5.2 atm is 82 ± 20% at early sampling times, less than 10 ms and 73 ± 15% at later sampling times after 30 ms. At the intermediate temperature condition of T = 1067 K, P = 4.4 atm, the carbon balance is 86 ± 7% at sampling times less than 10 ms, and 74 ± 5% at sampling times after 30 ms.

When the pressure is varied at the intermediate temperature condition of T = 1074 K, P = 10.0 atm, the carbon balance is 74 ± 17% at sampling times less than 10 ms, and 60 ± 12% at sampling times after 30 ms. Finally, at the highest temperature condition of T = 1193 K, P = 5.1 atm, the carbon balance is 81 ± 14% at sampling times less than 10 ms, and 73 ± 9% at sampling times after 30 ms. The plots of the carbon balance and associated uncertainties for each individual experiment compared with the model prediction of carbon captured by the measured species are presented in **Appendix A**. Since the mole fraction of *iso*-propanol in the system prior to each experiment is held constant across all four conditions, the carbon content prior to each experiment is also held constant. The carbon balance indicates that, while most of the carbon is contained in the measured species, there are still additional species produced that are not measured, with modeling predictions suggesting that some of these additional species may be CO or C1-C2 oxygenated hydrocarbons.

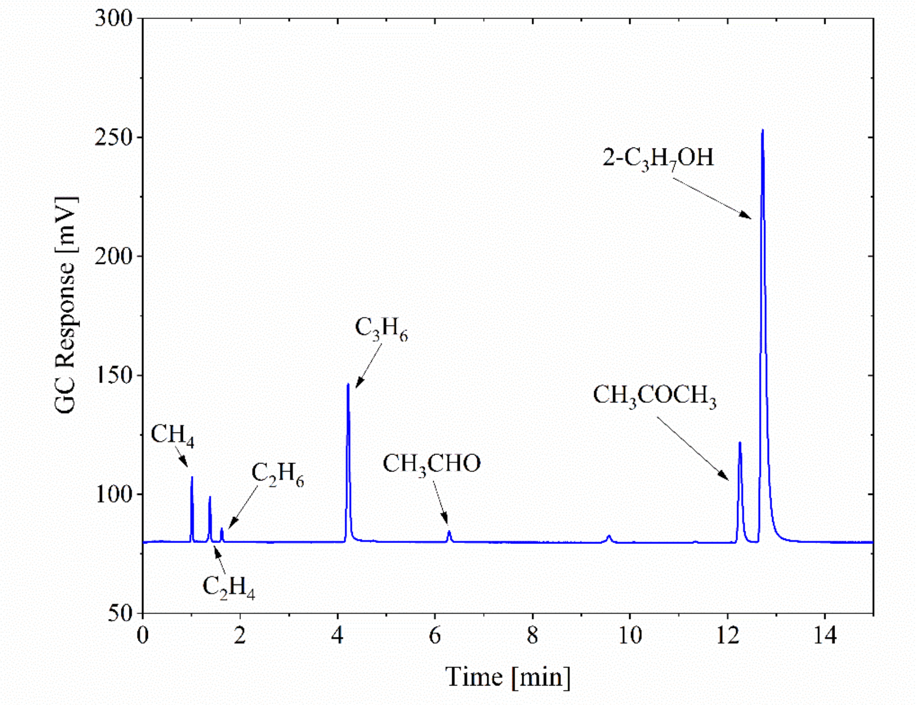

Figure 2.4: Typical gas chromatogram for a *iso*-propanol pyrolysis gas sampling experiment at T = 1053 K, P = 4.2 atm, and a sampling time t = 31.3 ms.

Overall percent differences between the model predictions and experimental observations at three different sampling time ranges are summarized in **Figure 2.5**. Results comparing species measurements across different temperature conditions are shown in **Figure 2.6** and **Figure 2.7**, with the plot for Acetylene in **Figure 2.6(g)** only providing results at the T = 1193 K, P = 5.1 atm condition, since Acetylene was not present in observable concentrations at the lower temperature conditions. **Figure 2.6** shows the impact that changing temperature has on species concentration when pressure is held roughly constant, with intermediate species concentration for all species besides acetone and *iso*-propanol showing an increase in production in response to increases of roughly 100 – 120 K in the temperature conditions. **Figure 2.7** shows the impact that changing pressure by more than a factor of 2 has on species concentration when temperature is held roughly constant, with intermediate species concentration remaining roughly constant for all species at the P = 4.4 atm and P = 10.0 atm conditions. Detailed discussion of the differences for each measured species provided below.

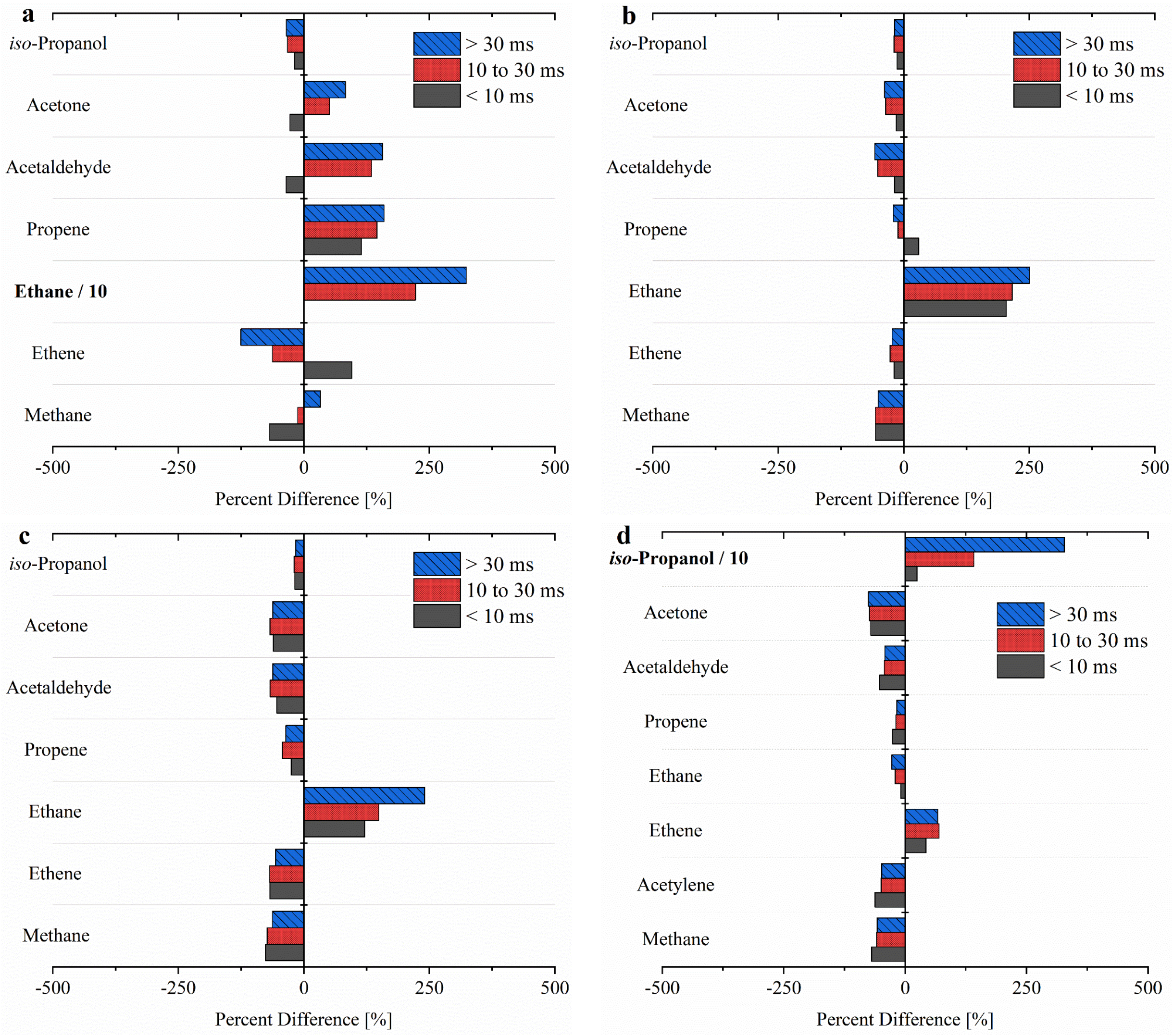

Figure 2.5: Percent difference between experimental results and model simulations at three ranges of time representing early times (< 10 ms), intermediate sampling times (10 to 30 ms), and late times (> 30 ms) for intermediate species and *iso*-propanol at the four conditions of interest: (a) T = 965 K, P = 5.2 atm, (b) T = 1067 K, P = 4.4 atm, (c) T = 1074 K, P = 10.0 atm,

and (d) T = 1193 K, P = 5.1 atm. Note that the percent difference results for ethane in panel (a) and *iso*-propanol in panel (d) have been divided by 10.

2.3.1.1 iso-Propanol

iso-Propanol consumption showed an increase in response to increases in both temperature and pressure. At T = 965 K, P = 5.2 atm, ~20% of the *iso*-propanol has been consumed within the first 10 ms, which increases to ~40% after 30 ms. These values increase to ~30% within the first 10 ms and ~50% after 30 ms at T = 1067 K, P = 4.4 atm. When the pressure is increased at the intermediate temperature condition of T = 1074 K, P = 10.0 atm, ~30% of *iso*-propanol is consumed within the first 10 ms similar to the P = 4.4 atm condition; however, at later times after 30 ms the consumption rate increases to ~60% in response to the increase in pressure. As expected, the highest rate of *iso*-propanol consumption is observed at the T = 1193 K, P = 5.1 atm condition, with ~50% consumed within the first 10 ms that increases to ~70% after 30 ms. The kinetic model utilizing the mechanism by Saggesse et al. [53] performs well at predicting *iso*-propanol consumption outside of the highest temperature condition. Experimental observations of *iso*-propanol at the T = 965 K are all within 50% of the model predictions, while model performs even better at the T = 1067 K and the higher-pressure T = 1074 K conditions with experimental observations all within 30% of the model predictions. The largest discrepancy between predicted and observed consumption of *iso*-propanol occurs at the T = 1193 K, P = 5.1 atm conditions, where the model increasingly diverges from observed *iso*-propanol concentrations over time, leading to differences greater than an order of magnitude by the latest sampling times.

2.3.1.2 Acetone

Acetone is the lone species that did not show a consistent increase in concentration in response to an increase in temperature. Within the first 5 ms, the T = 1193 K, P = 5.1 atm condition showed the highest concentration of acetone relative to the two lower temperature conditions. The concentration of acetone then shows a decrease that is comparable to the concentrations observed at the T = 1067 K, P = 4.4 atm and T = 965 K, P = 5.2 atm conditions. The early spike in production followed by an associated decrease in concentration at the highest temperature condition is predicted by the model, showing a behavior that is distinct from the two lower temperature conditions, but with experimental observations of acetone concentration being ~75% lower than that predicted by the model. The concentrations of acetone among all three temperature conditions after 30 ms are within 50% of each other, with the intermediate temperature condition showing the highest concentration at later times.

2.3.1.3 Propene

Production of propene is well predicted by the model at all conditions. The largest difference occurs during later sampling times at the lowest temperature T = 965 K, P = 5.2 atm conditions, where propene production is underpredicted by over a factor of 2. At the T = 1074 K, P = 10.0 atm condition, propene production falls within 50% of the model predictions. The model predictions perform even better at T = 1067 K, P = 4.4 atm and T = 1193 K, P = 5.1 atm with both sets of observations falling within 30% of the model predictions.

2.3.1.4 Acetaldehyde

Like propene, production of acetaldehyde is well predicted by the model, and shows the largest difference at the lowest temperature condition. At the T = 965 K, P = 5.2 atm, the experimental data shows good agreement with the model at early sampling times that then begins to diverge as time increases. Experimental observations of acetaldehyde at later times are over a factor of two higher than those predicted by the model. Across the other conditions, the model shows good agreement with experimental observations. The higher-pressure T = 1074 K, P = 10.0 atm experimental results are within 70% of the model predictions, while both the T = 1067 K, P = 4.4 atm and T = 1193 K, P = 5.1 atm results are within 60% of the model predictions. The highest temperature condition shows a slight rate of consumption after an initial sharp increase in production of acetaldehyde in both the experimental observation and the model predictions, in contrast to the initial sharp increase followed by continued slower rates of consumption seen in the T = 1067 K and T = 965 K conditions.

2.3.1.5 Ethane

Ethane production shows the largest difference in observed concentrations relative to model predictions of the species measured at the lower temperature conditions. At the T = 965 K, P = 5.2 atm condition, ethane is produced at over an order of magnitude greater rate than that predicted by the model after 10 ms. Prior to the 10 ms time, the ethane concentration is below the detectable limit in the GC. As the temperature is increased to the T = 1067 K, P = 4.4 atm and T = 1074 K, P = 10.0 atm conditions, the difference between observed concentrations and model predictions is decreased to roughly a factor of 4. The model performs very well at the highest temperature T =

1193 K, P = 5.1 atm condition, with the agreement between the model predictions and experimental observations of ethane falling within 30%.

2.3.1.6 Ethene

Ethene production is well predicted by the model across all four experimental conditions. The largest difference is seen at the lowest temperature T = 965 K, P = 5.2 atm condition, with the experimentally observed concentrations being within a factor of 2 – 3 relative to model predictions. Additionally, at this condition there appears to be a slight delay of a few milliseconds in ethene production where the model shows a sharp rise is production occurring at EOC while the experimental observations appear to increase sharply within the 5 – 10 ms range. At the remaining conditions, there is good agreement between the model and the experimental results. At T = 1067 K, P = 4.4 atm and T = 1074 K, P = 10.0 atm the observed ethene production is within 30% and 70% of the model predictions respectively, and a difference of 70% is also observed at the T = 1193 K, P = 5.1 atm condition.

2.3.1.7 Acetylene

Acetylene was only observed experimentally at the highest temperature T = 1193 K, P = 5.1 atm condition since production of acetylene was below the detectable limit for the remaining three conditions. The model performed well at predicting acetylene production at this condition, and experimental observations were within 70% of model predictions.

2.3.1.8 Methane

Methane production showed generally good agreement with the model predictions across all four experimental conditions. Like the results for ethene, methane production at the lowest temperature T = 965 K, P = 5.2 atm condition was observed to increase at a slightly delayed time relative to model expectations; however, after 20 ms the experimental observations showed very good agreement with the model. At T = 1067 K, P = 4.4 atm and T = 1074 K, P = 10.0 atm the observed values for methane were within 60% and 80% of the model predictions respectively, and a difference of 70% is observed at the T = 1193 K, P = 5.1 atm condition.

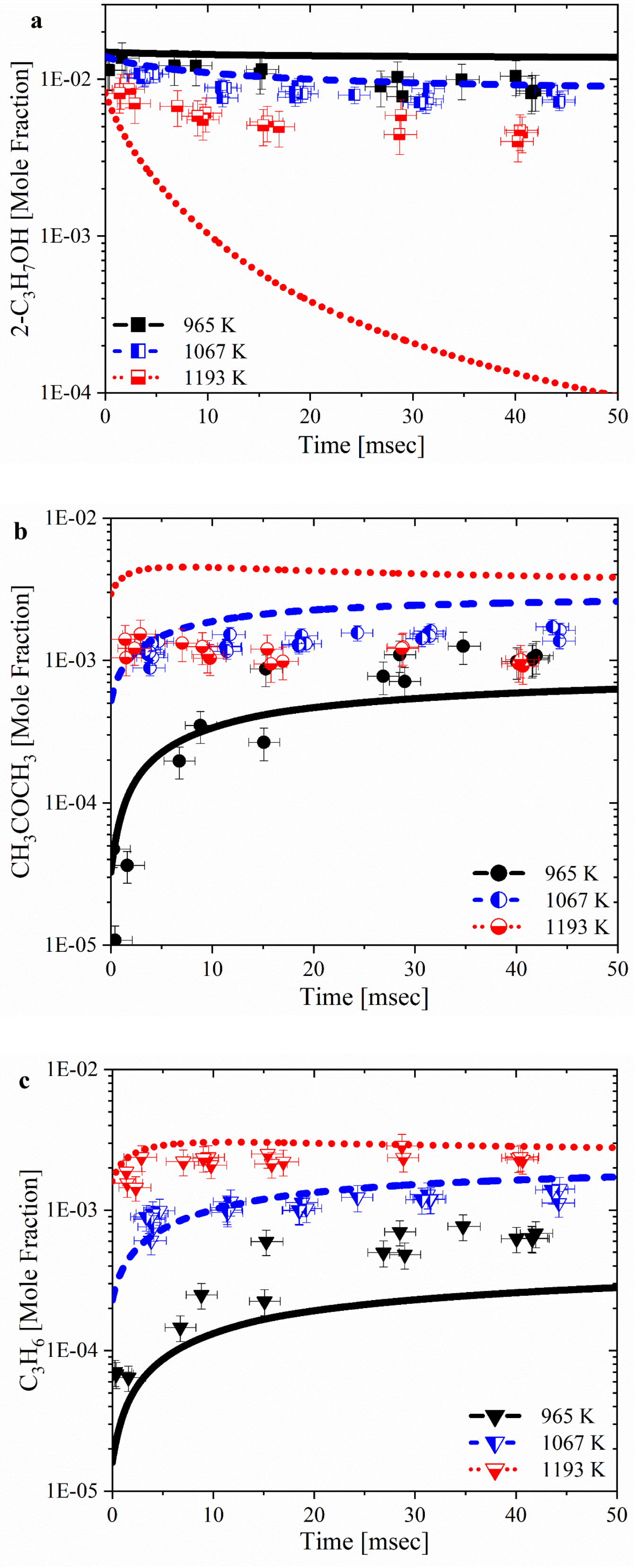
a
2-C_3H_7OH [Mole Fraction]
1E-02
1E-03
1E-04
0
10
20
30
40
50
Time [msec]
965 K
1067 K
1193 K
b
CH_3COCH_3 [Mole Fraction]
1E-02
1E-03
1E-04
1E-05
0
10
20
30
40
50
Time [msec]
965 K
1067 K
1193 K
c
C_3H_6 [Mole Fraction]
1E-02
1E-03
1E-04
1E-05
0
10
20
30
40
50
Time [msec]
965 K
1067 K
1193 K

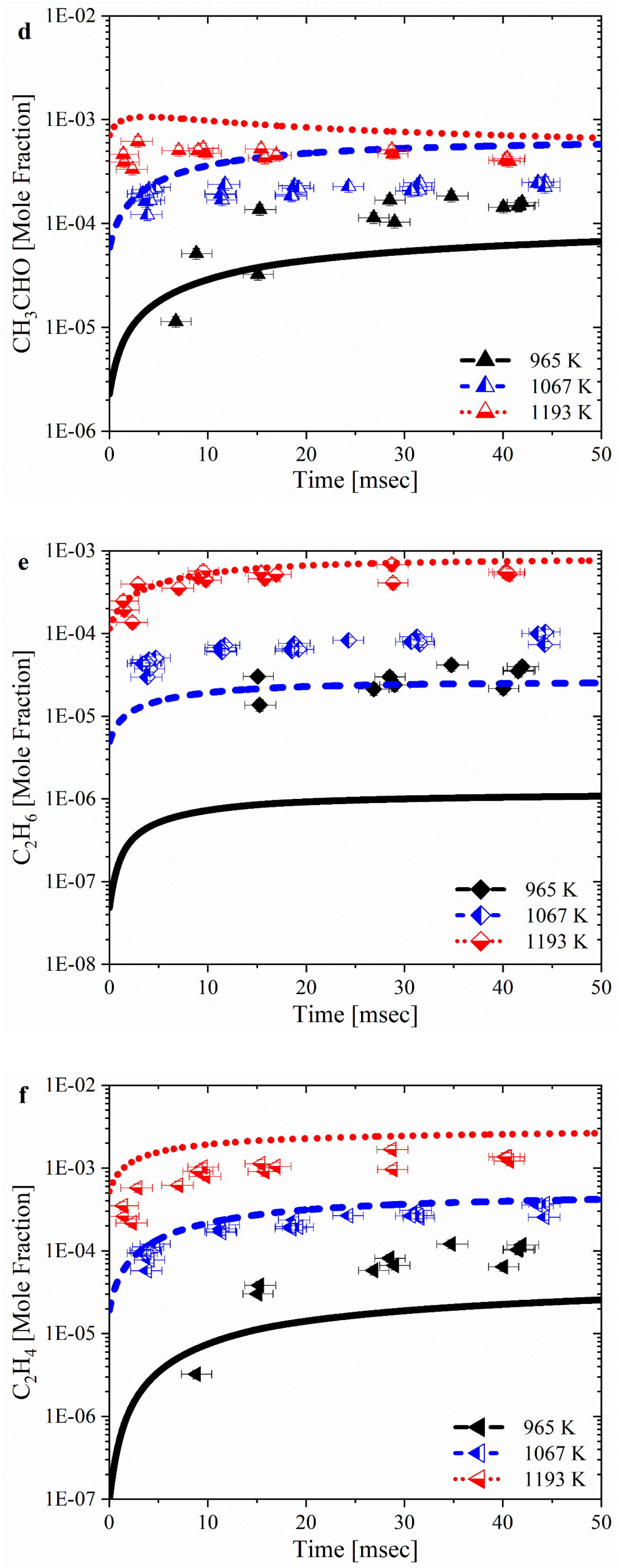
d
1E-02
1E-03
1E-04
1E-05
1E-06
CH_3CHO [Mole Fraction]
0
10
20
30
40
50
Time [msec]
965 K
1067 K
1193 K
e
1E-03
1E-04
1E-05
1E-06
1E-07
1E-08
C_2H_6 [Mole Fraction]
0
10
20
30
40
50
Time [msec]
965 K
1067 K
1193 K
f
1E-02
1E-03
1E-04
1E-05
1E-06
1E-07
C_2H_4 [Mole Fraction]
0
10
20
30
40
50
Time [msec]
965 K
1067 K
1193 K

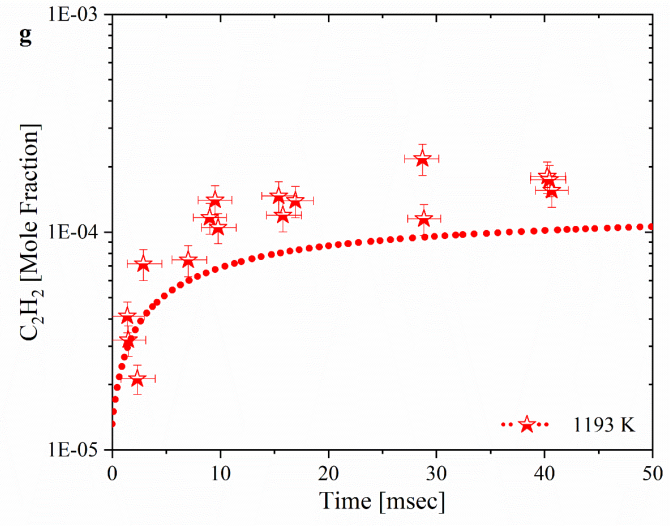

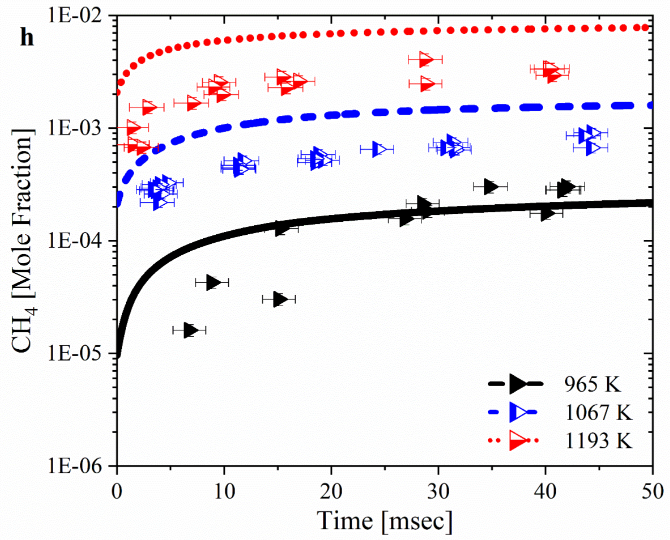

Figure 2.6: Comparison of the effects of temperature on the experimental results (symbols, where error bars are the experimental uncertainties) and model predictions (lines) for 1.5% *iso*-propanol pyrolysis at T = 965 K, P = 5.2 atm (black), T = 1067 K, P = 4.4 atm (blue), and T = 1193 K, P = 5.1 atm (red).

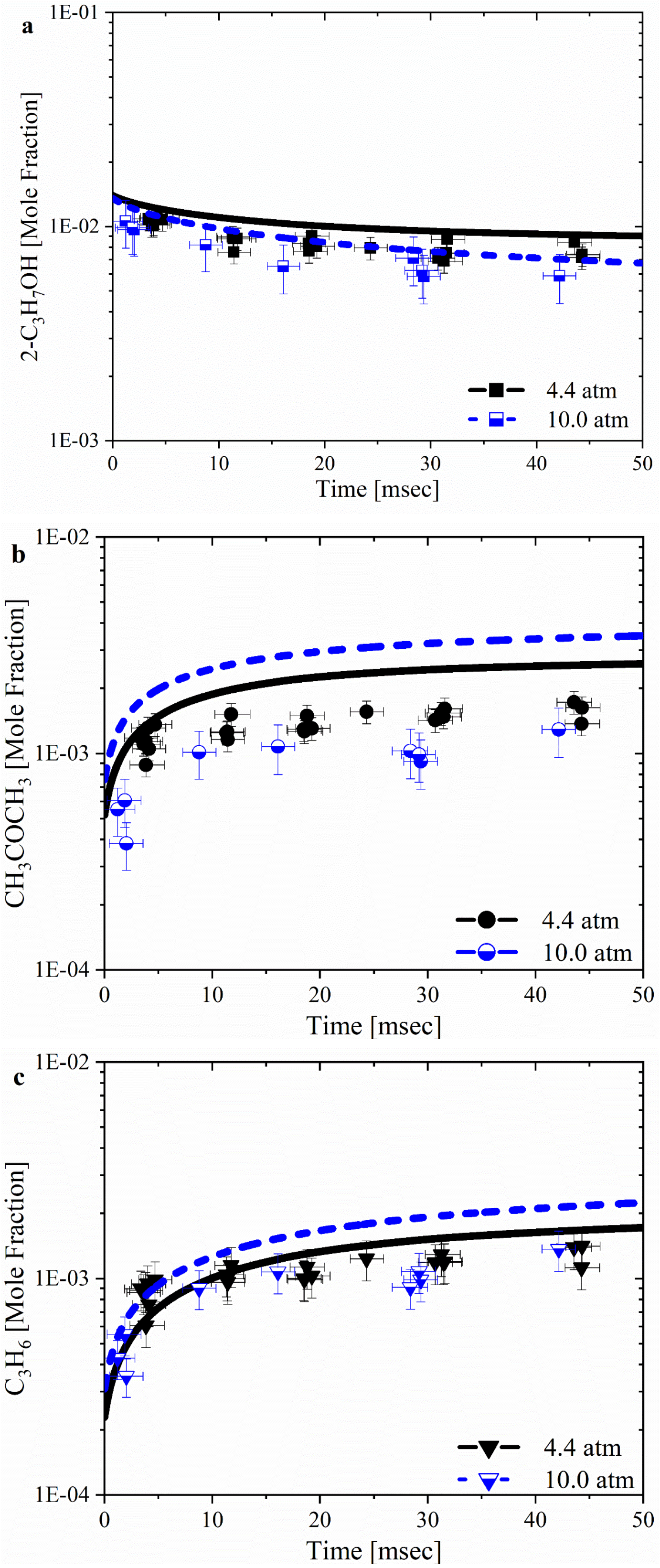
a
1E-01
1E-02
1E-03
2-C_3H_7OH [Mole Fraction]
0
10
20
30
40
50
Time [msec]
4.4 atm
10.0 atm
b
1E-02
1E-03
1E-04
CH_3COCH_3 [Mole Fraction]
0
10
20
30
40
50
Time [msec]
4.4 atm
10.0 atm
c
1E-02
1E-03
1E-04
C_3H_6 [Mole Fraction]
0
10
20
30
40
50
Time [msec]
4.4 atm
10.0 atm

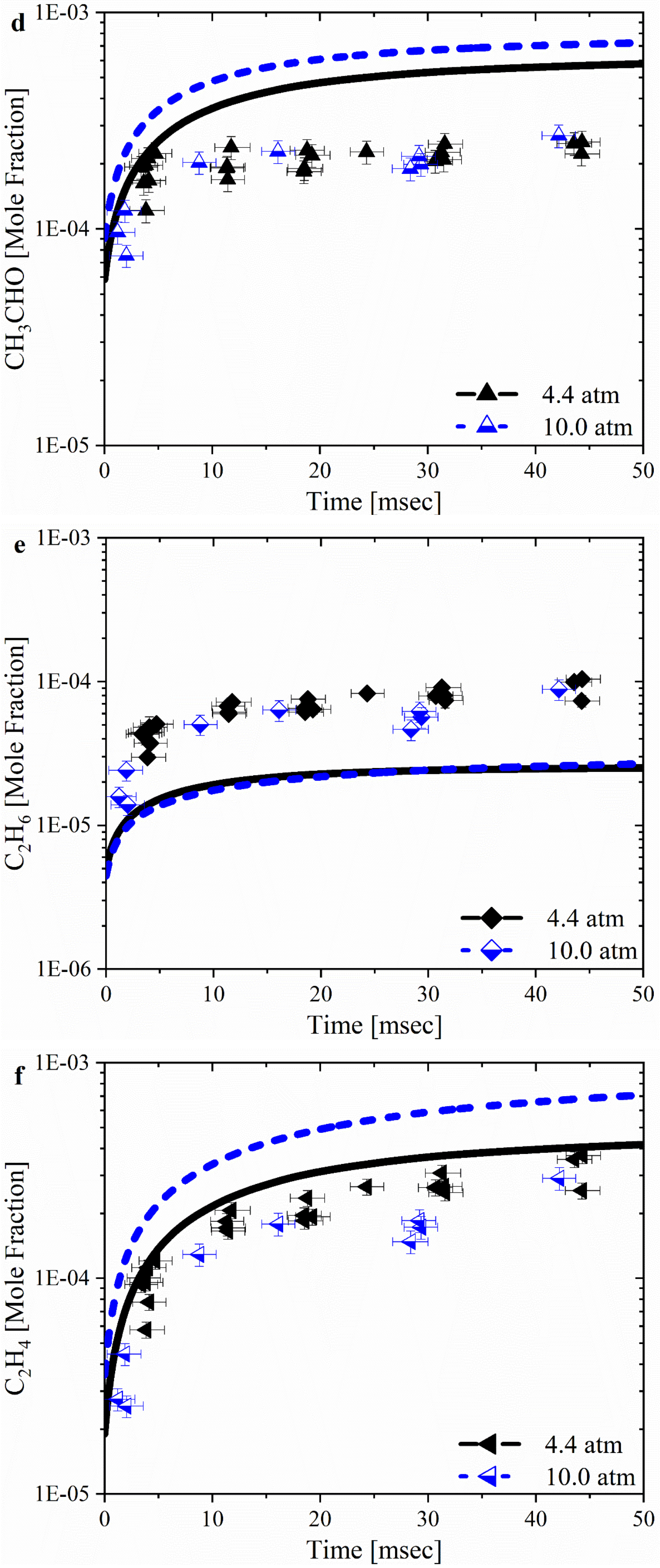
d
1E-03
1E-04
1E-05
CH_3CHO [Mole Fraction]
0
10
20
30
40
50
Time [msec]
4.4 atm
10.0 atm
e
1E-03
1E-04
1E-05
1E-06
C_2H_6 [Mole Fraction]
0
10
20
30
40
50
Time [msec]
4.4 atm
10.0 atm
f
1E-03
1E-04
1E-05
C_2H_4 [Mole Fraction]
0
10
20
30
40
50
Time [msec]
4.4 atm
10.0 atm

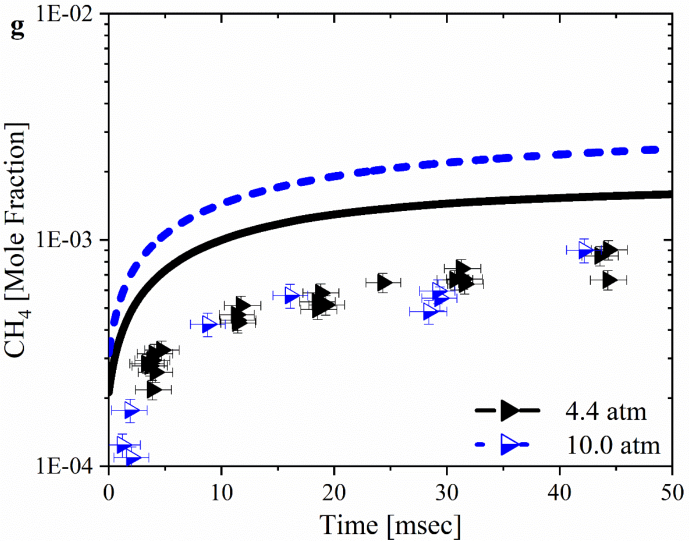

Figure 2.7: Comparison of the effects of pressure on the experimental results (symbols, where error bars are the experimental uncertainties) and model predictions (lines) for 1.5% *iso*-propanol pyrolysis at T = 1067 K, P = 4.4 atm (black) and T = 1074 K, P = 10.0 atm (blue).

2.3.2 Discussion

Due to the quenching of sampled gas required to measure species concentrations, the possibility of radical recombination impacting species measurements must be considered as a potential source of error. However, as shown in **Figure 2.8**, predictions for radical concentrations are very low, with the only meaningful concentration being of the CH_3 radical around the time of EOC that is still at low enough concentration that it is not expected to be a source of error in the present work.

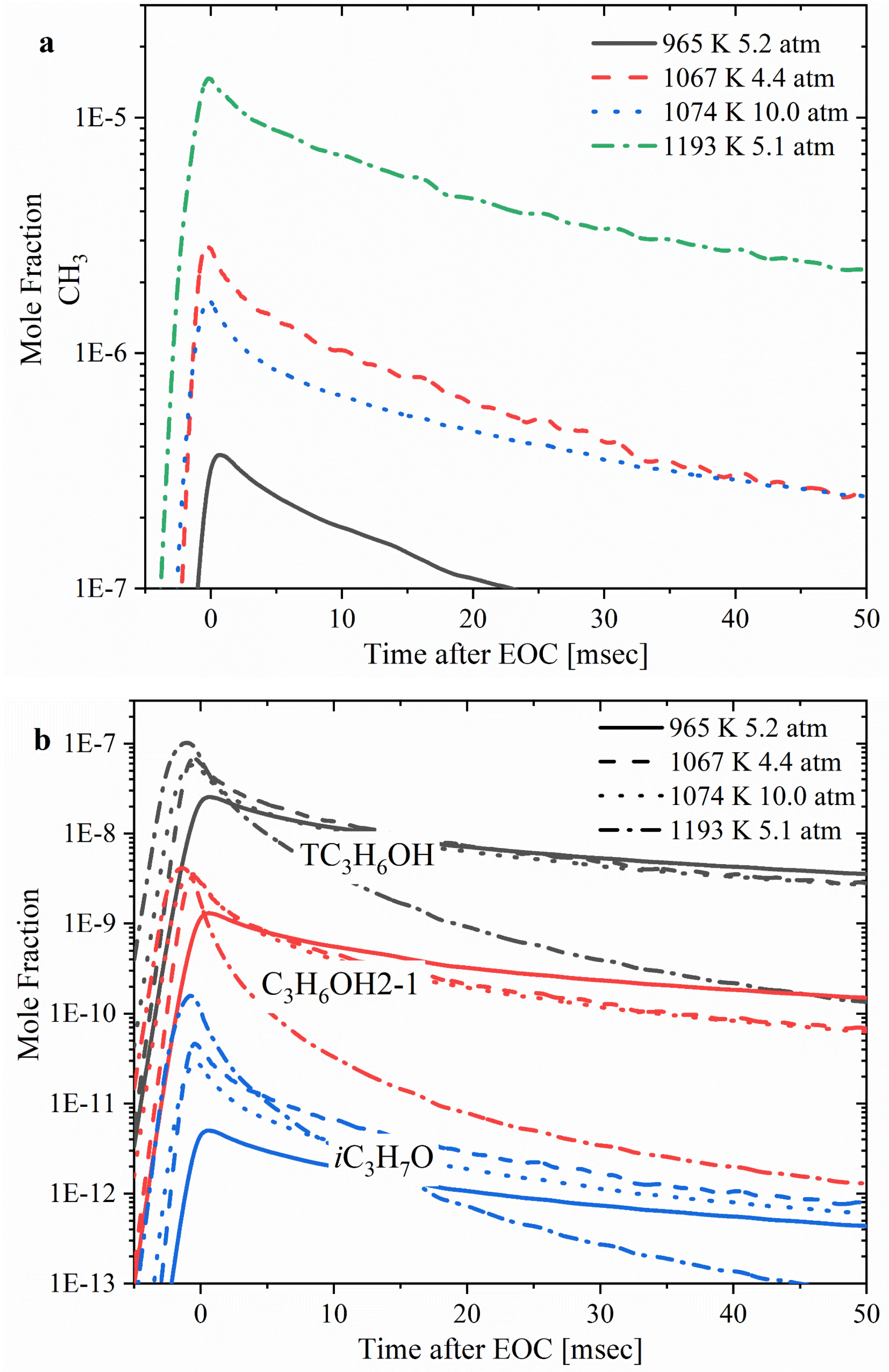
a
Mole Fraction
CH$_3$
1E-5
1E-6
1E-7
0
10
20
30
40
50
Time after EOC [msec]
965 K 5.2 atm
1067 K 4.4 atm
1074 K 10.0 atm
1193 K 5.1 atm
b
Mole Fraction
1E-7
1E-8
1E-9
1E-10
1E-11
1E-12
1E-13
0
10
20
30
40
50
Time after EOC [msec]
965 K 5.2 atm
1067 K 4.4 atm
1074 K 10.0 atm
1193 K 5.1 atm
TC$_3$H$_6$OH
C$_3$H$_6$OH2-1
*i*C$_3$H$_7$O

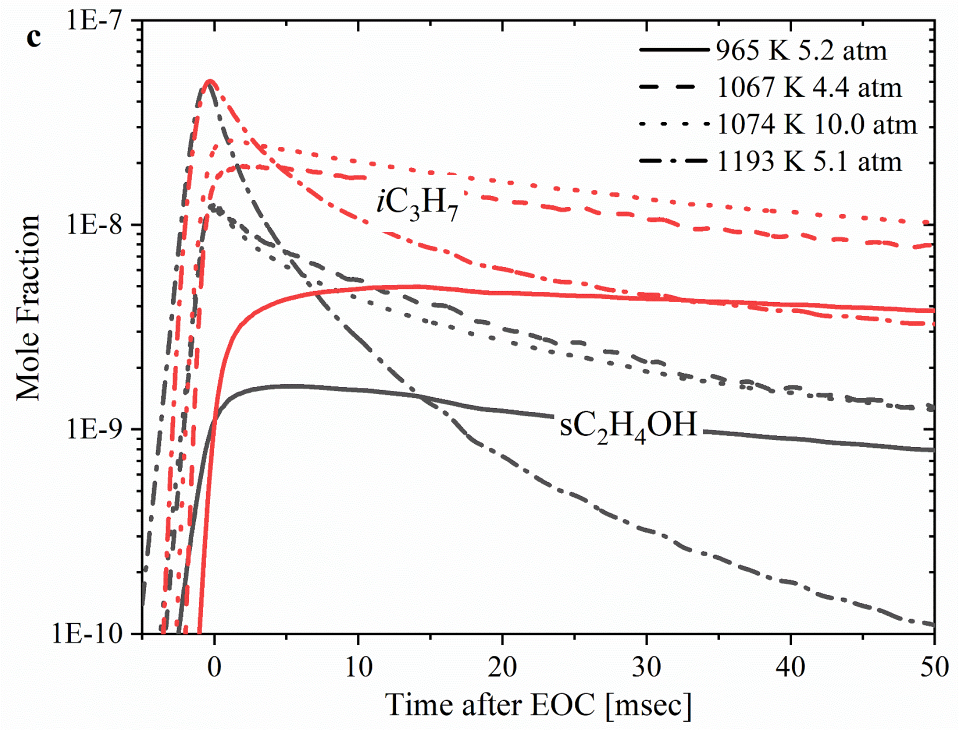

Figure 2.8: Predicted mole fractions of key radicals produced over time at each of the four experimental conditions studied. (a) CH3 production (b) Radicals produced by the H-atom abstraction reactions of *iso*-propanol (c) Other important radicals identified by the sensitivity analysis of *iso*-propanol.

The carbon balance for the system identified that a majority of the carbon was captured by the intermediate species and *iso*-propanol that were measured experimentally at each of the four conditions of interest, with 74 – 86% of the carbon present in the system at early sampling times (< 10 ms) and 60 – 74% at later sampling times (> 30 ms). The large difference in *iso*-propanol concentration between the experimental measurements and model predictions at the T = 1193 K condition also leads to a large discrepancy in the carbon balance between experimental conditions and model predictions at this temperature. Due to the difference in *iso*-propanol concentration between the experimental measurements and the model predictions at this condition (shown in **Figure 2.6a**), there is a ~30% difference in carbon accounted for due to *iso*-propanol at sampling times after 30 ms. The good agreement between the model predictions and the experimental results for the intermediate species measured at T = 1193 K, despite the large discrepancy for *iso*-propanol, indicates that the carbon resulting from the *iso*-propanol consumption is not accounted for by those stable intermediates but is instead being distributed to other species that were not measured in the present experimental setup. This indicates that the agreement between the intermediate species concentrations predicted by the model and those measured experimentally may simply be a coincidence, and revisions to the rate coefficients and branching fractions in the reactions responsible for *iso*-propanol pyrolysis may be needed.

Sensitivity analyses and reaction path diagrams were conducted at the four conditions studied in the present work to better understand the major pathways in the Saggese et al. [53] mechanism and identify possible explanations for the discrepancies between it and the experimental observations. The sensitivity analysis results for *iso*-propanol as temperature and pressure are varied are provided in **Figure 2.9**. **Figure 2.9(a)** and **Figure 2.9(b)** show the normalized sensitivity as temperature is varied at both 5 ms and 25 ms respectively, while **Figure 2.9(c)** and **Figure 2.9(d)** show the sensitivity as pressure is varied at 5 ms and 25 ms respectively. These results show that *iso*-propanol has the most sensitivity to changes in the H-atom abstraction reactions for the +CH_3 and +H reactions that produce TC_3H_6OH and the fuel (+M) reaction that produces CH_3 and SC_2H_4OH radicals. These results hold mostly true for all three temperature conditions at both times, but at the highest temperature T = 1193 K the fuel (+M) reaction that produces propene and water increases in importance at later times, while it does not have as great of an impact for the T = 1067 K and the T = 965 K conditions. All three conditions also show a similar sensitivity to limiting *iso*-propanol consumption through the competition for +CH_3 through the production of ethane by two CH_3 radicals and +H radicals through the production of $C_3H_{5\text{-}A}$ by the H-atom abstraction reaction from propene. Sensitivity to these pathways is also identified through variations in pressure, with many of the same reactions identified in the sensitivity analysis for pressure variation in **Figure 2.9(c)** and **Figure 2.9(d)**. The lack of major changes to the sensitivity analysis in response to pressure changes is expected based on the similarity in species production identified in the experimental results and lack of large differences in model predictions for these species traces in response to a roughly 2-fold increase in pressure. Sensitivity analyses for the other measured species are provided in **Appendix A**.

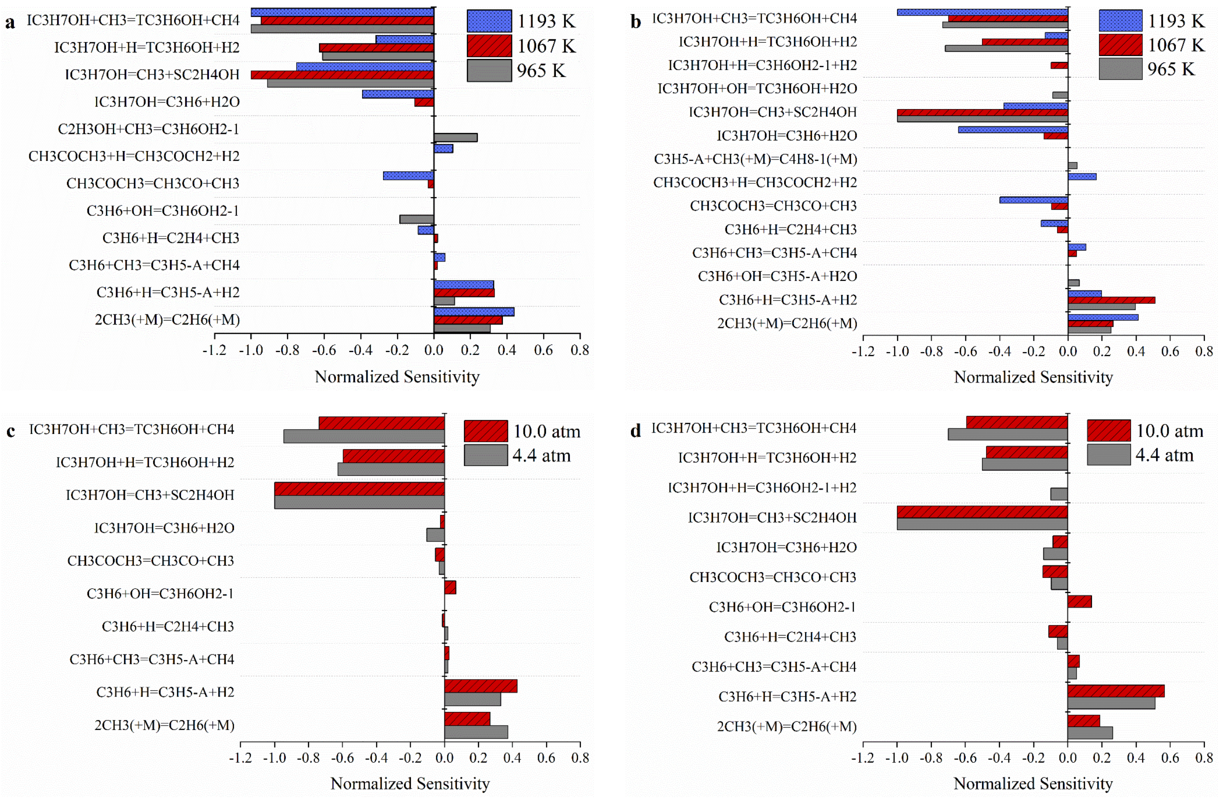

Figure 2.9: Sensitivity analyses of *iso*-propanol pyrolysis as temperature is varied at (a) 5 ms and (b) 25 ms and as pressure is varied at (c) 5 ms and (d) 25 ms.

Reaction path diagrams for the stable species measured in the present work were created using rate of production analysis of the Saggese et al. [53] mechanism at both 5 ms and 25 ms. As identified by the sensitivity analyses, the pyrolysis system is predicted to be predominantly controlled by the thermal decomposition of *iso*-propanol (+M) and the *iso*-propanol +CH_3 and +H reactions. The *iso*-propanol +OH reactions are also important to the consumption of *iso*-propanol, but at much lower rates than the +CH_3, +H, and thermal decomposition (+M) reactions. Of the species measured experimentally, methane and propene are direct products of these reactions, whereas other intermediates are created in subsequent steps. A majority of the methane is produced by the *iso*-propanol + CH_3 reactions, specifically the reaction producing TC_3H_6OH, making it the only species primarily produced directly as a first-order product of reactions that consume *iso*-propanol. Propene is produced by the thermal decomposition of *iso*-propanol (+M) but has a competing major pathway where it is also formed by the decomposition of $C_3H_6OH_{2\text{-}1}$ (+M).

Second order species identified by the reaction path diagram are ethane, ethene, and acetone. Ethane is almost exclusively produced by the combination of methyl radicals that directly competes with *iso*-propanol consumption in the *iso*-propanol +CH_3 reactions. Acetone is a product of H elimination from the TC_3H_6OH radical initially formed by the H-atom abstraction reactions for *iso*-propanol. Ethene is formed through two main pathways: the C_3H_6 +H reaction is responsible for most of its production and additional production results from the C_2H_3OH +H pathway. The C_2H_3OH +H reactions are also responsible for production of the third-order intermediate species measured, acetaldehyde, in conjunction with the C_2H_3OH (+M) reactions. The final measured species shown in the reaction path diagrams is acetylene, which was only measured at the highest temperature condition, T = 1193 K. It is a fourth-order species produced by the C_2H_3 (+M) reaction, with C_2H_3 produced by the C_2H_4 +H, +OH, and +CH_3 reactions.

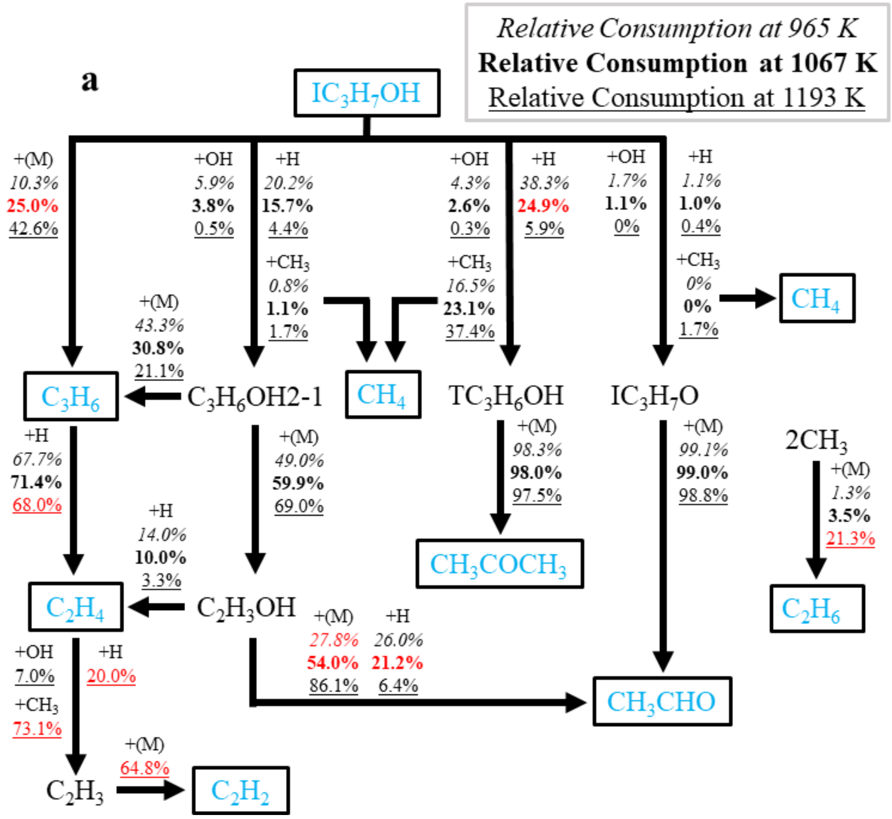

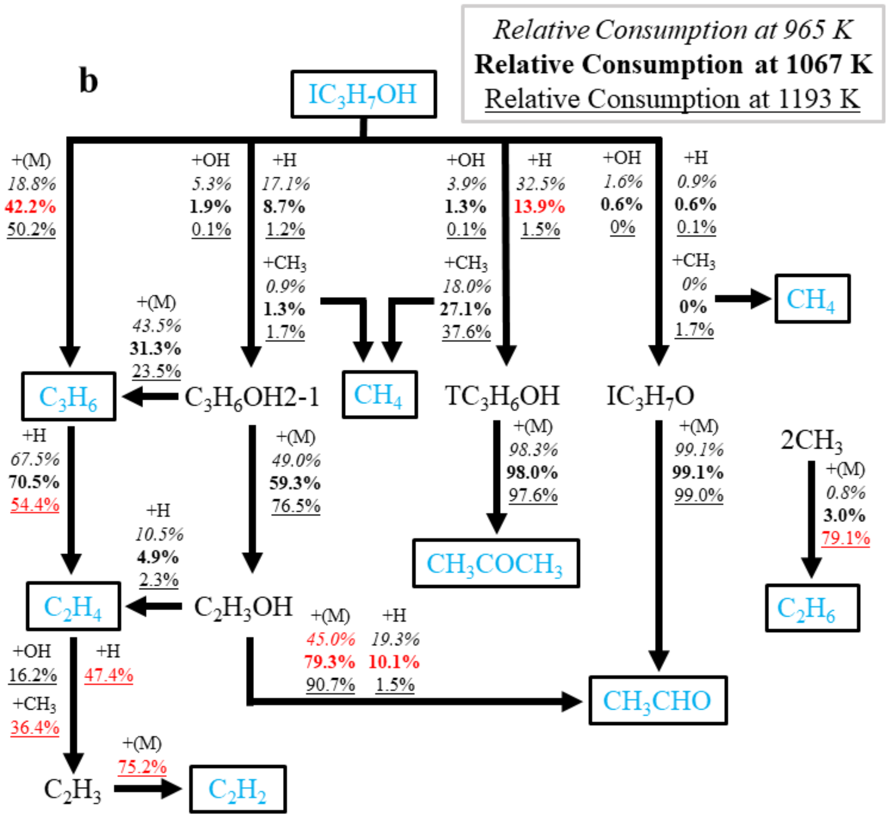

Figure 2.10: Major reaction pathways for pyrolysis of 1.5% *iso*-propanol mixtures and how relative consumption rates change in response to increases in temperature at (a) 5 ms and (b) 25 ms. Species in boxes and blue font indicate the species measured experimentally. The red text identifies conditions where there is a change of greater than 10% in that reaction pathway between the 5 ms and 25 ms conditions.

2.3.2.1 Effects of Temperature on Reaction Pathways

Figure 2.10(a) and **Figure 2.10(b)** highlight the impact that changes in temperature have on the major reaction pathways for *iso*-propanol pyrolysis at both 5 ms and 25 ms after EOC. The initial thermal decomposition reaction, *iso*-propanol (+M), that results in the formation of propene becomes more prominent as the temperature is increased, consuming 10.3% and 18.8% at 5 ms and 25 ms of *iso*-propanol respectively for the T = 963 K condition that then increases to 42.6% and 50.2% at the 5 ms and 25 ms times for the T = 1193 K condition. In response to the consumption of almost half of the *iso*-propanol at the highest temperature condition being accounted for by this pathway, the fraction of *iso*-propanol consumed by alternative pathways are greatly reduced. Specifically, the formation of $C_3H_6OH_{2\text{-}1}$ and TC_3H_6OH through the IC_3H_7OH +H reactions show the most dramatic reduction in relative consumption at T = 1193 K when compared to T = 965 K. The production of $C_3H_6OH_{2\text{-}1}$ by the IC_3H_7OH +H reaction is reduced from 20.2% to 4.4% at 5 ms after EOC and 17.1% to 1.2% at 25 ms after EOC. The production of TC_3H_6OH by the IC_3H_7OH +H reaction is similarly reduced from 38.3% to 5.9% at 5 ms after EOC and 32.5% to 1.5% at 25 ms after EOC. Reductions in relative consumption are shown in response to an increase in temperature for the production of $C_3H_6OH_{2-1}$ and TC_3H_6OH through the IC_3H_7OH +OH reactions, but these reactions accounted for less than 6% of relative consumption of *iso*-propanol at their maximum. While the production of TC_3H_6OH is reduced by the +H and +OH pathways at the highest temperature, it is increased by higher relative consumption rates of *iso*-propanol +CH_3. The relative consumption rate for this reaction is increased from 16.5% to 37.4% at 5 ms and 18.0% to 37.6% at 25 ms, also leading to an increase in production of methane in response to an increase in temperature. Propene production through the $C_3H_6OH_{2-1}$ (+M) reaction is decreased in response to temperature increases, with more of the C_3H_6OH2-1 going to the formation of C_2H_3OH responsible for ultimately forming acetaldehyde. The pathway responsible for the formation of acetone remains relatively constant in response to increases in temperature, since almost all of the TC_3H_6OH is converted to acetone. As such, changes in the formation of TC_3H_6OH will heavily impact the production of acetone.

Other notable impacts of increases in temperature are the increase in production of ethane from the combination of two methyl radicals, which shows a dramatic increase at the 25 ms after EOC condition from 0.8% of methyl radicals consumed by production of ethane at T = 965 K increasing all the way to 79.1%. Additionally, C_2H_3OH becomes much more important for the formation of acetaldehyde and less of a factor in the formation of ethene in response to an increase in temperature.

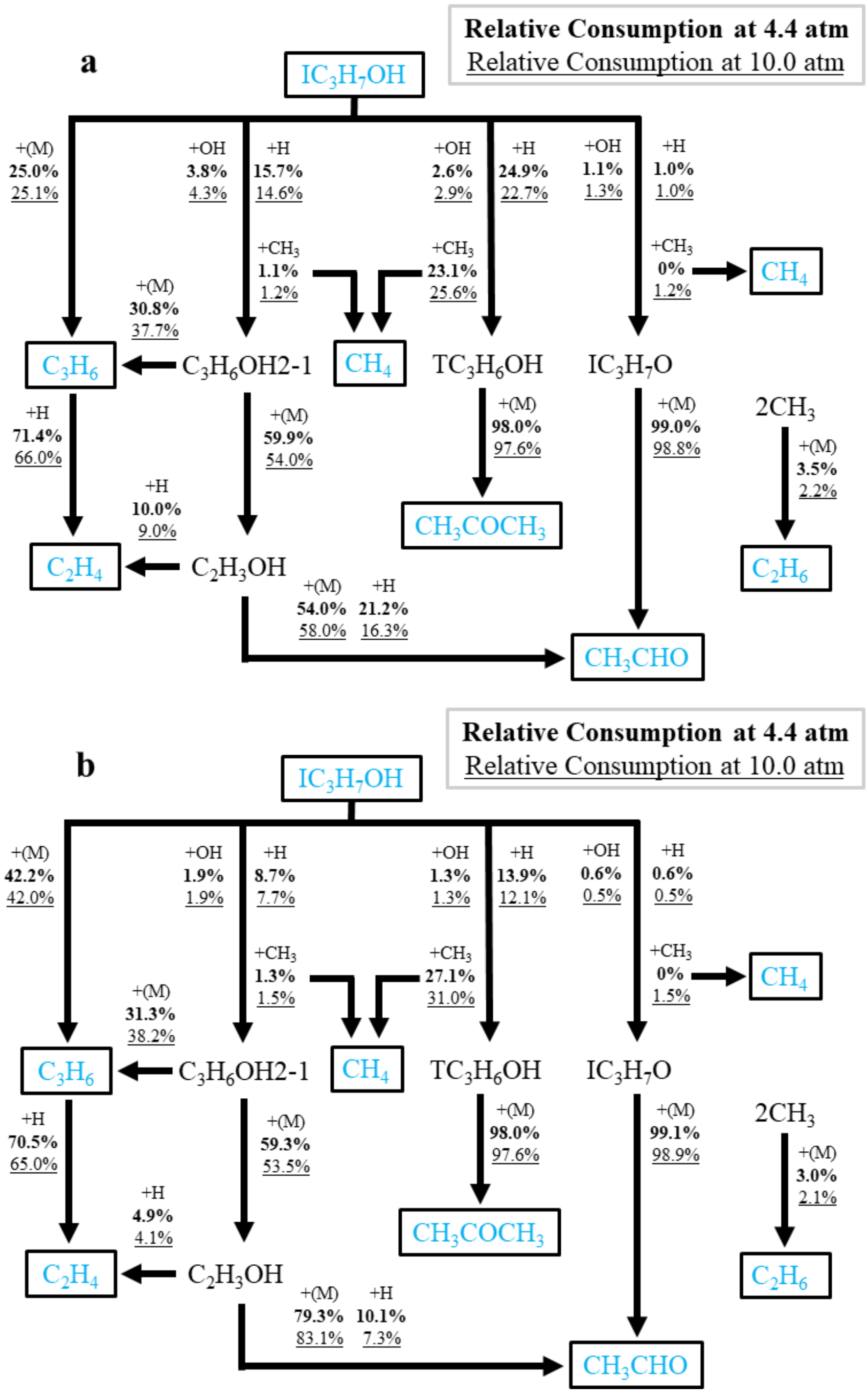

Figure 2.11: Major reaction pathways for pyrolysis of 1.5% *iso*-propanol mixtures and how relative consumption rates change in response to increases in pressure at (a) 5 ms and (b) 25 ms. Species in boxes and blue font indicate the species measured experimentally.

2.3.2.2 Effects of pressure on reaction pathways

Figure 2.11(a) and **Figure 2.11(b)** indicate that pyrolysis of *iso*-propanol has lower sensitivity to a pressure increase compared to increases in temperature. A more than two-fold pressure increase leads to a less than 2% change in relative consumption rates for all the initial *iso*-propanol thermal decomposition and H-atom abstraction reactions except for the *iso*-propanol +CH_3 reaction responsible for the formation of TC_3H_6OH, which still only shows a ~4% increase. The lack of large changes in the reaction pathways in response to this increase in pressure is supported by the similar species concentrations observed experimentally at both the P = 4.4 atm and P = 10.0 atm conditions.

2.4 Conclusions

The results of this work provide the first experimental data of stable intermediates formed during *iso*-propanol pyrolysis at a range of intermediate temperatures (T = 965 – 1193 K) and pressures (P = 4.4 – 10.0 atm) using a rapid compression facility. The measurements quantified the concentrations of seven intermediate species and *iso*-propanol and showed significant formation of acetone, propene, acetaldehyde, ethene, ethane, and methane for T = 965 – 1074 K and P = 4.4 – 10.0 atm. The formation of acetylene was also observed, but only at T = 1193 K and P = 5.1 atm. A carbon balance identified that a majority of carbon present in the system was present in the intermediate species and *iso*-propanol concentrations that were measured experimentally across the four conditions of interest. At early sampling times less than 10 ms, between 74 – 86% of the initial carbon in the *iso*-propanol was captured by the measured species. At the later sampling times after 30 ms, between 60 – 74% of initial carbon was captured by the experimentally measured species. The 30% difference in carbon between *iso*-propanol measured experimentally and predicted by the model at the T = 1193 K condition that was unaccounted for by the intermediate species suggests that the highest temperature condition reactions likely need the most refining, despite the good agreement shown by the intermediate species.

The species concentration measurements showed generally good agreement with the model predictions using the mechanism from Saggese et al. [53], with key exceptions of the overprediction of *iso*-propanol consumption at T = 1193 K by more than an order of magnitude and the underprediction of ethane production at T = 965 K by more than an order of magnitude. The overprediction of *iso*-propanol consumption at the highest temperature condition is the most notable considering the remaining measured species were within a factor of three of the concentrations predicted by the model. This indicates additional refinement is needed in the reaction pathways and branching fractions most responsible for *iso*-propanol pyrolysis at this condition, specifically the *iso*-propanol (+M), +H, and +CH_3 pathways. A discrepancy of this magnitude also suggests that there may be additional reaction pathways or branching fractions not accounted for in the reaction mechanism and warrants further study. The underprediction of ethane at the lowest temperature condition also suggests a need for refining of the branching fractions responsible for ethane productions at this condition. Since ethane is primarily produced through the combination of methyl radicals, the competition between the *iso*-propanol H-atom abstraction reactions responsible for producing methane (*iso*-propanol +CH_3) and the methyl combination reaction responsible for producing ethane likely needs additional refinement for the reaction rates and branching fractions at this condition.

The intermediate species concentrations were more sensitive to temperature (specifically increases of 100 – 120 K increments) compared with the sensitivity to pressure (specifically an increase by more than two-fold). As expected, the kinetic modeling comparisons indicate the most important reactions for *iso*-propanol pyrolysis at the conditions studied are the thermal decomposition of *iso*-propanol (+M) and the H-atom abstraction reactions, specifically *iso*-propanol +H and +CH_3. The results of this work are essential benchmarks for species concentrations at low-to-intermediate temperatures and provide speciation data that can be used to improve rate coefficients and branching fractions for the *iso*-propanol thermal decomposition and *iso*-propanol H-atom abstraction reactions at conditions where the highest discrepancies were identified.

2.5 References

[1] International Energy Agency, World energy outlook, 2020

[2] J.M. Bergthorson, M.J. Thomson, A review of the combustion and emissions properties of advanced transportation biofuels and their impact on existing and future engines, Renew. Sustain. Energy Rev., 42 (2015), pp. 1393-1417

[3] A. Demirbas, Biofuels sources, biofuel policy, biofuel economy and global biofuel projections Energy Convers. Manag., 49 (8) (2008), pp. 2106-2116

[4] A. Demirbas, Competitive liquid biofuels from biomass, Appl. Energy, 88 (1) (2011), pp. 17-28

[5] A.K. Agarwal, Biofuels (alcohols and biodiesel) applications as fuels for internal combustion engines, Prog. Energy Combust. Sci., 33 (2007), pp. 233-271

[6] D.J. Gaspar, B.H. West, D. Ruddy, T.J. Wilke, E. Polikarpov, T.L. Alleman, et al., Top ten blendstocks derived from biomass for turbocharged spark ignition engines: bio-blendstocks with potential for highest engine efficiency, Pacific Northwest National Lab (PNNL); 2019. PNNL-28713.

[7] Keskin A, Gürü M. The effects of ethanol and propanol additions into unleaded gasoline on exhaust and noise emissions of a spark ignition engine. Energ Source Part A. 2011;33:2194-2205.

[8] Masum B,Masjuki HH, KalamM, Palash S, HabibullahM. Effect of alcohol–gasoline blends optimization on fuel properties, performance and emissions of a SI engine. J Clean Prod. 2015;86:230-237.

[9] Xingcai L, Yuchun H, Libin Zu, Linlin A, Zhen H. Heat release analysis on combustion and parametric study on emissions of HCCI engines fueled with 2-propanol/n-heptane blend fuels. Energy Fuel. 2006;20:1870-1878.

[10] Calam A, Aydoğan B, Halis S. The comparison of combustion, engine performance and emission characteristics of ethanol, methanol, fusel oil, butanol, isopropanol and naphtha with n-heptane blends on HCCI engine. Fuel. 2020;266:117071.

[11] Uyumaz A. An experimental investigation into combustion and performance characteristics of an HCCI gasoline engine fueled with n-heptane, isopropanol and n-butanol fuel blends at different inlet air temperatures. Energy Convers Manag. 2015;98:199-207.

[12] Gong J, Zhang Y, Tang C, Huang Z. Emission characteristics of *iso*-propanol/gasoline blends in a spark-ignition engine combined with exhaust gas re-circulation. Therm Sci. 2014;18:269-277.

[13] Li W, Zhang Y, Mei B, et al. Experimental and kinetic modeling study of n-propanol and i-propanol combustion: flow reactor pyrolysis and laminar flame propagation. Combust Flame. 2019;207:171-185.

[14] Cooper, SP, Mulvihill, CR, Mathieu, O, Petersen, EL. Isopropanol dehydration reaction rate kinetics measurement using H2O time histories. Int J Chem Kinet. 2021; 53: 536– 547.

[15] S.M. Sarathy, P. Oßwald, N. Hansen, K. Kohse-Höinghaus, Alcohol combustion chemistry, Prog. Energy Comb. Sci. 44 (2014) 40-102.

[16] P. Zhang, S. Li, Y. Wang, W. Ji, W. Sun, B. Yang, X. He, Z. Wang, C.K. Law, F. Zhang, Measurement of reaction rate constants using RCM: A case study of decomposition of dimethyl carbonate to dimethyl ether. Combust. Flame 183 (2017) 30–38.

[17] Michael V. Johnson, S. Scott Goldsborough, Zeynep Serinyel, Peter O'Toole, Eoin Larkin, Grainne O'Malley, and Henry J. Curran, A shock tube study of n- and *iso*-propanol ignition, Energy & Fuels 2009 23 (12), 5886-5898.

[18] Xingjia Man, Chenglong Tang, Jiaxiang Zhang, Yingjia Zhang, Lun Pan, Zuohua Huang, Chung K. Law, An experimental and kinetic modeling study of n-propanol and i-propanol ignition at high temperatures, Combustion and Flame, Volume 161, Issue 3, 2014, Pages 644-656.

[19] Jouzdani S, Zhou A, Akih-Kumgeh B. Propanol isomers: investigation of ignition and pyrolysis time scales. Combust Flame. 2017;176:229-244.

[20] Akih-Kumgeh B, Bergthorson JM. Ignition of C3 oxygenated hydrocarbons and chemical kinetic modeling of propanal oxidation. Combust Flame. 2011;158:1877-1889.

[21] Cheng, S., Kang, D., Goldsborough, S. S., Saggese, C., Wagnon, S. W., & Pitz, W. J. (2021). Experimental and modeling study of C2–C4 alcohol autoignition at intermediate temperature conditions. Proceedings of the Combustion Institute, 38(1), 709-717.

[22] Goldsborough, S. S., Cheng, S., Kang, D., Saggese, C., Wagnon, S. W., & Pitz, W. J. (2021). Effects of isoalcohol blending with gasoline on autoignition behavior in a rapid compression

machine: Isopropanol and isobutanol. Proceedings of the Combustion Institute, 38(4), 5655-5664.

[23] Veloo PS, Egolfopoulos FN. Studies of n-propanol, *iso*-propanol, and propane flames. Combust Flame. 2011;158:501-510.

[24] Smith SR, Gordon AS. Studies of diffusion flames. II. Diffusion flames of some simple alcohols. J Phys Chem. 1956;60:1059-1062.

[25] Sinha A, Thomson M. The chemical structures of opposed flow diffusion flames of C3 oxygenated hydrocarbons (isopropanol, dimethoxy methane, and dimethyl carbonate) and their mixtures. Combust Flame. 2004;136:548-556.

[26] Li Y, Wei L, Tian Z, et al. A comprehensive experimental study of low-pressure premixed C3-oxygenated hydrocarbon flames with tunable synchrotron photoionization. Combust Flame. 2008;152:336-359.

[27] Kasper T, Oßwald P, Struckmeier U, Kohse-Höinghaus K, Taatjes CA, et al. Combustion chemistry of the propanol isomers investigated by electron ionization and VUV-photoionization molecular-beam mass spectrometry. Combust Flame. 2009;156:1181-1201.

[28] Frassoldati A, Cuoci A, Faravelli T, et al. An experimental and kinetic modeling study of n-propanol and *iso*-propanol combustion. Combust Flame. 2010;157:2-16.

[29] Togbe C, Dagaut P, Halter F, Foucher F. 2-Propanol oxidation in a pressurized jet-stirred reactor (JSR) and combustion bomb: experimental and detailed kinetic modeling study. Energy Fuel. 2011;25:676-683.

[30] J.S. Heyne, S. Dooley, Z. Serinyel, F.L. Dryer, H. Curran, Decomposition studies of isopropanol in a variable pressure flow reactor, Z. Phys. Chem., 229 (6) (2015), pp. 881-907

[31] Bui B, Zhu R, Lin M. Thermal decomposition of *iso*-propanol: first-principles prediction of total and product-branching rate constants. J Chem Phys. 2002;117:11188-11195.

[32] W. Tsang, Thermal stability of alcohols, Int. J. Chem. Kinet. 8, (1976) 173-192.

[33] Trenwith AB. Thermal decomposition of isopropanol. J Chem Soc Faraday Trans. 1975;71:2405-2412.

[34] M.T. Donovan, X. He, B.T. Zigler, T.R. Palmer, M.S. Wooldridge, A. Atreya, Demonstration of a free-piston rapid compression facility for the study of high temperature combustion phenomena, Combust. Flame 137 (2004) 351-365.

[35] A.B. Mansfield, M.S. Wooldridge, H. Di, X. He, Low-temperature ignition behavior of *iso*-octane, Fuel, Volume 139, 2015, Pages 79-86.

[36] S.M. Walton, X. He, B.T. Zigler, M.S. Wooldridge, A. Atreya, An experimental investigation of *iso*-octane ignition phenomena, Combustion and Flame, Volume 150, Issue 3, 2007, Pages 246-262.

[37] X. He, B.T. Zigler, S.M. Walton, M.S. Wooldridge, A. Atreya, A rapid compression facility study of OH time histories during *iso*-octane ignition, Combustion and Flame, Volume 145, Issue 3, 2006, Pages 552-570.

[38] Dimitris Assanis, Scott W. Wagnon, Margaret S. Wooldridge, An experimental study of flame and autoignition interactions of *iso*-octane and air mixtures, Combustion and Flame, Volume 162, Issue 4, 2015, Pages 1214-1224.

[39] X. He, M.T. Donovan, B.T. Zigler, T.R. Palmer, S.M. Walton, M.S. Wooldridge, A. Atreya, An experimental and modeling study of *iso*-octane ignition delay times under homogeneous charge compression ignition conditions, Combustion and Flame, Volume 142, Issue 3, 2005, Pages 266-275.

[40] Darshan M. A. Karwat, Scott W. Wagnon, Margaret S. Wooldridge, and Charles K. Westbrook The Journal of Physical Chemistry A 2012 116 (51), 12406-12421

[41] Miles A. Burnett, Margaret S. Wooldridge, An experimental investigation of flame and autoignition behavior of propane, Combustion and Flame, Volume 224, 2021, Pages 24-32.

[42] Scott W. Wagnon, Margaret S. Wooldridge, Effects of buffer gas composition on autoignition, Combustion and Flame, Volume 161, Issue 4, 2014, Pages 898-907.

[43] Andrew B. Mansfield, Margaret S. Wooldridge, High-pressure low-temperature ignition behavior of syngas mixtures, Combustion and Flame, Volume 161, Issue 9, 2014, Pages 2242-2251.

[44] Andrew B. Mansfield, Margaret S. Wooldridge, The effect of impurities on syngas combustion, Combustion and Flame, Volume 162, Issue 5, 2015, Pages 2286-2295.

[45] Rachel A. Schwind, Margaret S. Wooldridge, Effects of organic silicon compounds on syngas auto-ignition behavior, Combustion and Flame, Volume 212, 2020, Pages 234-241.

[46] S.M. Walton, X. He, B.T. Zigler, M.S. Wooldridge, An experimental investigation of the ignition properties of hydrogen and carbon monoxide mixtures for syngas turbine applications, Proceedings of the Combustion Institute, Volume 31, Issue 2, 2007, Pages 3147-3154.

[47] Cesar L. Barraza-Botet, Margaret S. Wooldridge, Combustion chemistry of *iso*-octane/ethanol blends: Effects on ignition and reaction pathways, Combustion and Flame, Volume 188, 2018, Pages 324-336.

[48] Cesar L. Barraza-Botet, Jon Luecke, Bradley T. Zigler, Margaret S. Wooldridge, The impact of physicochemical property interactions of *iso*-octane/ethanol blends on ignition timescales, Fuel, Volume 224, 2018, Pages 401-411.

[49] Cesar L. Barraza-Botet, Scott W. Wagnon, and Margaret S. Wooldridge, The Journal of Physical Chemistry A 2016 120 (38), 7408-7418

[50] Darshan M.A. Karwat, Scott W. Wagnon, Paul D. Teini, and Margaret S. Wooldridge The Journal of Physical Chemistry A 2011 115 (19), 4909-4921

[51] Scott W. Wagnon, Cesar L. Barraza-Botet, and Margaret S. Wooldridge The Journal of Physical Chemistry A 2015 119 (28), 7695-7703

[52] Stephen M. Walton, Darshan M. Karwat, Paul D. Teini, Adrienne M. Gorny, Margaret S. Wooldridge, Speciation studies of methyl butanoate ignition, Fuel, Volume 90, Issue 5, 2011, Pages 1796-1804.

[53] Chiara Saggese, Charlotte M. Thomas, Scott W. Wagnon, Goutham Kukkadapu, Song Cheng, Dongil Kang, S. Scott Goldsborough, William J. Pitz, An improved detailed chemical kinetic model for C3-C4 linear and *iso*-alcohols and their blends with gasoline at engine-relevant conditions, Proceedings of the Combustion Institute, Volume 38, Issue 1, 2021, Pages 415-423.

[54] Yang Li, Chong-Wen Zhou, Kieran P. Somers, Kuiwen Zhang, Henry J. Curran, The oxidation of 2-butene: A high pressure ignition delay, kinetic modeling study and reactivity

comparison with isobutene and 1-butene, Proceedings of the Combustion Institute, Volume 36, Issue 1, 2017, Pages 403-411.

[55] Max R. McGillen, Munkhbayar Baasandorj, and James B. Burkholder The Journal of Physical Chemistry A 2013 117 (22), 4636-4656

[56] Gaurav Mittal, Sinéad M. Burke, Varun A. Davies, Bikash Parajuli, Wayne K. Metcalfe, Henry J. Curran, Autoignition of ethanol in a rapid compression machine, Combustion and Flame, Volume 161, Issue 5, 2014, Pages 1164-1171.

[57] Qian Zhao, Yingjia Zhang, Wuchuan Sun, Fuquan Deng, Feiyu Yang, and Zuohua Huang, The Journal of Physical Chemistry A 2019 123 (5), 971-982

[58] Sarah N. Elliott, Kevin B. Moore, Andreas V. Copan, Murat Keçeli, Carlo Cavallotti, Yuri Georgievskii, Henry F. Schaefer, Stephen J. Klippenstein, Automated theoretical chemical kinetics: Predicting the kinetics for the initial stages of pyrolysis, Proceedings of the Combustion Institute, Volume 38, Issue 1, 2021, Pages 375-384.

[59] CHEMKIN, release 10131 (x64); Reaction Design: Sand Diego, 2011.

Chapter 3: An Experimental Investigation of Flame and Autoignition Behavior of Propane

This chapter was published in Combustion and Flame as Miles A. Burnett, Margaret S. Wooldridge, "An experimental investigation of flame and autoignition behavior of propane", February 2021.

3.1 Introduction

Due to the prevalence of propane in natural gas blends, the fundamental chemical structure of propane, and the importance of propane as a primary fuel and intermediate in combustion chemistry, many experimental studies on the autoignition behavior of propane are available in the literature. As outlined in Goyal *et al.* [1] and Samini-Abianeh *et al.* [2], the available data span many different experimental facilities, including shock tubes [3,4,5,6,7,8,9,10,11,12], rapid compression machines (RCMs) [9,13,14], flow reactors [15,16,17,18], and jet stirred reactors [19]. The diversity of experimental approaches has allowed propane combustion data to be collected over a large range of temperatures, pressures, concentrations, and equivalence ratios. Much of the autoignition delay time data for propane comes from high-temperature studies conducted using shock tubes, and the data are generally in good agreement and exhibit relatively low scatter at higher temperatures (e.g., autoignition delay times are within a factor of 2 at temperatures above 1300 K), as seen in the Arrhenius diagram presented in **Figure 3.1**. The data in **Figure 3.1** are for fuel-to-air equivalence ratios of 0.5 (molar basis) and have been normalized by pressure to 10 atm. However, the scatter in the data increases remarkably at lower temperatures, e.g., with over an order of magnitude variation in autoignition delay time at temperatures below 900 K. Unscaled data for the studies cited in **Figure 3.1**, and autoignition delay time results for other equivalence ratios are provided in **Appendix B**. Low temperature autoignition behavior of propane is particularly of interest because propane is the smallest alkane to exhibit negative temperature coefficient (NTC) behavior at lower temperatures (i.e., below 1000 K) [1,13,20,21], and lower temperature combustion strategies are promising means to increase efficiency and reduce emissions in transportation and stationary power generation applications [22,23,24]. However, there are challenges to lower temperature combustion strategies including misfire and reduced control over heat release and reaction rates [22,23]. Accurate understanding of low-temperature combustion characteristics is important for successfully advancing these high-efficiency, low-emissions applications, and ignition delay time data are one important means to develop, quantify, and validate fundamental understanding of combustion at low temperatures.

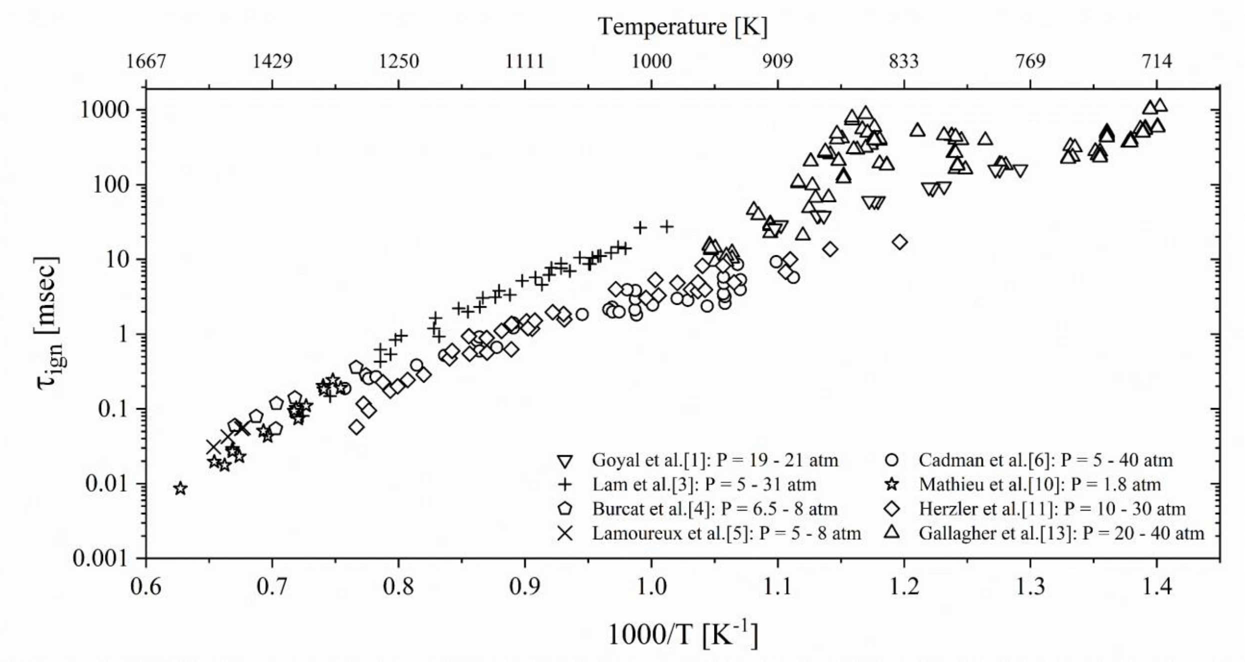

Figure 3.1: Summary of ignition delay time data for propane/air mixtures at ϕ=0.5. The data have been normalized to P = 10 atm using scaling of $\tau_{ign} \propto 1/P$. Unscaled data and ignition delay time results for other equivalence ratios are provided in **Appendix B**.

The specific focus of this chapter is on the interaction between volumetric autoignition and reaction fronts that is more likely to affect ignition data at lower temperatures [25,26,27,28,29,30]. The presence of reaction fronts is attributable to the thermal gradients that are ubiquitous to all experimental facilities. Thermal gradients are created (in part) by mixing induced by the compression process in rapid compression machines and by non-ideal shock behavior and boundary layer effects in shock tubes. The interaction between autoignition and reaction fronts leads to ignition behavior typically referred to as weak, mild, or mixed ignition [25,26,27,28,31] and has been studied in shock tubes [32,33,34,35,36,37] and RCMs [25,26,28]. Earlier work that included high-speed imaging has provided key insights connecting the effects of reaction fronts and autoignition phenomena on ignition delay time data [25,26,28,34]. Since pre-ignition pressure rise can be associated entirely with volumetric kinetics (e.g., [38]), the use of high-speed imaging coupled with pressure data to characterize ignition behavior is vital to distinguish between volumetric low-temperature heat release and mixed, mild, or weak ignition. The presence of reaction fronts can dramatically accelerate ignition delay times as notably observed with syngas autoignition at low temperatures [26] or have limited to no effect on ignition delay times [29], depending on the ignition regime [25,26,27].

Many studies have documented the characteristics of the different ignition regimes, and these works have provided researchers with important data to advance theories on the state and mixture conditions leading to different ignition behavior (see Zeldovich [39], Sankaran *et al.* [40], Bansal and Im [30], Im *et al.* [41], and references therein). To briefly summarize the characteristics of the ignition regimes, strong ignition is when ignition chemistry dominates, and the entire test gas mixture ignites simultaneously and homogeneously, i.e., without spatial variation. Strong ignition is characterized by a rapid increase in pressure, and ignition delay times that are highly repeatable with low experimental uncertainties. Weak, mild, or mixed ignition occurs when reaction fronts propagate from one or more localized sites within the reaction chamber while the remainder of the unburned mixture is simultaneously undergoing autoignition. The pressure rise associated with the heat release from the reaction fronts compresses the unburned gases in the combustion chamber, typically accelerating the autoignition chemistry and leading to homogeneous ignition of the remaining unburned gases. Mansfield and Wooldridge [26] defined this behavior as "mixed" ignition due to the presence of both inhomogeneous characteristics (e.g., the presence of reaction fronts) and eventual homogeneous ignition of the unburned gas region. There have been many different means of defining strong ignition in the literature, including Meyer and Oppenheim [31] who classified strong ignition solely by whether a transition to detonation occurred. However, most of the recent studies have defined strong ignition as spatially uniform ignition behavior with the absence of localized reaction fronts prior to ignition.

Understanding the different types of ignition phenomena is critical to building confidence in the ignition delay time data used for developing and validating combustion chemistry. Most models used to test combustion reaction mechanisms represent ignition experiments of shock tubes and RCMs as zero-dimensional, i.e., they do not include spatial effects. The assumption of uniform state conditions is invalid for mixed ignition regimes and can lead to incorrect conclusions when comparing experimental and modeling data. Thus, theory that can predict *a priori* when mixed ignition can affect ignition delay time data is key to understanding experimental uncertainties and limitations. Additionally, it is valuable if the theory is accessible to a broad range of combustion reactivities without the need for extensive estimates, measurements, and simulations. The theory that is the focus of this chapter is the ignition criterion proposed by Sankaran et al. [40], which in turn was based on work by Zeldovich [39], that compares the laminar flame speed of a given mixture to the reaction front propagation rate driven by the thermal gradients present in the physical system. There are several ignition criteria that have been proposed in recent years, including works by Im *et al.* [41] and Grogan *et al.* [42]. The fairly simple inequality, referred to as the Sankaran Criterion, is a prediction strong ignition limit location based on comparison of the homogeneous chemical reactivity of a mixture with the deflagration flame speed of the mixture. The Sankaran Criterion is captured within the theory proposed by Im *et al.* [41] and Grogan *et al.* [42], but the latter theories including turbulent mixing scales. Turbulent mixing scales have not been measured in the UM-RCF and would therefore be a source of high uncertainties, hence they are not utilized in the present work. Additionally, the Sankaran criterion is considered more accessible to combustion engineers because it is based on more easily and more often measured input parameters of temperature and pressure.

The Sankaran Criterion can be used to make *a priori* predictions of ignition behavior, and the validity of the Sankaran Criterion as a predictive tool was demonstrated by Mansfield and Wooldridge [26] for syngas (CO and H_2) and by Mansfield *et al.* [25] for *iso*-octane. The theory was further developed and non-dimensionalized in the work by Im *et al.* [41]. Prior studies indicate the Sankaran Criterion is not fuel specific; however, additional demonstrations of the theory for other fuels, particularly for fundamental alkanes like propane, are important to building confidence in the validity of the theory. Additionally, mixed ignition is often associated with lower temperatures ($T < 1200$ K), where experimental measurements frequently exhibit higher scatter compared with higher temperatures (e.g., see **Figure 3.1**) and larger discrepancies with model predictions (e.g., syngas [26]). Thus, the objectives of this chapter were to test the Sankaran Criterion for application to propane ignition, providing further evidence of its utility as a general *a priori* method for accurately predicting ignition behavior, to evaluate the existing propane ignition data in the literature in the context of the Sankaran Criterion, and to consider simplified means to account for mixed ignition phenomena when comparing experimental data with model predictions. This work presents the first study of ignition regimes for a straight chain alkane, and successful demonstration of the approach for interpreting data in the literature has broad implications on low temperature ignition data of other fuels.

3.2 Methods

3.2.1 Experimental

As described in **Chapter 2**, the UM-RCF is a uniquely designed experimental apparatus that can create uniform state conditions at high temperatures (600 – 2000 K) and high pressures (1 – 40 atm) using a free piston (sabot) to isentropically compress a test gas mixture, with detailed descriptions of the apparatus available in Donovan *et al.* [43] and He *et al.* [44]. While these temperatures and pressures are achievable with the UM-RCF, limits are further imposed by the test times for propane ignition at the mixture compositions and state conditions studied. Test times greater than 75 ms can be affected by considerable heat losses that impact ignition, and test times less than 1 ms are convolved with the compression process. Thus, the current work targeted state and mixture conditions between the limits of test times from 1 to 75 ms.

The test gas mixtures are prepared in a stainless-steel mixing tank with an automatic stirring mechanism, and the mixture's composition determined through relative partial pressure measurements of each gas component. The mixture is typically left to stir overnight to ensure homogeneous mixture composition. The component gases used in this study were propane (PurityPlus, >99.5%), nitrogen (PurityPlus, >99.999%), argon (PurityPlus, >99.999%) and carbon dioxide (PurityPlus, >99.995%). Mixture uncertainty is predominantly a result of the uncertainty in the pressure transducers used to calculate mixture composition. Overall, uncertainty is < 0.1% for fuel concentration and < 0.05% for oxygen and diluent concentration.

Before each ignition experiment, a vacuum pump is used to evacuate the driven section, which is subsequently filled with the prepared test gas mixture. The driver section is then filled with compressed air that is used to propel the sabot down the length of the driven section upon opening the globe valve. The process rapidly compresses the test gas mixture into the test section located on the opposite end of the driven section, with the bulk of the compression occurring in the last 10 ms of the compression stroke. At the end of compression, the sabot seats via an annular interference fit which seals the test gas mixture within the test section at the desired thermodynamic conditions.

Pressure-time history measurements are obtained in the test section before, during, and after the compression process using a pressure transducer (Kistler 4045A2) and charge amplifier (Kistler 4618A0) with a 100 kHz sampling frequency. The pressure measurements have an uncertainty of ≤ 1% (~0.1 atm). A transparent polycarbonate end-wall is used for optical access for high-speed imaging of the autoignition process. Images for this study were recorded using a CMOS camera (Phantom V711-32G-MAG-C, 512 x 512 pixels) with a 50 mm lens (Navitar, F0.95), a 62mm lens (HOYA +2 Zoom), and a 62 mm UV(0) filter (Hoya). The video sequences were recorded at 25,000 frames per second with 39.6 μs exposure time.

For this study, the UM-RCF was used to conduct ignition experiments for mixtures of propane and oxygen with fuel-to-O_2 equivalence ratios of $\phi = 0.25$ and $\phi = 0.5$ with air levels of dilution; meaning the molar O_2-to-diluent gas ratio was 1:3.76. Three diluent gases (N_2, Ar, and CO_2) were used, with N_2 being the primary diluent gas, and the levels of Ar and CO_2 were adjusted to control the end-of-compression test gas temperature. Experiments with an equivalence ratio of $\phi = 0.25$ included end-of-compression temperatures between 930 – 1070 K and pressures between 8.9 – 10.4 atm, and experiments with an equivalence ratio of $\phi = 0.5$ included end-of-compression temperatures between 945 – 1010 K and pressures between 9.7 – 11.3 atm. As noted earlier, these conditions place the ignition delay times between 1 and 75 ms. Test times >75 ms are significantly affected by heat losses in RCMs, shock tubes and other devices, increasing measured ignition delay times beyond the effects of only chemical kinetics. Test times less than 1 ms are convolved with the compression process with many RCMs, and shock tubes and other experimental approaches may yield lower uncertainties. While a limited temperature range is covered in the study, importantly the data span predicted transitions in ignition behavior, allowing validation of the ignition regime hypothesis. The mixture composition and thermodynamic state conditions for each experiment are summarized in **Appendix B**.

3.2.2 Computational

Predictions for ignition delay times were made using the Healy *et al.* [45] C1 – C5 chemical kinetic mechanism with the Chemkin [46] program suite (version 19.1, x64) for a zero-dimensional, closed homogeneous reactor model with constant total volume and constant total energy. The original reaction mechanism by Healy *et al.* [45] was used with no changes to any of the rate coefficients. The predictions were obtained using the mixture composition and thermodynamic state (T and P) from each experiment as the initial conditions for the simulations. There are many different methods for quantifying uncertainties due to the reaction chemistry used with Chemkin simulations. Details on the uncertainty quantification for the simulations are provided in **Appendix B** along with results of time-dependent sensitivity analysis. The effects of different modeling assumptions were also evaluated, including simulating the compression stroke. Comparison of the modeling approaches is provided in **Appendix B**. Differences in the predicted ignition delay times due to different modeling approaches were less than the uncertainty associated with the elementary chemistry of the reaction mechanism. Therefore, constant volume and constant energy modeling was used throughout this work, and the error bars represented in figures are due to uncertainties in the rate coefficients used in the reaction mechanism. Note that quantifying uncertainties in reaction mechanisms remains non-standardized in the combustion community. Systematic methods for representing modeling uncertainties when reaction chemistry is significant (as in ignition modeling) remains an important area for future work.

The strong ignition limit was calculated using the Sankaran Criterion as described in Sankaran *et al.* [40] and as applied in Mansfield and Wooldridge [26] and Mansfield *et al.* [25]. As described by Sankaran *et al.* [40], the Criterion compares the relative magnitude of spontaneous propagation of ignition and deflagration, as per Equation (1):

$$\left|\frac{d\tau}{dT} * \frac{dT}{dx}\right| < (s_u^0)^{-1} \tag{1}$$

where the gradient of the ignition delay time (dτ/dx) is decomposed into the product of the thermal gradient of the physical system (dT/dx) and the thermal sensitivity of the ignition delay time (dτ/dT), and s_u^0 is the laminar flame speed. When spontaneous propagation dominates the ignition behavior of the combustion system and the thermal gradients are small, homogeneous, or strong, ignition is expected, and the inequality is true. When deflagration dominates, laminar flames consume the fuel inhomogeneously, faster than the autoignition chemistry, and the inequality is false meaning weak ignition is expected. Between the limiting strong and weak ignition regimes, mixed ignition is expected with some attributes of autoignition and propagation of local reaction fronts.

To evaluate Eqn. (1), ignition delay times were systematically calculated over a broad range of thermodynamic conditions for $\phi = 0.25$ and $\phi = 0.5$. The results were used to calculate the thermal sensitivity of the ignition delay time, dτ/dT for each equivalence ratio. A constant thermal gradient of 5 K/mm value was applied in Mansfield and Wooldridge [26] and Mansfield *et al.* [25]

for syngas and *iso*-octane, respectively. The value of 5 K/mm originates from temperature measurements made in the UM-RCF by Donovan *et al.* [43]. Laminar flame speeds were calculated using the Premixed Laminar Flame-Speed Calculation in Chemkin [46] with the Healy *et al.* [45] reaction mechanism, thermodynamic data, and transport data. Laminar flame speeds for temperatures above ~1000 K and below ~750 K were extrapolated from calculations at intermediate temperatures using an exponential fit.

3.3 Results and discussion

Pressure-time histories and high-speed video were recorded for each experiment. The pressure data were used to determine the ignition delay time for each experiment, and the high-speed videos were used to observe and classify the ignition behavior based on the chemiluminescence observed. Typical pressure histories for inhomogeneous (mixed) and homogeneous (strong) ignition are presented in **Figure 3.2** and **Figure 3.3**, respectively. For both experiments, the pressure data show the compression stroke causes a smooth increase in pressure in the test section until the end of compression. After the end of compression, there is a slight pressure decrease in both experiments caused by heat transfer from the test gas to the cooler test-section walls. P_{min} is the minimum pressure after the end of compression and is labeled in the figures. The key difference in the two pressure histories is near the time of ignition. The pressure history for the mixed (inhomogeneous) ignition experiment in **Figure 3.2** shows a gradual pressure rise starting around P_{min} (from t = ~5 to 12 ms), prior to the rapid increase in pressure due to ignition at t = 13.1 ms. This pre-ignition heat release is most apparent in the pressure derivative data, also presented in **Figure 3.2**. The pressure history for the strong (homogeneous) ignition experiment in **Figure 3.3** shows no heat release prior to ignition at 15.6 ms.

Figure 3.4 presents imaging results corresponding to the experimental data presented in **Figure 3.2** and **Figure 3.3**. The images in the left column of **Figure 3.4** exhibit inhomogeneous characteristics and are from the same experiment as the pressure data presented in **Figure 3.2**. The images in the right column of **Figure 3.4** exhibit uniform or homogenous ignition characteristics and are from the same experiment as the pressure data presented in **Figure 3.3**. The three still images from each experiment are from after the end of compression and correspond to times at: 1. P_{min}, 2. an intermediate time, and 3. the time of ignition. Comparison of the pressure and imaging data from the inhomogeneous experiment (i.e., **Figure 3.2** and the left column of **Figure 3.4**) shows the gradual pressure rise before ignition corresponds with the propagation of reaction fronts in the test section (t = 4 to ~13 ms), and the rapid pressure rise at 13.1 ms corresponds with autoignition of the reactants not consumed by the reaction fronts. The timing of the first observation of the reaction fronts (t =~4 ms) is consistent with the timing of the first observation of an increase in the rate of pressure rise after the end of mechanical compression of the test gas mixture (t=~5 ms). Alternatively, comparison of the pressure and imaging data from the homogeneous experiment (i.e., **Figure 3.3** and the right column of **Figure 3.4**) shows no early heat release or reaction fronts prior to ignition, and the chemiluminescence at ignition is spatially uniform. Furthermore, the maximum intensity of the images corresponds exactly with the maximum rate of pressure rise at t = 15.6 ms. Comparing the imaging data at the time of ignition from the mixed and strong ignition experiments highlights the non-uniformity of the chemiluminescence caused by the reaction fronts at the mixed ignition conditions.

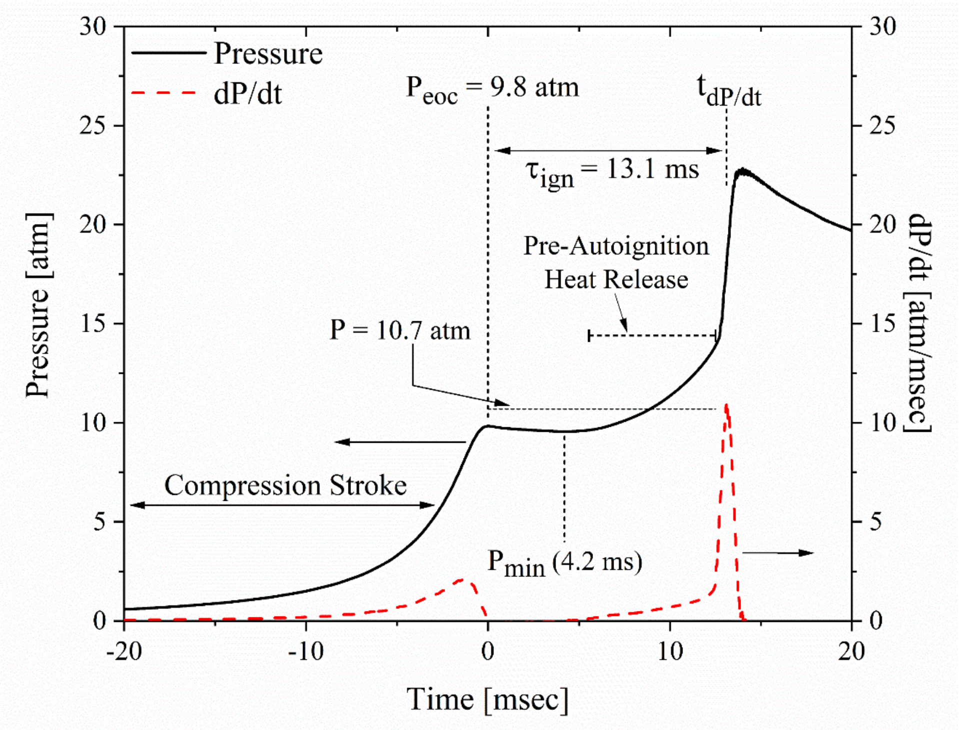

Figure 3.2: Typical experimental pressure history exhibiting characteristics of mixed ignition for conditions of P = 10.7 atm, T = 963 K, and ϕ=0.5 with a mixture composition of 2.06% C_3H_8/20.60% O_2/77.34% N_2. P_{eoc} is the pressure at the end of the mechanical compression stroke, and P is the time-averaged pressure from P_{eoc} to P at maximum dP/dt.

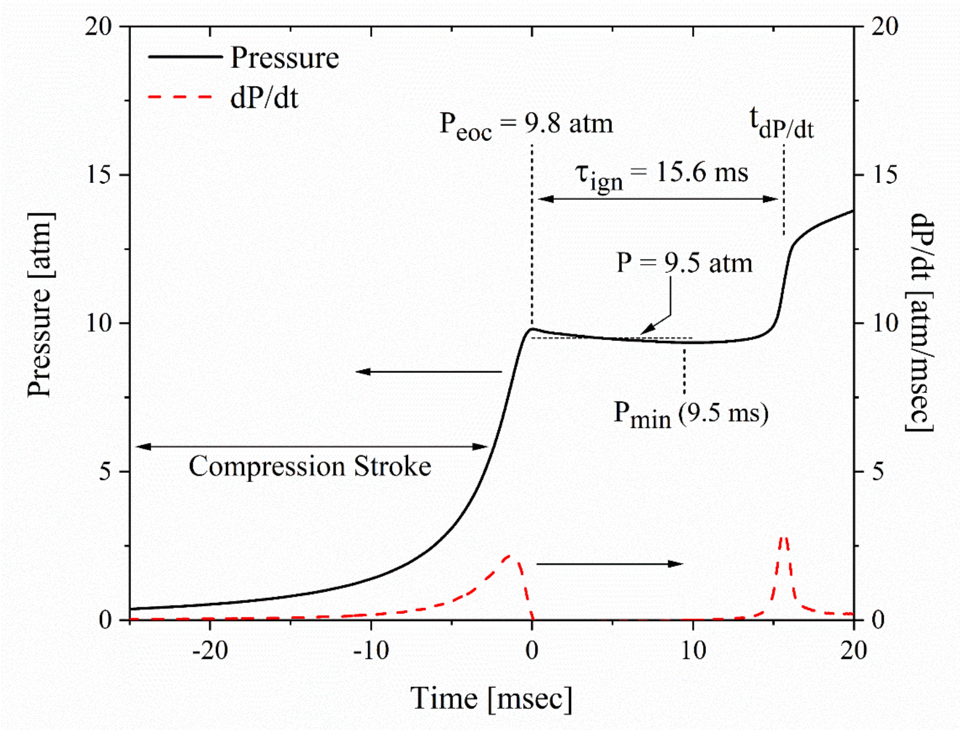

Figure 3.3: Typical experimental pressure history exhibiting characteristics of strong ignition for experimental conditions of P = 9.5 atm, T = 990 K, and ϕ = 0.25 with a mixture composition of 1.04% C_3H_8/20.80% O_2/78.16% N_2. P_{eoc} is the end of the mechanical compression stroke, and P is the time averaged pressure from P_{eoc} to P at maximum dP/dt.

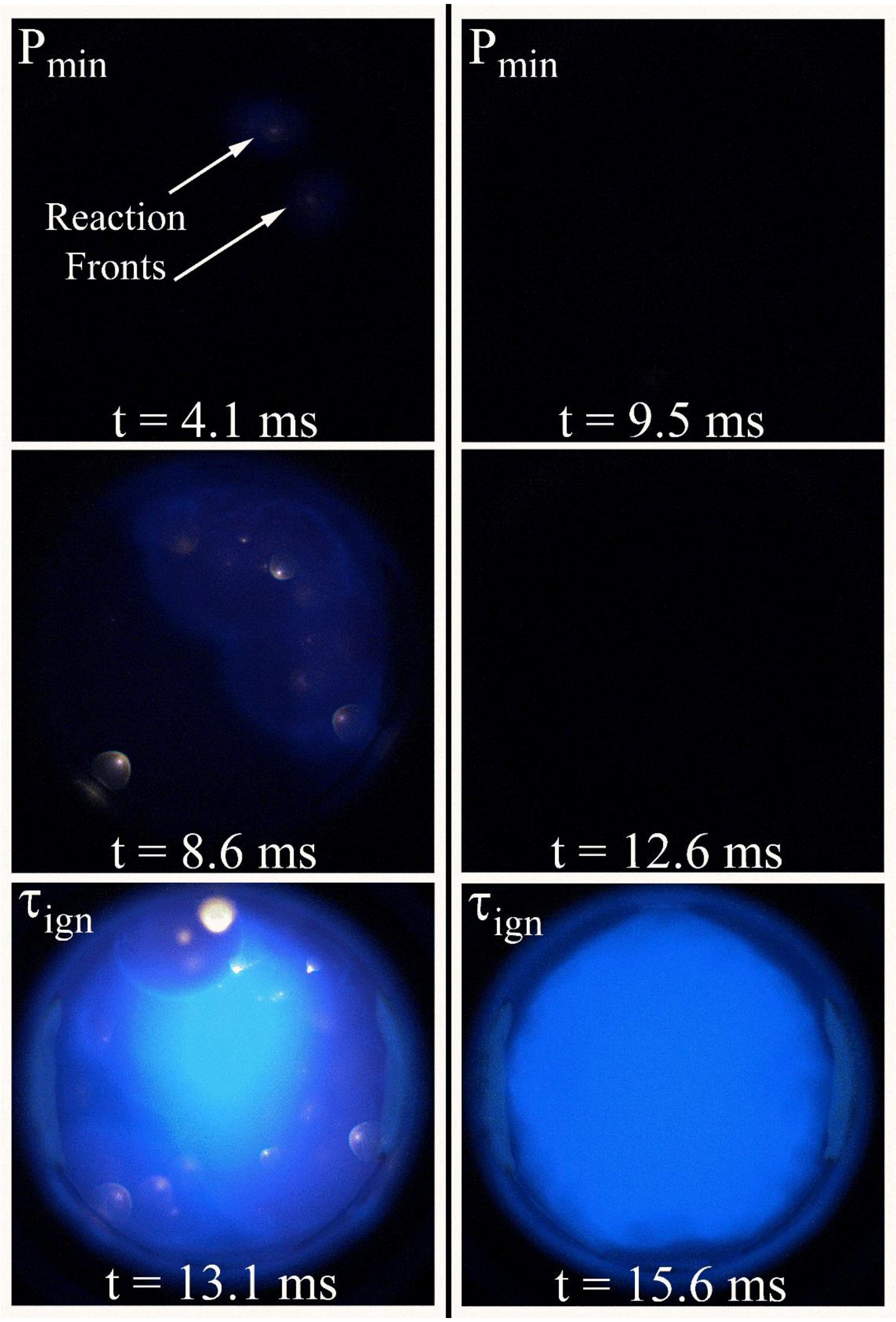

Figure 3.4: Imaging results from typical inhomogeneous (left column) and homogeneous (right column) ignition experiments. The images in the left column are from the same experiment as the data presented in **Figure 3.2**. The images in the right column are from the same experiment as the data presented in **Figure 3.3**. Note the presence and propagation of reaction fronts at the inhomogeneous ignition conditions.

The pressure data were used to determine the ignition delay time and thermodynamic state conditions for each experiment. First the pressure data were filtered using a 75-point smoothing algorithm to reduce noise from the pressure transducer, and the pressure derivative was calculated.

The ignition delay time (τ) was defined as the time from the end-of-compression (i.e., the time of maximum pressure due to compression of the test gas mixture by the sabot) to the time of maximum dP/dt, as shown in **Figure 3.2** and **Figure 3.3**. The primary uncertainty in the ignition delay time is due to the noise in the pressure data, resulting in a maximum uncertainty of ± 0.6 ms.

The pressure for each experiment was defined as the time-averaged value of pressure from the end-of-compression to the time of maximum dP/dt. The temperature was then defined using isentropic state relations and the actual mixture properties, as described in Donovan *et al.* [43]. The primary uncertainty in the pressure is due to noise in the transducer data and is assessed as <0.4 atm based on different smoothing algorithms. The uncertainty in temperature is primarily due to propagation of the uncertainty of the pressure measurements, and is estimated as <10 K. A summary of the state conditions and measured ignition delay times is provided in **Appendix B**. Alternative methods for assigning state conditions are discussed further below.

3.3.1 Autoignition behavior

All experiments were categorized using the imaging data as either mixed ignition (where reaction fronts were observed prior to volumetric autoignition) or strong ignition (where no reaction fronts were observed prior to volumetric autoignition). No experiments exhibited characteristics of weak ignition (where only reaction fronts consume the reactants with no volumetric autoignition). The results for the classifications of the experiments are presented on pressure-temperature diagrams for $\phi = 0.25$ in **Figure 3.5** and for $\phi = 0.5$ in **Figure 3.6**, and the figures include ignition delay time contours and the strong ignition limits based on the Sankaran Criterion/Eqn. (1). Recall, the ignition delay time contours and the parameters used to define the strong ignition limit were calculated using Chemkin modeling and the Healy *et al.* [45] reaction mechanism. No other propane ignition studies that include imaging data for regime classification are available in the literature. However, the range of conditions considered in previous ignition studies of propane for $\phi = 0.5$ is highlighted in **Figure 3.6**.

The experimental results for $\phi = 0.25$ resulted in ignition delay times from 4 ms to 56 ms in the temperature range of 930 – 1070 K and the pressure range of 8.9 – 10.4 atm. The high-speed imaging data indicated spatially uniform ignition behavior with no flame front propagation prior to ignition (i.e., strong ignition) for all $\phi = 0.25$ experiments. As seen in **Figure 3.5**, the results are in excellent agreement with expectations based on the Sankaran Criterion for the strong ignition limit.

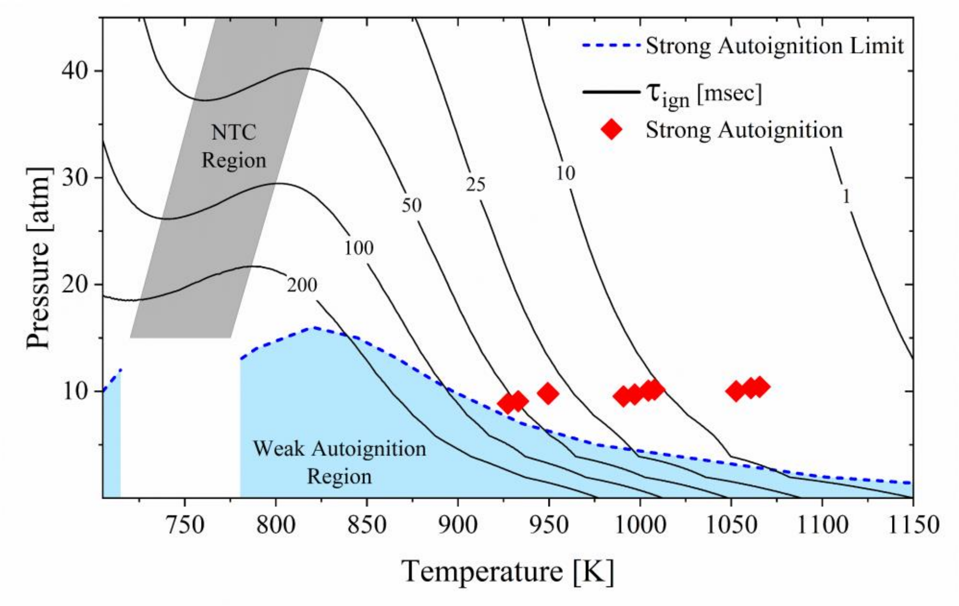

Figure 3.5: Experimental results for ignition regimes for ϕ = 0.25 as a function of state conditions. Calculated ignition delay time contours, τ_{ign} [ms], are shown as solid lines. The unshaded region is the strong ignition regime based on the Sankaran Criterion for the strong ignition limit assuming a 5 K/mm thermal gradient. The blue shaded region is the weak ignition regime.

Figure 3.6 presents the ignition regime classification results for mixtures with ϕ = 0.5. The ignition delay times varied from 6 ms to 22 ms in the temperature range of 945 – 1000 K and the pressure range of 9.7 – 11.3 atm. The high-speed imaging data confirmed the presence of reaction fronts (with pre-ignition heat release) prior to volumetric autoignition for all the ϕ = 0.5 experiments. The results are generally consistent with expectations based on the Sankaran Criterion, with most of the mixed autoignition experiments falling within the weak ignition regime. While some of the experimental conditions at higher temperatures might have been expected to yield strong ignition, the strong ignition limit plotted in **Figure 3.6** does not include uncertainty bounds, which might reasonably extend the strong ignition limit to include the experimental data. Also superimposed on the ignition regime diagram in **Figure 3.6** is the approximate range of state conditions of the low-temperature studies presented in the Arrhenius diagram in **Figure 3.1**. The superposition highlights that many of the data from the experimental studies of propane at low temperature may be affected by mixed ignition characteristics.

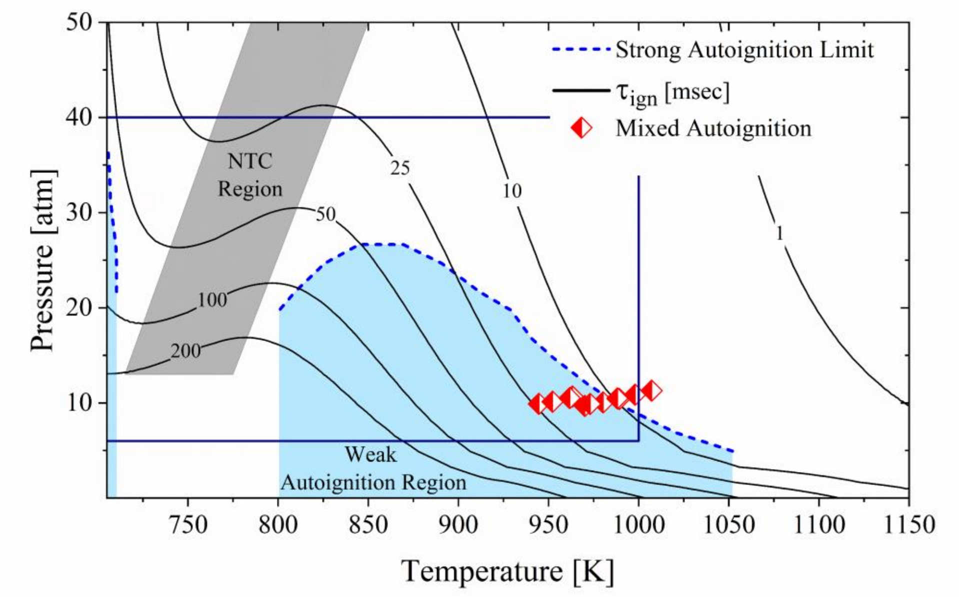

Figure 3.6: Experimental results for ignition regimes for ϕ = 0.5 as a function of state conditions. Calculated ignition delay time contours, τ_{ign} [ms], are shown as solid lines. The unshaded region is the strong ignition regime based on the Sankaran Criterion for the strong ignition limit assuming a 5 K/mm thermal gradient. The blue shaded region is the weak ignition regime. The box indicates the approximate bounds of the experimental conditions of the low-temperature studies presented in **Figure 3.1**.

3.3.2 Autoignition delay time

Figure 3.7 and **Figure 3.8** summarize the ignition delay time results as a function of inverse temperature for the two equivalence ratios studied. The error bars represent the uncertainties in the measurements described previously and the uncertainties in the model predictions described in **Appendix B**. In **Figure 3.7** and **Figure 3.8**, the two panels show the comparison between the experimental measurements and the model predictions where two different methods are used to define the thermodynamic state conditions of the experiments. Recall, the state conditions of the experiments are also the initial conditions used in the 0-dimensional Chemkin modeling, with the volume and total energy of the system fixed during the simulation allowing the pressure and temperature to change as the simulated reactions progress. Note that, while localized ignition and propagation of the reaction fronts affect the unburned gases by increasing pressure (and therefore temperature), the 0D homogeneous reactor is still an appropriate first order representation of the system, since mass transport does not occur on a time scale to impact the unburned gases. In **Figure 3.7(a)** and **Figure 3.8(a)**, the temperature and pressure are based on the time-averaged pressure from the end of compression to the time of maximum pressure rise. As seen in the pressure history data in **Figure 3.2**, this definition includes the effects of pre-ignition heat release and compression heating of the unburned gases by reaction front propagation. In **Figure 3.7(b)** and **Figure 3.8(b)**, the temperature and pressure are based on the time-averaged pressure from the end-of-compression to the time of minimum pressure before autoignition, P_{min}. This definition neglects pre-ignition heat release. For strong ignition conditions, where negligible pre-ignition heat release was observed, the difference in definitions should have little effect on the experimental and model results, which is consistent with the results shown in **Figure 3.7**. Additionally, the model predictions using the Healy *et al.* mechanism [45] at the strong $\phi = 0.25$ conditions are in excellent agreement with the experimental measurements.

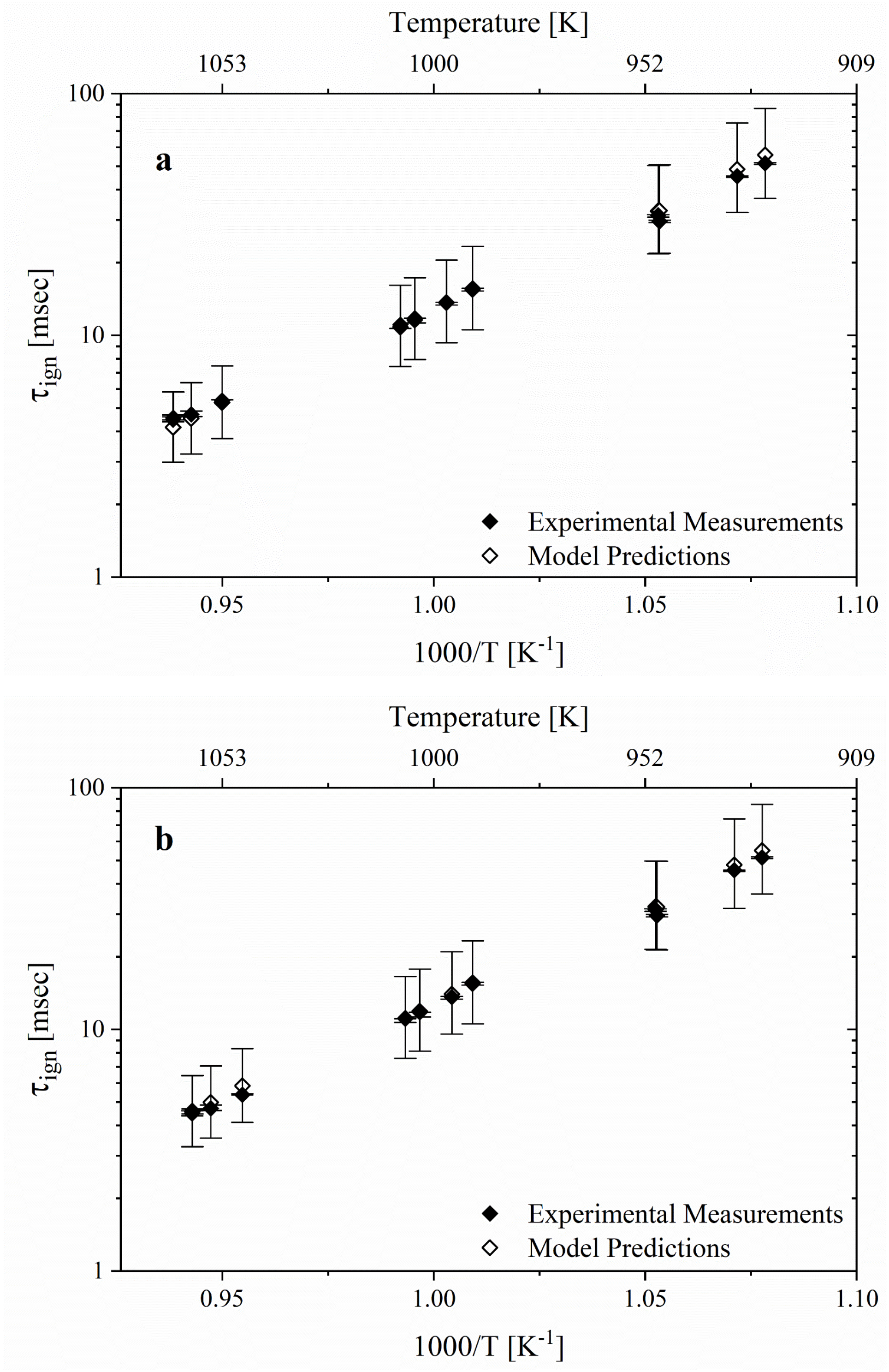

Figure 3.7: Measured and predicted ignition delay times for $\phi = 0.25$ where strong ignition was observed for all experiments: (a) state conditions based on the time-averaged pressure from the end-of-compression to maximum dP/dt, (b) state conditions based on the time-averaged pressure from the end-of-compression to P_{min} prior to autoignition. For both panels, the error bars represent the uncertainties of the experimental measurements and model predictions.

On the other hand, **Figure 3.8** shows the impact of mixed ignition and the associated pre-ignition heat release on the assigned state conditions and on the comparison between physical measurements and model predictions. As seen in **Figure 3.8(a)**, when the effects of early heat release are included in defining the state conditions, the model predictions and experimental data generally agree within the uncertainty limits. However, when pre-ignition heat release is neglected, as in **Figure 3.8(b)**, the model predictions are systematically higher than the experimental measurements, and the effects are larger at lower temperatures with a maximum discrepancy of a factor of three observed between the experimental results and model predictions. The trend for agreement between model predictions and experimental measurements follows closely with the proximity to the strong ignition regime (see **Figure 3.6**).

Comparison of the experimental data in the two panels in **Figure 3.8** also shows reaction fronts can lead to observable effects on the Arrhenius diagram due to differences in the assigned state conditions. Specifically, while the temperature and pressure for an experiment does not impact the measurement of the ignition delay time from the pressure history data, changing the assigned temperature shifts the data along the x-axis. Additionally, if the ignition delay time data are scaled based on pressure (as in **Figure 3.1**), changing the assigned pressure shifts the data on the vertical axis of the Arrhenius diagram as well. Depending on the amount of pre-ignition heat release, using time-averaged state conditions that do or do not include the effects of pre-ignition heat release can significantly rearrange the data, as most dramatically illustrated by comparing the four lowest temperature data in **Figure 3.8(a)** and **Figure 3.8(b)**. In this work, maximum differences in pressure of 1.0 atm and in temperature of 23 K were determined when the two methods were applied to mixed ignition experiments, compared with maximum differences of 0.2 atm and 5 K with strong ignition experiments. Note, some studies use volume histories of compression of an inert gas mixture to model RCM experiments. Such an approach would not capture the effects of reaction fronts and the associated heat release and would be expected to yield systematically higher ignition delay times.

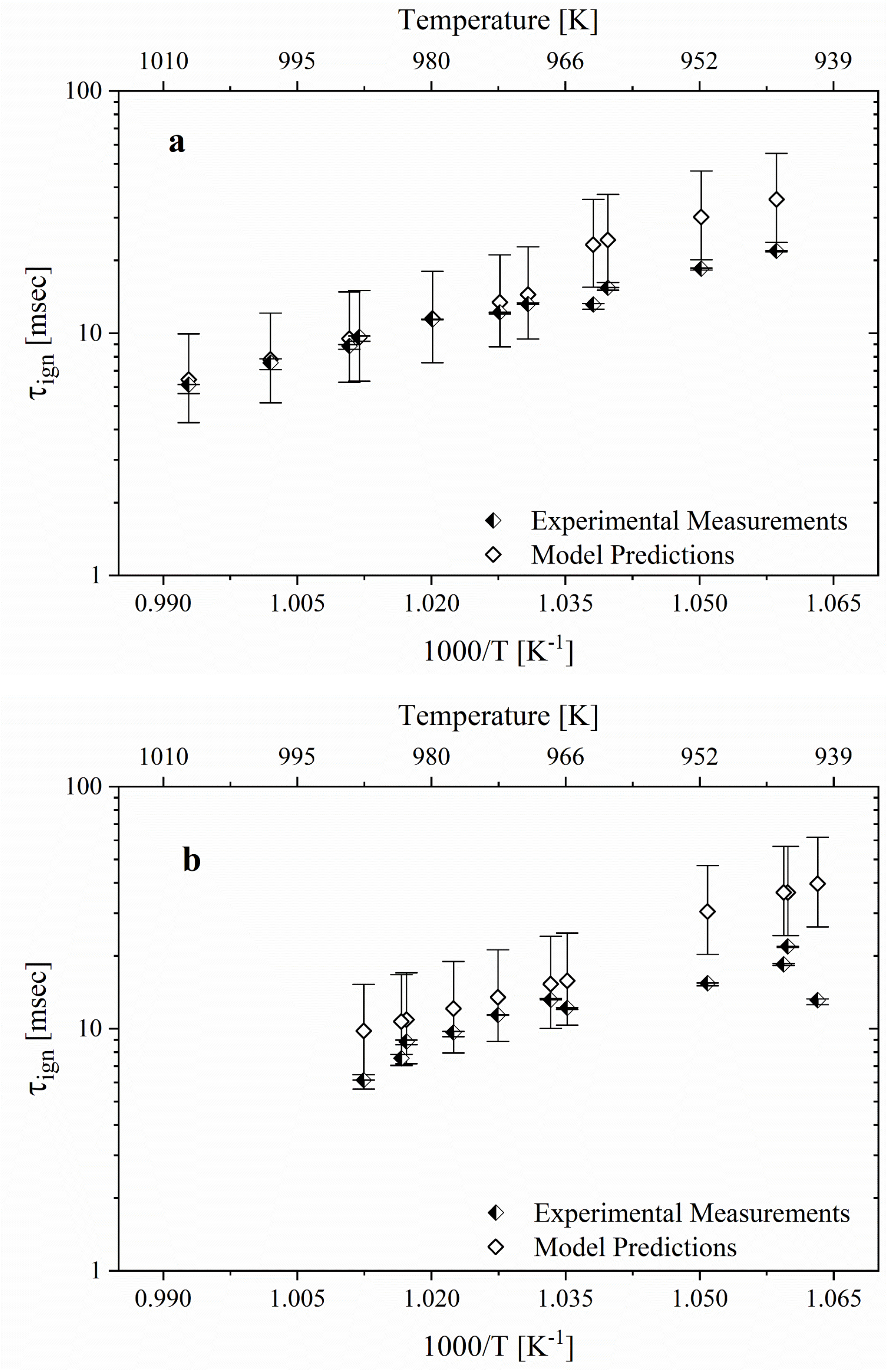

Figure 3.8: Measured and predicted ignition delay times for $\phi = 0.5$ where mixed ignition was observed for all experiments: (a) state conditions based on the time-averaged pressure from the end-of-compression to maximum dP/dt, (b) state conditions based on the time-averaged pressure from the end-of-compression to P_{min} prior to ignition. For both panels, the error bars represent the uncertainties of the experimental measurements and model predictions.

The experimental ignition delay time results from the current work are compared with previous ignition studies of propane at an equivalence ratio of $\phi = 0.5$ in **Figure 3.9**, where all data have been normalized to P = 10 atm using scaling of $\tau_{ign} \propto 1/P$ and normalized to air dilution levels using scaling of $\tau_{ign} \propto$ concentration of diluent. In **Figure 3.9**, the state conditions that include the effects of pre-autoignition heat release were used for the UM-RCF data. Also in the figure, the mixture and state conditions reported in the prior studies were used with the Sankaran Criterion (**Figure 3.6**) to categorize the prior experiments as in the weak or strong ignition regimes. The results are within the range of values reported previously for τ_{ign} at similar conditions; however, comparison of the state conditions used in prior studies with the ignition diagram of **Figure 3.6** indicates some of the previous studies were likely in the weak ignition regime and may have been affected by reaction fronts. Notably, in the temperature region covered here, the scatter in the ignition delay time data is at least an order of magnitude. The scatter could be due (in part) to the propagation of localized reaction fronts, and the use of time-integrated pressure data (or other means to account for pre-ignition heat release) to assign state conditions could possibly correct for some of the scatter (as in **Figure 3.8**). However, the pressure histories of the prior studies are not available for the majority of the data reported in the literature. Model predictions for P = 10 atm are also shown in **Figure 3.9** and are in excellent agreement with the current results and other studies at strong ignition conditions. Notably, experimental data farthest from the model predictions are in the weak ignition regime based. Also note for P = 10 atm, NTC behavior is predicted for temperatures below 800 K and will likely contribute further to the scatter at temperatures below 800 K.

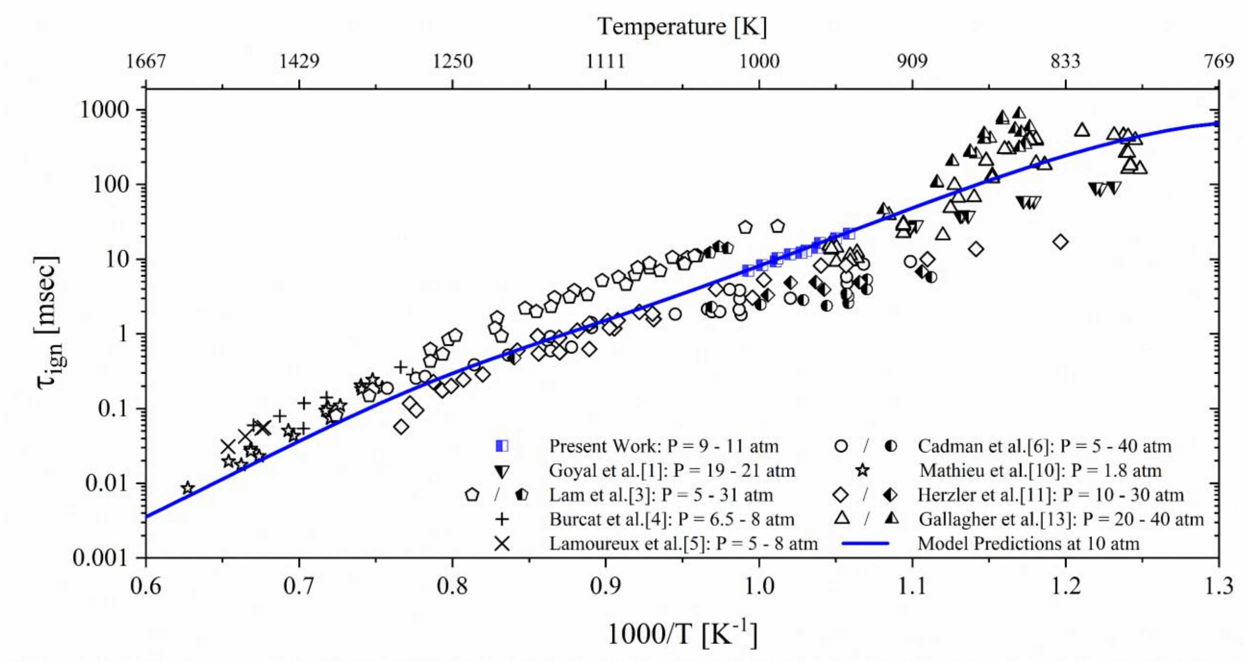

Figure 3.9: Comparison of ignition delay time measurements for propane/air mixtures at ϕ=0.5. All data have been normalized to P = 10 atm and air dilute conditions. Based on the reported state conditions and using the Sankaran Criterion presented in **Figure 3.6**, half-filled symbols are in the weak ignition region and unfilled symbols are in the strong ignition region.

Figure 3.10 presents a comparison of the current results with prior studies of propane mixtures at ϕ = 0.25. As with **Figure 3.9**, the data have been scaled to P = 10 atm and air levels of dilution. There are no previous studies at low temperatures for propane at ϕ = 0.25, only the current RCF study. All data presented in **Figure 3.10** are in the strong ignition region, and model predictions included in **Figure 3.10** show excellent agreement with both experimental studies.

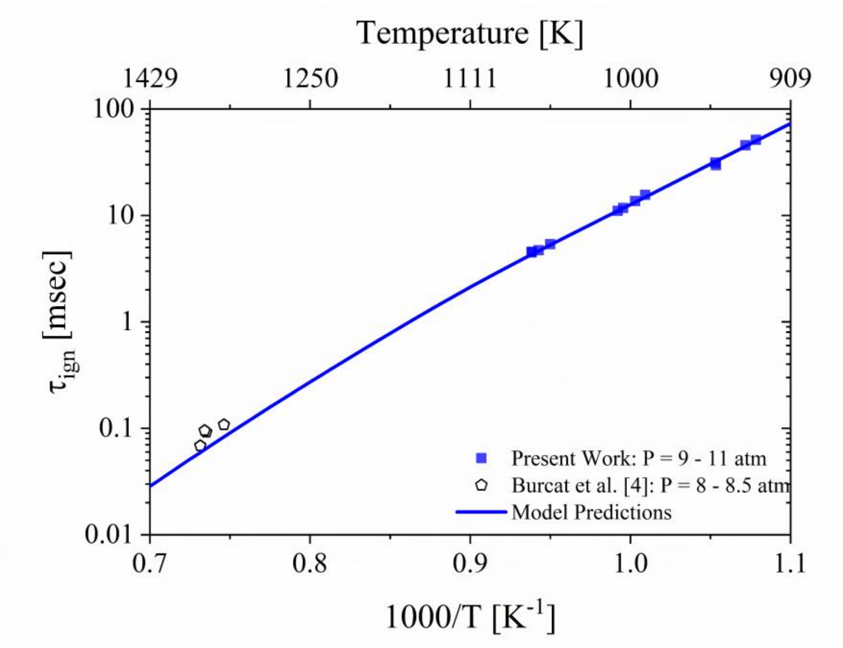

Figure 3.10: Comparison of ignition delay time measurements for propane/air mixtures at ϕ=0.25. All data have been normalized to P = 10 atm and air dilute conditions. Based on the reported state conditions and using the Sankaran Criterion presented in **Figure 3.6**, the filled and unfilled symbols are in the strong ignition region.

3.4 Conclusions

This chapter presents the first experimental results to categorize the ignition behavior of propane mixtures using pressure and imaging data simultaneously acquired at low-temperature conditions. Ignition behavior for lean propane-air mixtures exhibited exclusively strong (spatially homogeneous) ignition characteristics at the state conditions studied with mixtures of ϕ = 0.25 and exclusively mixed (spatially inhomogeneous with propagation of localized reaction fronts) ignition characteristics at the state conditions studied with mixtures of ϕ = 0.5. The results supported the validity of the Sankaran Criterion to identify the strong ignition limit for propane, where the limit shifted to higher temperatures and pressures as the equivalence ratio was increased. High-speed imaging showed the presence of reaction fronts were associated with pre-ignition heat release for all inhomogeneous ignition experiments, and homogeneous ignition did not exhibit heat release prior to ignition. Model predictions were in excellent agreement with ignition delay times measured in the current work when time-averaged values including the effects of pre-ignition heat release were used. Model predictions over-estimated ignition delay times determined from mixed ignition experiments, if the effects of pre-ignition heat release were not considered, especially at lower temperatures.

The results of this study quantified the impact of mixed ignition phenomena on propane ignition data at low temperatures, and the importance of assigning state conditions that appropriately capture ignition behavior within the reactor. The effects of state conditions are particularly important when ignition data are used to inform and validate chemical kinetic models. The results identified mixed ignition phenomena as a potential source of the higher scatter observed in the low temperature ignition data for propane.

The results presented in this chapter provide further evidence that the Sankaran Criterion is both a powerful means to improve the quality and understanding of low temperature ignition data and a useful method for *a priori* predictions of ignition behavior. This outcome has potentially far-reaching implications and impact. The Sankaran Criterion should be applied pro-actively to plan ignition delay time experiments that isolate strong ignition conditions, which are then ideally suited for chemical kinetics studies. Alternatively, the Sankaran Criterion can be retroactively applied to interpret ignition delay time data and pressure histories, particularly when imaging data are not available. In particular, the Sankaran Criterion can be used to revise experimental uncertainties on ignition data that are used for development of reaction chemistry, potentially resolving discrepancies observed in experimental and computational studies at these important low temperature conditions.

3.5 References

[1] T. Goyal, D. Trivedi, O. Samimi Abianeh, Autoignition and flame spectroscopy of propane mixture in a rapid compression machine, Fuel 233 (2018) 56-67.

[2] O. Samimi-Abianeh, J.A. Piehl, A. Zyada, M. Al-Sadoon, L. Brave, Effect of Diluents on the Autoignition of Propane Mixtures Using a Rapid Compression Machine, Energy and Fuels 33 (4) (2019) 3529-3538.

[3] K.-Y. Lam, Z. Hong, D.F. Davidson, R.K. Hanson, Shock tube ignition delay time measurements in propane/O2/argon mixtures at near-constant-volume conditions, Proc. Combust. Inst. 33 (1) (2011) 251-258.

[4] A. Burcat, A. Lifshitz, K. Scheller, G. Skinner, Shock-tube investigation of ignition in propane-oxygen-argon mixtures, Symp. (Int.) Combust.13, (1971) 745-755.

[5] N. Lamoureux, C. Paillard, V. Vaslier, Low hydrocarbon mixtures ignition delay times investigated behind reflected shock waves, Shock Wave 11 (2002) 309-322.

[6] P. Cadman, G. Thomas, P. Butler, The auto-ignition of propane at intermediate temperatures and high pressures, Phys. Chem. Chem. Phys. 2 (2000) 5411-5419.

[7] C.J. Brown, G.O. Thomas, Experimental studies of shock-induced ignition and transition to detonation in ethylene and propane mixtures, Combust. Flame 117 (1999) 861-870.

[8] K. Kim, K. Shin, Shock Tube and Modeling Study of the Ignition of Propane, Bull. Korean Chem. Soc. 22 (2001) 303-307.

[9] D. Healy, H.J. Curran, S. Dooley, J.M. Simmie, D.M. Kalitan, E.L. Petersen, G. Bourque, Methane/propane mixture oxidation at high pressures and at high, intermediate and low temperatures, Combust. Flame 155 (3) (2008) 451-461.

[10] O. Mathieu, J. Goulier, F. Gourmel, M.S. Mannan, N. Chaumeix, E.L. Petersen, Experimental study of the effect of CF3I addition on the ignition delay time and laminar flame speed of methane, ethylene, and propane, Proc. Combust. Inst. 33 (3) (2015) 2731-2739.

[11] J. Herzler, L. Jerig, P. Roth, Shock-tube study of the ignition of propane at intermediate temperatures and high pressures, Combust. Sci. Tech. 176 (10) (2004) 1627-1637.

[12] P. Dagaut, M. Cathonnet, J.C. Boettner, Kinetic modeling of propane oxidation and pyrolysis, Int. J. Chem. Kinet. 24 (1992) 813-837.

[13] S.M. Gallagher, H.J. Curran, W.K. Metcalfe, D. Healy, J.M. Simmie, G. Bourque, A rapid compression machine study of the oxidation of propane in the negative temperature coefficient regime, Combust. Flame 153 (1/2) (2008) 316-333.

[14] A. Ramalingam, Y. Fenard, A. Heufer, Ignition delay time and species measurement in a rapid compression machine: A case study on high-pressure oxidation of propane, Combust. Flame 211 (2020) 392-405.

[15] M. Cathonnet, J.C. Boettner, H. James, Experimental study and numberical modeling of high temperature oxidation of propane and n-butane, Symp. (Int.) Combust. 18 (1981) 903-913.

[16] D.J. Beerer, V.G. McDonell, An experimental and kinetic study of alkane autoignition at high pressures and intermediate temperatures, Proc. Combust. Inst. 33 (2011) 301-307.

[17] J.S. Hoffman, W. Lee, T.A. Litzinger, D.A. Santavicca, W.J. Pitz, Oxidation of propane at elevated pressures: experiments and modeling, Combust. Sci. Technol. 77 (1991) 95-125.

[18] P. Sabia, M. de Joannon, M.L. Lavadera, P. Giudicianni, R. Ragucci, Autoignition delay times of propane mixtures under MILD conditions at atmospheric pressure, Combust. Flame 161 (2014) 3022-3030.

[19] P. Dagaut, M. Cathonnet, J.C. Boettner, F. Gaillard, Kinetic modeling of propane oxidation, Combust. Sci. Technol. 56 (1987) 23-63.

[20] S.S. Merchant, C.F. Goldsmith, A.G. Vandeputte, M.P. Burke, S.J. Klippenstein, W.H. Green, Understanding low-temperature first-stage ignition delay: Propane, Combust. Flame 161 (10) (2015) 3658-3673.

[21] S.S. Goldsborough, S. Hochgreb, G. Vanhove, M.S. Wooldridge, H.J. Curran, C.-J. Sung, Advances in rapid compression machine studies of low- and intermediate autoignition phenomena, Prog. Energy Combust. Sci. 63 (2017) 1-78.

[22] G.A. Richards, M.M. McMillian, R.S. Gemmen, W.A. Rogers, S.R. Cully, Issues for low-emission, fuel-flexible power systems, Prog. Energy Combust. Sci. 27 (2) (2001) 141-169.

[23] S. Saxena, I.D. Bedoya, Fundamental phenomena affecting low temperature combustion and HCCI engines, high load limits and strategies for extending these limits, Prog. Energy Combust. Sci. 39 (2013) 457-488.

[24] X. Lu, D. Han, Z. Huang, Fuel design and management for the control of advanced compression-ignition combustion modes, Prog. Energy Combust. Sci. 37 (2011) 741-783.

[25] A.B. Mansfield, M.S. Wooldridge, H. Di, X. He, Low-temperature ignition behavior of *iso*-octane, Fuel 139 (2015) 79-86.

[26] A.B. Mansfield, M.S. Wooldridge, High-pressure low-temperature ignition behavior of syngas mixtures, Combust. Flame 161 (9) (2014) 2242-2251.

[27] P. Pal, A. B. Mansfield, P.G. Arias, M.S. Wooldridge, H.G. Im, A computational study of syngas auto-ignition characteristics at high-pressure and low-temperature conditions with thermal inhomogeneities, Combust. Theory Model. 19 (5) (2015) 587-601.

[28] S.M. Walton, X. He, B.T. Zigler, M.S. Wooldridge, A. Atreya, An experimental investigation of *iso*-octane ignition phenomena, Combust. Flame 150 (3) (2007) 246-262.

[29] D. Assanis, S.W. Wagnon, M.S. Wooldridge, An experimental study of flame and autoignition interactions of *iso*-octane and air mixtures, Combust. Flame 162 (4) (2015) 1214-1224.

[30] G. Bansal, H.G. Im, Autoignition and front propagation in low temperature combustion engine environments, Combust. Flame 158 (11) (2011) 2105-2112.

[31] J.W. Meyer, A.K. Oppenheim, On the shock-induced ignition of explosive gases, Symp. (Int.) Combust. 13 (1) (1971) 1153-1164.

[32] R. Blumenthal, K. Fieweger, K.H. Kom, G. Adomeit, Gas Dynamic Features of Self Ignition of Non-Diluted Fuel/Air Mixtures at High Pressure, Combust. Sci. Tech. 113 (1) (1996) 137-166.

[33] K. Fieweger, R. Blumenthal, G. Adomeit, Shock-tube investigations on the self-ignition of hydrocarbon-air mixtures at high pressures, Symp. (Int.) Combust. 25 (1) (1994) 1579-1585.

[34] D.J. Vermeer, J.W. Meyer, A.K. Oppenheim, Auto-ignition of hydrocarbons behind reflected shock waves, Combust. Flame 18 (3) (1972) 327-336.

[35] K. Fieweger, R. Blumenthal, G. Adomeit, Self-ignition of S.I. engine model fuels: A shock tube investigation at high pressure, Combust. Flame 109 (4) (1997) 599-619.

[36] J. Shao, R. Choudhary, A.J. Susa, Y. Peng, D.F. Davidson, R.K. Hanson, High-speed imaging of n-heptane ignition in a high-pressure shock tube, Proc. Combust. Inst. (2020), https://doi.org/10.1016/j.proci.2020.06.158.

[37] V.A. Troutman, C.L. Strand, M.F. Cambell, A.M. Tulgestke, V.A. Miller, D.F. Davidson, R.K. Hanson, High-speed OH* chemiluminescence imaging of ignition through a shock tube end-wall, Appl. Phys. B. 122 (56) (2016) 1-7.

[38] D.M.A. Karwat, S.W. Wagnon, M.S. Wooldridge, C.K. Westbrook, Low-temperature speciation and chemical kinetic studies of n-heptane, Combust. Flame 160 (12) (2013) 2693-2706.

[39] Ya.B. Zeldovich, Regime classification of an exothermic reaction with nonuniform initial conditions, Combust. Flame 39 (2) (1980) 211-214.

[40] R. Sankaran, H.G. Im, E.R. Hawkes, J.H. Chen, The effects of non-uniform temperature distribution on the ignition of a lean homogeneous hydrogen–air mixture, Proc. Combust. Inst. 30 (1) (2005) 875-882.

[41] H.G. Im, P. Pal, M.S. Wooldridge, A.B. Mansfield, A regime diagram for autoignition of homogeneous reactant mixtures with turbulent velocity and temperature fluctuations, Combust. Sci. Tech. 187 (2015) 1263-1275.

[42] K.P. Grogan, S.S. Goldsborough, M. Ihme, Ignition regimes in rapid compression machines, Combust. Flame 162 (8) (2015) 3071-3080.

[43] M.T. Donovan, X. He, B.T. Zigler, T.R. Palmer, M.S. Wooldridge, A. Atreya, Demonstration of a free-piston rapid compression facility for the study of high temperature combustion phenomena, Combust. Flame 137 (3) (2004) 351-365.

[44] X. He, B.T. Zigler, S.M. Walton, M.S. Wooldridge, A. Atreya, A rapid compression facility study of OH time histories during *iso*-octane ignition, Combust. Flame 145 (3) (2006) 552-570.

[45] D. Healy, D.M. Kalitan, C.J. Aul, E.L. Petersen, G. Bourque, H.J. Curran, Oxidation of C1−C5 Alkane Quinternary Natural Gas Mixtures at High Pressures, Energy Fuels 24 (3) (2010) 1521-1528.

[46] CHEMKIN-PRO 15112, Reaction Design: San Diego, 2011.

Chapter 4: Understanding the Effects of Boundary Layers on Ignition of Fuels with Complex Temperature Dependence

4.1 Introduction

All experimental studies on autoignition behavior will be impacted at some level by facility effects on observed ignition behavior. **Chapter 3** focused on the localized thermal gradients present in an experimental setup and the effect of thermal gradients on ignition behavior based on the sensitivity of a mixture to autoignition. This chapter focuses on a similar thermal sensitivity that can impact ignition measurements. In **Chapter 3**, local thermal non-uniformities on the order of 5 K/mm were considered as temperature gradients induced by turbulent fluent motion. Here, the effects of thermal boundary layers are considered. Thermal boundary layers produce bulk temperature gradients on the order of 200 K/mm, for example near the wall of an autoignition reactor. The high activation energy of ignition chemistry typically quenches the reaction rates near the cooler walls of a reactor. However, fuels that exhibit negative temperature coefficient (NTC) behavior are characterized by higher reaction rates with decreasing temperature for specific ranges of temperatures and pressures. The hypothesis of this study is as follows. If the thermal boundary layer spans state and mixture conditions where NTC reactivity is high, the thermal boundary layer can impact the observed autoignition characteristics and, consequently, the experimental data require more nuanced interpretation of the results. Further, complex NTC behavior may be responsible for the higher level of scatter observed in the NTC region for many fuels. To test the hypothesis that NTC chemistry is affecting autoignition results, a combined modeling and physical experimental approach is used here.

Differences between shock tube and RCM ignition delay time (IDT) data at lower temperatures (e.g., < 1800 K) and lower pressures (< 20 atm) have been discussed in the literature, e.g., Petersen et al. [1] and Lam et al. [2], without a clear conclusion on what is responsible for the discrepancies between experimental approaches. However, notably, experimental autoignition data tend to exhibit higher scatter and lower repeatability in the NTC region for many fuels, as highlighted in the study of n-heptane by Campbell et al. [3] where the experimentally measured ignition delay times diverged by almost an order of magnitude from the kinetic model predictions within the NTC region and much less pronounced NTC behavior relative to that predicted by the model.

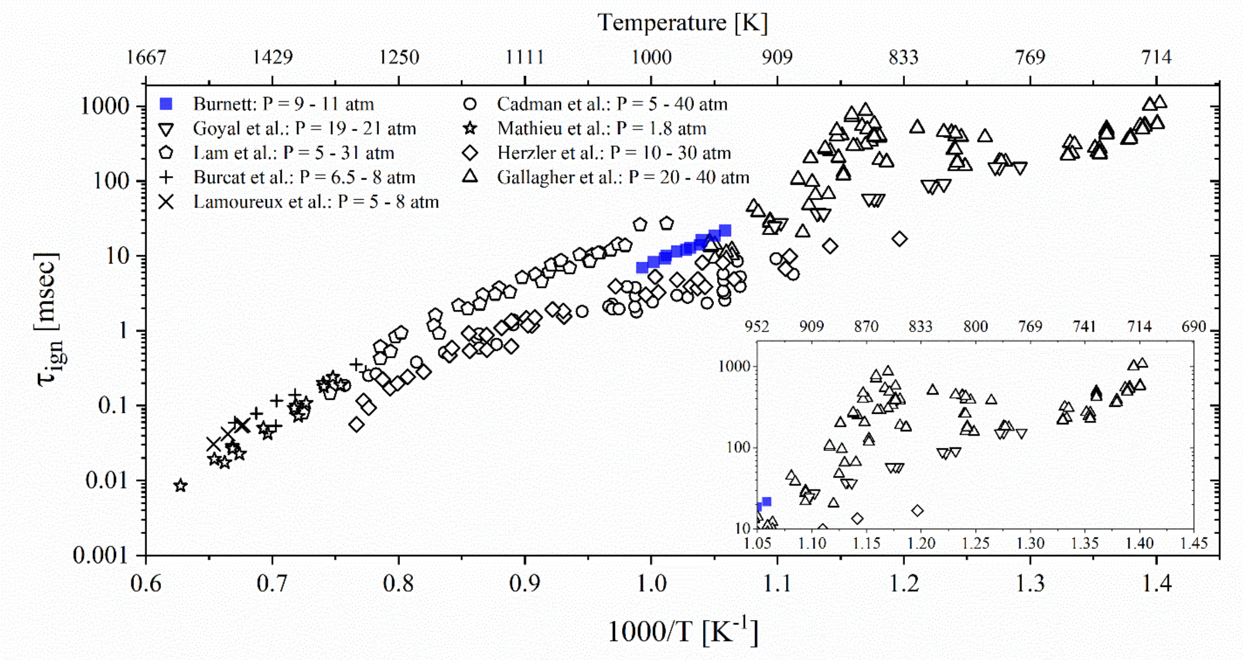

Figure 4.1: Summary of ignition delay time data for propane/air mixtures at ϕ=0.5 from **Figure 3.1**with UM-RCF results added. The data have been normalized to P = 10 atm using scaling of $\tau_{ign} \propto 1/P$ and highlight the additional scatter in experimental results as the thermodynamic conditions enter the NTC region. The insert plot highlights the results within the NTC region and the roughly two order-of-magnitude scatter at conditions below 900 K.

Understanding ignition inhomogeneities in the near-wall region of combustion chambers is a topic of interest within the combustion community, especially within the context of RCM and shock tube experiments where high-speed imaging through a transparent end-wall allows for direct observation of ignition behavior. Several groups have sought to better understand this topic through both experimental work and computational modeling of different causes of inhomogeneous phenomena. As discussed in detail in **Chapter 3**, localized ignition events have been demonstrated to result from changes in the autoignition regimes based on mixture composition, end-of-compression state conditions and facility-dependent phenomena. While localized ignition due to autoignition regime differences (weak vs. strong ignition) and NTC chemistry are distinct behaviors, their appearance may be similar when observed through different imaging techniques and convolved with one another, making *a priori* predictive methods like the Sankaran Criterion (**Chapter 3**) valuable tools for interpreting autoignition behavior.

Multiple computational studies on NTC behavior have been conducted to better understand its possible impact on ignition behavior. One of the earliest studies to consider the possibility of boundary layer ignition prior to the core gas region of an NTC fuel was conducted by Griffiths et al. [4] and focused on modeling the alkane components of gasoline within an RCM at conditions where the NTC region was expected to impact ignition behavior. Computational fluid dynamics (CFD) modeling of the impacts of turbulence (creating localized pockets of fuel at NTC conditions within an RCM) were conducted by Mittal et al. [5] to study the suitability of a common 0-D approach in predicting ignition behavior of NTC fuels at low temperature conditions. Jayachandran and Egolfopoulos [6] studied diffusion effects on boundary layer ignition of NTC fuels using a 1-D model and found NTC behavior led to localized ignition centers within the boundary layer. Dai et al. [7] used a 1-D planar numerical model to identify ignition modes at a “cool spot” within the NTC region of n-heptane. The computational studies concluded that NTC behavior could lead to localized ignition behavior when these “cool spots” or boundary layers fall within the NTC region.

Figure 4.2 provides a comparison of IDT predictions for multiple combustion reaction mechanisms using detailed chemistry that have been developed for propane and other small alkanes (i.e., C5 and smaller). The IDT values are provided for propane-air mixtures at $\phi = 1.0$ and P = 20 atm and a range of temperature including high temperature, NTC, and low-temperature regions. The four reaction mechanisms are from Healy et al. [8], Gokulakrishnan et al. [9], the San Diego Mechanism [10], and Cord et al. [11], and the differences highlight the uncertainty in predictive capability for ignition behavior within the NTC and low-temperature combustion regions. The Healy et al. [8] mechanism was developed for a broad range of temperatures (650 – 1550 K), while the Gokulakrishnan et al. [9] and Cord et al. [10] mechanisms were developed for low temperature oxidation (< 950 K), and the Cord et al. [11] mechanism was developed for flame speed and high temperature ignition/detonation studies. Within the NTC region, the maximum observed ignition delay time difference is between the Cord et al. [11] mechanism and the San Diego Mechanism [10] and results in a difference of more than an order of magnitude. Notably, there are discrepancies between the model predictions using the different reaction mechanisms at low and high temperatures as well. Similar discrepancies between different mechanisms, as well as a notable difference between the model predictions and experimental results, within the NTC region was also identified for n-heptane by Campbell et al. [3] demonstrating that this phenomenon is not fuel-specific to propane.

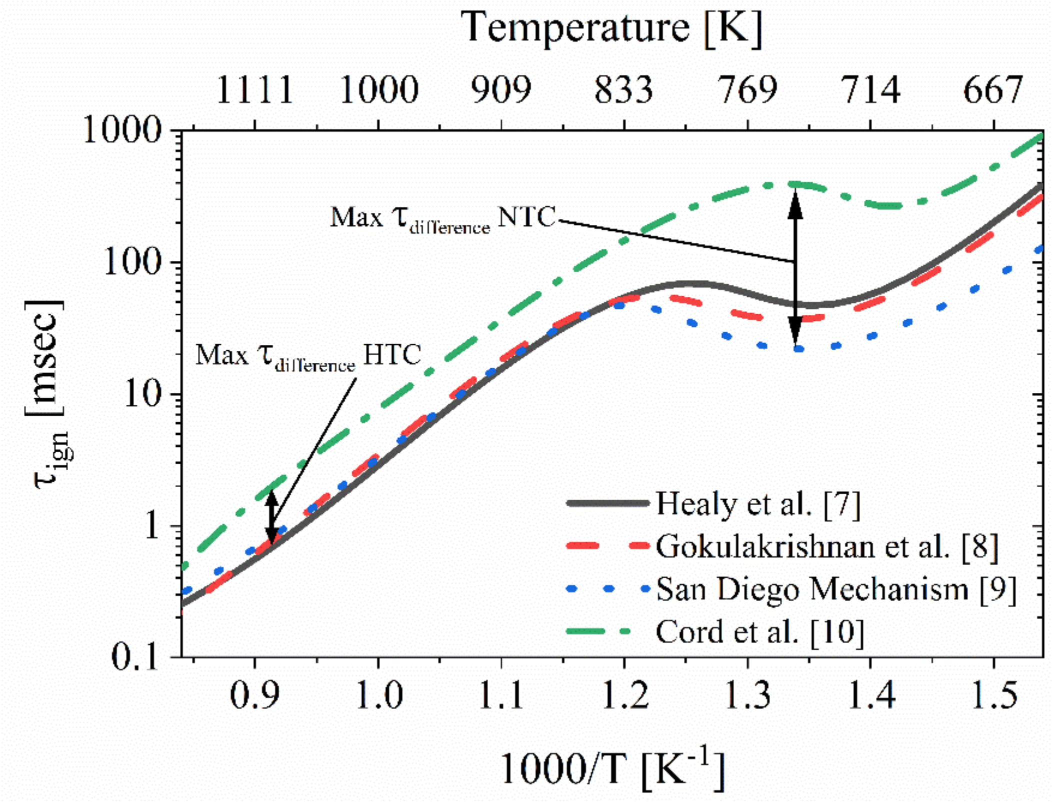

Figure 4.2: Comparison of ignition delay time predictions for propane-air mixtures at ϕ = 1.0 using different detailed propane combustion reaction mechanisms.

A summary of previous experimental studies on the impact of temperature inhomogeneities in general, and on propane ignition in particular, is provided in **Chapter 3**. Most of the studies focused on non-NTC fuels or on conditions outside of the NTC region; however, some experimental studies have specifically focused on NTC IDT measurements. Healy et al. [8] studied ignition behavior and developed an elementary chemical kinetic mechanism for C1-C5 alkanes that captured the NTC behavior in natural gas blends. Shao et al. [12] used end-wall imaging in a shock tube to study homogeneous and inhomogeneous ignition of n-heptane within and just outside of the NTC region. Bogin et al. [13] studied the NTC behavior of alkanes in an ignition quality tester (IQT) and noted the discrepancy between IQT and RCM data within the NTC region. Zhang et al. [14] studied first-stage ignition behavior within the NTC region for *iso*-octane and methyl-cyclohexane. Houidi et al. [15] examined how thermal gradients within the NTC region impact RCM studies where a flat piston was used to compress the test gas. Yunliang et al. [16] studied autoignition behavior under super knock conditions for both an NTC fuel (*iso*-octane) and a non-NTC fuel (methanol) and commented that boundary layer ignition leading to knock that was observed in their facility may not have been influenced by the NTC behavior of a fuel but could be a result of other factors. Recently, Liu et al. [17] discussed the ignition behavior of *iso*-octane within and below the characteristic temperatures of the NTC region. The common theme among these experimental studies is the complexity of the fluid interactions (such as thermal boundary layer development and mixing) and NTC chemistry on ignition observations, leading to generally higher scatter in the experimental results for IDT in the NTC region, and therefore higher uncertainty in the data used to develop and validate NTC chemistry. The gap in the literature is a study specifically focusing on quantifying (computationally and experimentally) the effects of thermal boundary layers and NTC reaction chemistry on IDT measurements. The current work contributes to filling this gap using a combination of modeling and physical experiments. A key issue that has not been considered in previous studies is the effect of expansion and compression work of the thermal boundary layer and core regions of the test gas mixture on ignition measurements. Evaluation of these expansion and compression effects is the major focus of the current work. Propane was selected as the test fuel for the study because it is the simplest hydrocarbon that exhibits NTC behavior as well as its industrial importance, the wealth of experimental data on propane, and the robust reaction chemistry available for modeling propane combustion. A summary of previous experimental studies of propane ignition that span RCMs, shock tubes, flow reactors, and jet stirred reactors and the associated state and mixture conditions of these studies is provided in **Chapter 3**.

The work presented in this chapter focuses on state conditions where the boundary layer spans the NTC region (based on the elementary reaction mechanism by Healy et al. [8]) specifically, pressures from 10 to 30 atm and temperatures below 1000 K. The study approach was two-fold: a two-zone computational model using the detailed reaction chemistry by Healy et al. [8] was created to represent the core and boundary layer regions in an RCM or shock tube. The model was used to identify the magnitude of the potential effects of NTC chemistry on overall ignition delay times (as would be measured in RCM and shock tube experiments) and the location of ignition events (specifically, ignition in the boundary layer preceding ignition in the core region and vice versa). The model results were then used to design RCM experiments with test conditions that transition between different ignition characteristics. To span the broad range of conditions identified as relevant during modeling, two experimental facilities were used. Experiments were conducted in the Tsinghua University RCM (TU-RCM) at temperatures between 744 and 908 K and pressures between 19.1 and 25.4 atm and in the University of Michigan RCF (UM-RCF) at temperatures between 911 and 1044 K and pressures between 9.4 and 10.0 atm. The modeling and experimental results are discussed in terms of the implications on measured ignition delay times and the ability to accurately predict and interpret fuel ignition behavior within the NTC region.

4.2 Methodology

4.2.1 Computational Methodology

Single- and two-zone models, both using detailed chemistry, were created and used to investigate the effects of a thermal boundary layer on ignition time and location of ignition. The models used Chemkin [18] and Cantera [19] software, and the Healy et al. [8] reaction mechanism for C1-C5 alkanes. Both the single- and two-zone model are based on closed homogenous reactor assumptions with constant total volume (V_{total}). The single-zone reactor model was created using Chemkin to study heat release and species production at specific temperatures and pressures and provided baseline ignition delay time (IDT) predictions for comparison with the two-zone model and the experimental results. Additional Chemkin flame speed predictions and ignition results were utilized to map the ignition regime space based on the Sankaran Criterion describe in **Chapter 3** and to understand when weak or strong ignition behavior could be expected under different experimental conditions. The two-zone "balloon" model was created using Cantera, where each zone used separate initial conditions and could interact with the other zone only by expansion or compression work. The gas was not allowed to mix between zones, i.e., each zone was closed with fixed mass. Given the time required for mass transfer by diffusion, compared with the chemical reaction times of ignition (<100 ms), this representation is appropriate for this simple model. If turbulent mixing were expected, as in a reciprocating engine designed to enhance mixing, this assumption would not be valid.

To represent a range of thickness for the thermal boundary layer, the volume fraction of the core region, i.e., the higher temperature central region of an experimental reaction chamber away from the walls, is defined as:

$$\frac{V_{core}}{(V_{core} + V_{annulus})} = \frac{V_{core}}{V_{total}} \tag{1}$$

where, $V_{annulus}$ is the volume of the thermal boundary layer, i.e., the annulus region of the cooler gases near the reaction chamber wall. The energy transfer between zones occurs by equalizing the pressure in each zone at time step, i.e., pressure is always constant throughout the chamber.

4.2.2 Experimental Methodology

Experiments conducted in the UM-RCF for this study followed the same procedures as those outlined in **Chapter 3**. The experiments were conducted at stoichiometric conditions, $\phi = 1.0$, with an O_2-to-diluent ratio of 7.5. N_2 (PurityPlus, >99.999%), CO_2 (PurityPlus, >99.995%), and Ar (PurityPlus, >99.999%) were used as diluents to control the pressure and temperature conditions within the test section, which ranged from 9.4 – 10.0 atm and 911 – 1044 K, respectively. The mixture compositions studied in the UM-RCF are summarized in **Table 4.1**.

Table 4.1: Composition for the three mixtures studied in the UM-RCF.

Mixture	T_{goal} [K]	ϕ	C_3H_8 [%]	O_2 [%]	N_2 [%]	Ar [%]	CO_2 [%]
1	1050	1.0	2.29	11.55	64.67	21.48	0.00
2	1000	1.0	2.29	11.55	75.39	10.77	0.00
3	925	1.0	2.29	11.55	81.04	0.00	5.12

Di et al. [20] provides a detailed description of the TU-RCM that was used for the higher-pressure and lower-temperature propane ignition studies. Briefly, the TU-RCM uses a creviced piston driven by a series of hydraulics to rapidly compress a test-gas mixture. A high-pressure chamber filled with air provides the power to propel the piston and compress the test gas, while a high-pressure chamber filled with oil serves as the “brakes” for the system, holding the piston in the starting position and serving as a damper for piston motion near the end of compression (EOC). The test section has an inner diameter of 50.8 mm and has an adjustable length between 13 to 80 mm to control the compression ratio of the system. The driven section has the same 50.8 mm diameter as the test section and a length of 0.5 m that defines the distance of the compression stroke. A pressure transducer (Kistler 6125C) and charge amplifier (Kistler 5018) were used to measure pressure within the test section, while images were recorded using a high-speed camera

(Photron SA-X2) with a 35 mm lens (Nikon Nikkor 1:1.8G) at a frame rate of 288,000 frames per second with 128 x 128-pixel resolution. Additional details on the high-speed imaging methodologies using the TU-RCM can be found in Qi et al. [16] and Wang et al. [21]. The propane, oxygen, nitrogen, and argon gases used for these experiments were all ultra-high purity gases (>99.999%, AirLiquide). The mixture compositions studied in the TU-RCM are summarized in **Table 4.2**.

Table 4.2: Mixture compositions for the three mixtures studied in the TU-RCM.

Mixture	**T_{goal} [K]**	**ϕ**	**C_3H_8 [%]**	**O_2 [%]**	**N_2 [%]**	**AR [%]**
1	900	1.0	4.03	20.16	6.06	69.74
2	850	1.0	4.03	20.16	16.85	58.96
3	750	1.0	4.03	20.16	54.15	21.66

4.3 Computational Results

Results for IDT from the single zone Chemkin simulations are shown in **Figure 4.3**. The location of the NTC region and the magnitude of the effect on IDT are a function of pressure and temperature, with less pronounced impact at 1 and 100 atm relative to the 20 atm conditions shown in the figure. To be precise, at 1 atm and 100 atm, the chemistry does not lead to “negative” temperature coefficient behavior at all; instead, the slope of the model predictions is changed slightly but remains positive throughout the temperature range considered. Note that the Healy et al. [8] mechanism agrees well with high- and low-temperature IDT data as seen in **Figure 3.9** and **Figure 3.10** from **Chapter 3**. Based on the IDT sensitivity to NTC behavior, 20 atm conditions were chosen for the multi-zone modeling.

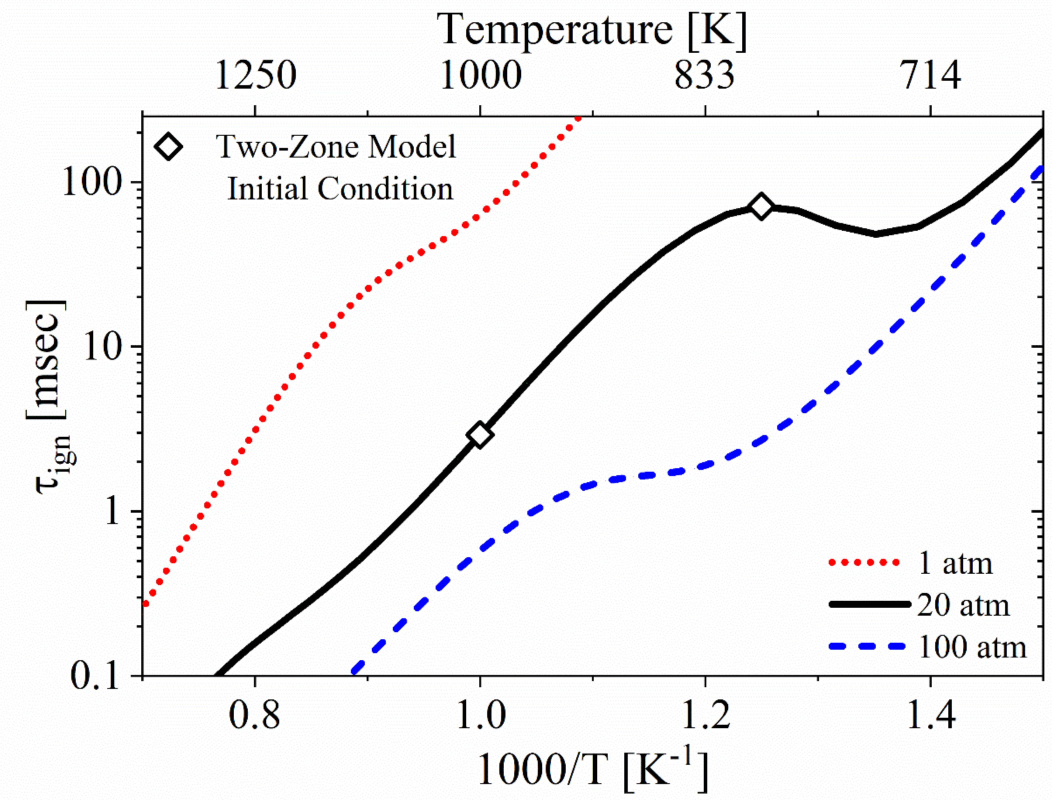

Figure 4.3: Ignition delay time for propane for $\phi = 1.0$, and air levels of dilution. The initial core-zone temperature conditions for the simulations listed in **Figure 4.4** and **Figure 4.5** are marked to highlight their proximity to the NTC region.

A large parametric space was studied using the two-zone model where the initial temperatures and sizes of the two zones were varied. The initial pressure was 20 atm for the two zone results presented here. Because the boundary layer was represented by a single zone, an average temperature between the initial temperature of the core region and the walls (298 K) was set for the initial temperature of the annulus ($T_{annulus}$). The average annulus temperature was always lower than the core temperature (T_{core}). A range of temperature differences ($\Delta T = T_{core} - T_{annulus}$) was tested from $\Delta T = 10 – 100$ K, spanning the range of conditions expected during RCM and shock-tube experiments from core temperatures of 670 – 1000 K. For reference, a temperature difference of 75 K was measured in the UM-RCF study by Donovan et al. [22] at, and immediately after, the end-of-compression.

Simulation results for the ignition delay times for the core and annulus regions for a range of relative volumes are presented in **Figure 4.4** and **Figure 4.5**. The results are for two initial core temperatures of 1000 K and 800 K, respectively. The model predictions for a single reaction zone are shown in the figures for reference as solid lines. At the higher temperature, **Figure 4.4** shows the size of the boundary layer has negligible impact on the IDT of the core region, and IDTs for the core region are in excellent agreement (< 5% difference) with predictions for IDT based on the single-zone model when the high-temperature core region is > 50% of the test volume. The results are consistent with expectations since both the core and annulus region are outside the NTC region expected for P = 20 atm, as seen in **Figure 4.3**. The results also show ignition of the boundary layer only discernably lags the IDT of the core for conditions where the boundary layer is quite large (> 75% of the total volume).

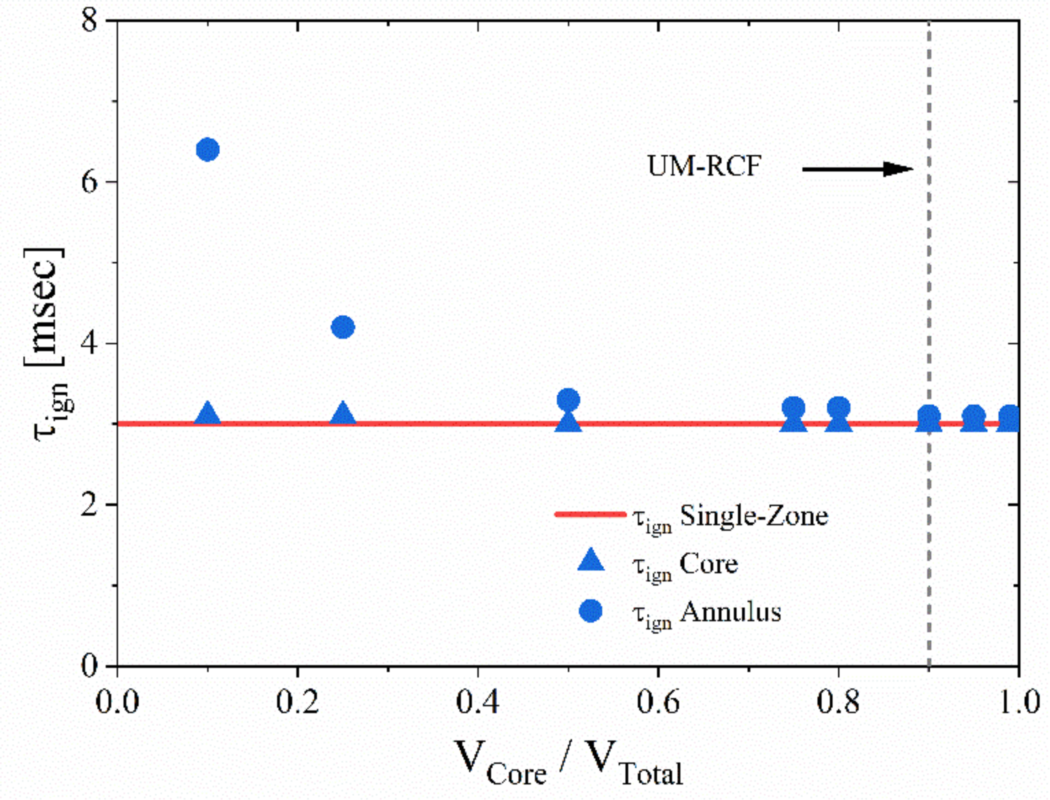

Figure 4.4: Ignition delay time predictions for an initial pressure of 20 atm, an initial core temperature of 1000 K and an initial annulus temperature of 925 K. The IDT for the single zone model with an initial temperature of 1000 K is provided for reference. The typical core volume fraction expected immediately after end of compression in the UM-RCF is shown as the dotted line.

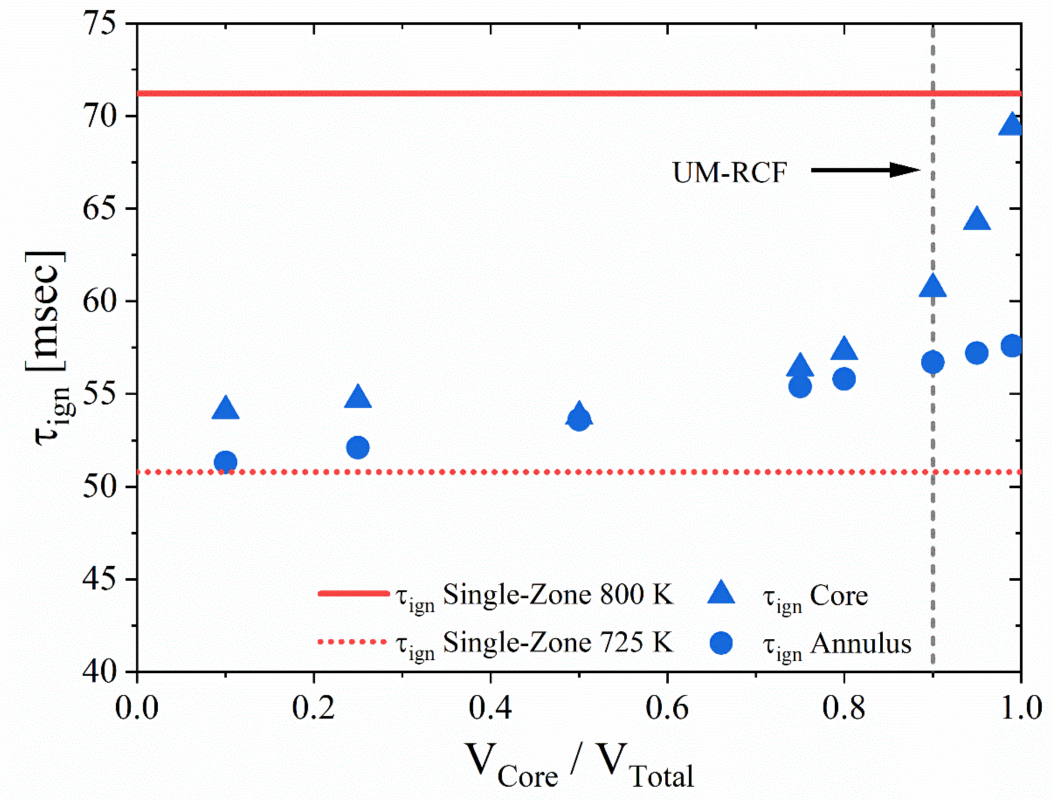

Figure 4.5: Ignition delay time predictions for an initial pressure of 20 atm, an initial core temperature of 800 K and an initial annulus temperature of 725 K. The IDTs for the single zone model with an initial temperature of 800 K and 725 K are provided for reference.

The lower temperature results presented in **Figure 4.5** show very different behavior, where all results with a core volume fraction less than 100% are markedly faster than the single-zone model predictions for IDT (e.g., by over ~15 ms or 20% for V_{core}/V_{total} ratios less than 75%). For these simulations, the initial temperature of the annulus is in the NTC region and the initial temperature of the core is at the start of the region of high-temperature chemistry (see **Figure 4.3**). Notably, even the smallest annulus volume fraction (i.e., largest core volume fraction) causes acceleration of the ignition of the core gases relative to the single-zone calculation. The acceleration of ignition of the core is due to compression heating by ignition of the annulus gases. Thus, the core and annulus IDTs are systematically faster than the single-zone model. Specifically, ignition delay times for V_{core}/V_{total} ratios between 0.8 and 1 (which might be considered typical for RCMs and shock tubes with larger diameters and overall volumes), show significant divergence between the core and the annulus, with the annulus region igniting between 1-12 ms faster than the core. The annulus ignition causes the core region to ignite between 2-14 ms faster than the single-zone predictions. Specific values for the different IDTs are provided in **Figure 4.3** for the V_{core}/V_{total} = 0.9 simulations. For the lower initial temperature condition, there is a 4 ms difference (7%) between the core and the annulus ignition delay time and a 10 ms difference (14%) between the core IDT and the single-zone model. At the higher temperature initial condition, the differences between the core, annulus, and single-zone IDTs are small (< 0.25 ms, < 3%) and well within experimental and computational uncertainties.

As the volume fraction of the core decreases below 50%, the IDT of the annulus approaches the IDT for a single zone at the initial temperature of the annulus. However, since some thermal energy is lost to compression of the core region, the IDT of the annulus is slightly slower than the single-zone limit. Importantly, the results indicate the NTC effects have observable impact on the IDT of the system, and all RCM and shock tube reactors are affected to some extent, regardless of the size of the boundary layers, if the state conditions span similar regions and levels of NTC reactivity.

Table 4.3: Summary of initial conditions and results for the two-zone model results for $V_{core}/V_{annulus}$ = 90%, shown in **Figure 4.6**.

	Low temperature initial condition	**High temperature initial condition**
Initial Core Temperature (K)	800	1000
Initial Annulus Temperature (K)	725	925
Initial Pressure (atm)	20	20
Core IDT (ms)	61	3.0
Annulus IDT (ms)	57	3.1
Single-Zone IDT (ms)	71	3.0

Figure 4.6 presents a visual representation of the two-zone model predictions for temperature and volumes for V_{core}/V_{total} = 0.9 for three characteristics times: before ignition, when the first zone ignites, and when the second zone ignites. At the high temperature condition, after the core ignites, the expansion of the core gases compresses the boundary layer/annulus region. The compression work increases the temperature of the boundary layer, accelerating ignition of the cooler gases, so the ignition of the two regions is nearly simultaneous. The lower temperature simulation shows ignition occurs first in the annulus, which causes significant expansion of the annulus gases, and compression of the core region. The compression work on the core gases accelerates the high

temperature chemistry of the core, causing the gases to ignite at a notably faster time than the single zone model predicts.

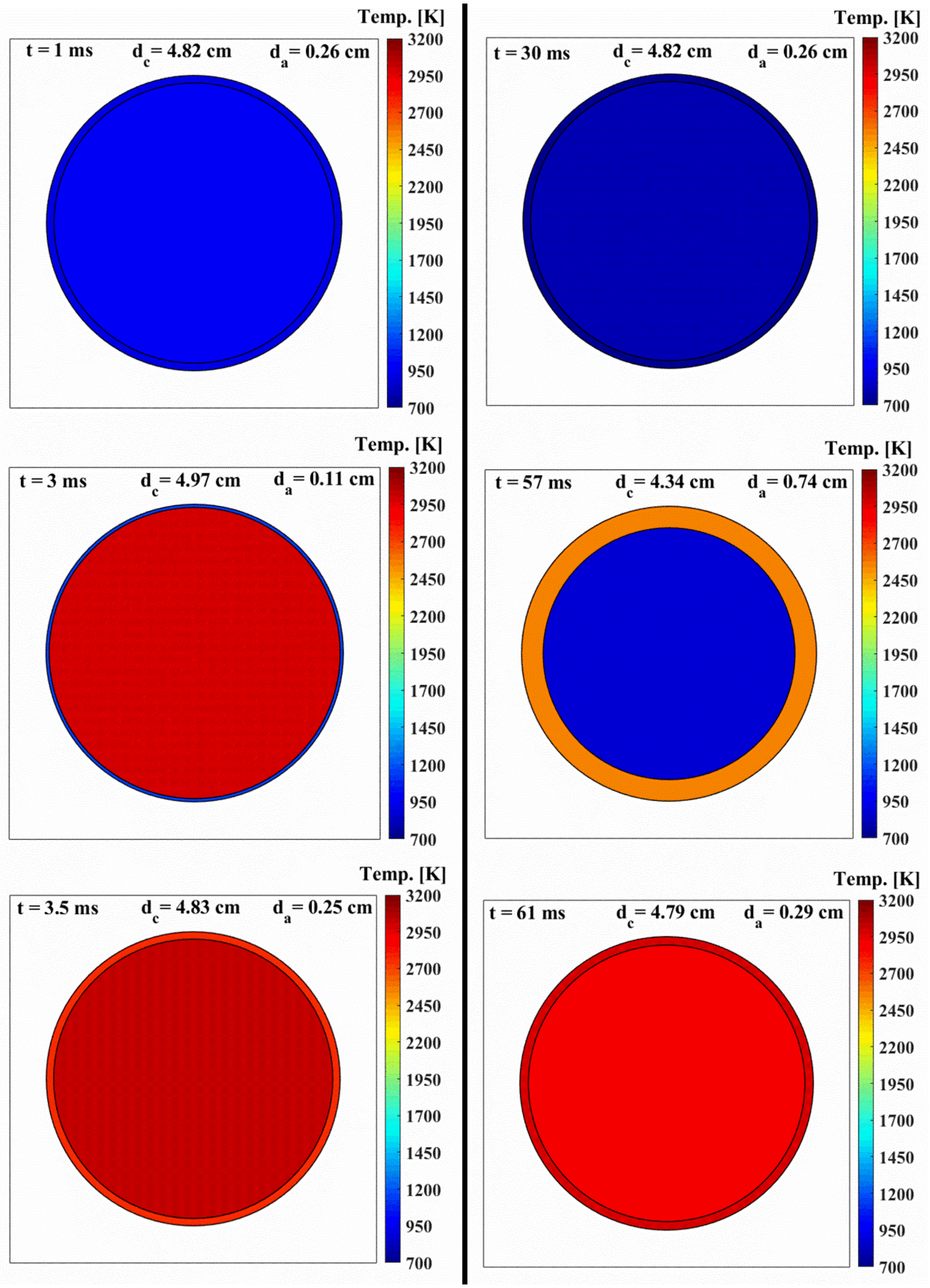

Figure 4.6: Comparison of the two-zone model predictions for temperature and volume as a function of time for high-temperature initial conditions (right column) and low-temperature initial conditions (left column) for $V_{core}/V_{annulus}$ = 90%. Additional simulation conditions are summarized in **Table 4.3**.

4.4 Experimental Results

The modeling results guided the experimental efforts to confirm the effects of NTC and thermal boundary layers on IDT measurements. Specifically, the approach was to conduct a series of experiments similar to the modeling efforts, where NTC behavior would be amplified or de-amplified based on the end-of-compression conditions. Namely, ignition data would be collected over a range of core temperatures. The thermal boundary layer spans the NTC region for all experiments; however, the IDT of the core region is faster at higher temperatures and slower at lower temperatures and therefore more susceptible to NTC effects from the boundary layer. The diagnostics included end-view imaging, similar to the visualization of the model results presented in **Figure 4.6**, and IDT measurements based on pressure time histories.

An additional challenge for the experiments was to minimize the effects of weak and strong ignition regimes. Mapping the strong and weak autoignition regimes was done using the Sankaran Criterion, as outlined in **Chapter 3**, for the NTC propane mixture conditions (namely an equivalence ratio of 1.0 and N_2/O_2 of 7.5). The same experimental methods described in **Chapter 3** were applied using the UM-RCF. The results of the regime-mapping experiments are provided in **Figure 4.7**(**a)**, where the symbols indicate whether strong or weak autoignition was observed at the P and T conditions of the experiments. **Figure 7(b)** shows a comparison between the experimental measurements and single-zone model predictions for IDT. The ignition regime transition was consistent with the theory and results presented in **Chapter 3**, and for homogeneous/strong ignition results, the IDTs were in good agreement with single-zone model predictions (within 18%). The two-zone model results, presented in **Figure 4.7**(**b)**, show similar agreement with experimental results at strong-ignition conditions (within 10%). Typical imaging data demonstrating inhomogeneous (i.e., weak or mixed) ignition and homogeneous (strong) ignition behavior are provided in **Figure 4.8**. As expected, based on the mixture and state conditions, the results showed no characteristics associated with NTC chemistry in the thermal boundary. Lower temperatures were not achievable with the UM-RCF without introducing significant uncertainties due to very long test times (> 100 ms), so further experiments were conducted at lower temperature and higher-pressure conditions studied using the TU-RCM.

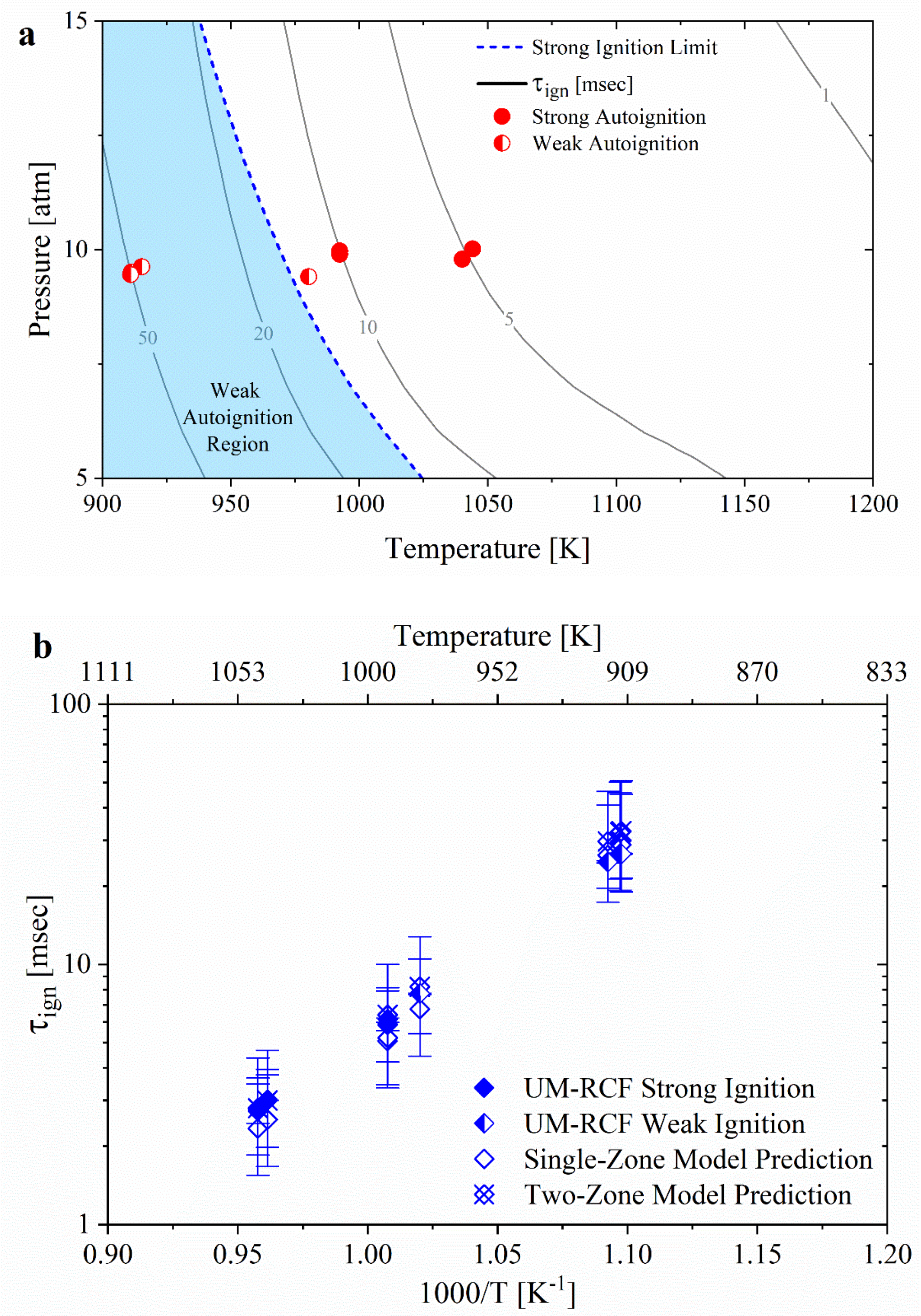

Figure 4.7: (a) Ignition regime diagram and (b) UM-RCF experimental results for propane mixtures with $\phi = 1.0$ and an N_2/O_2 of 7.5.

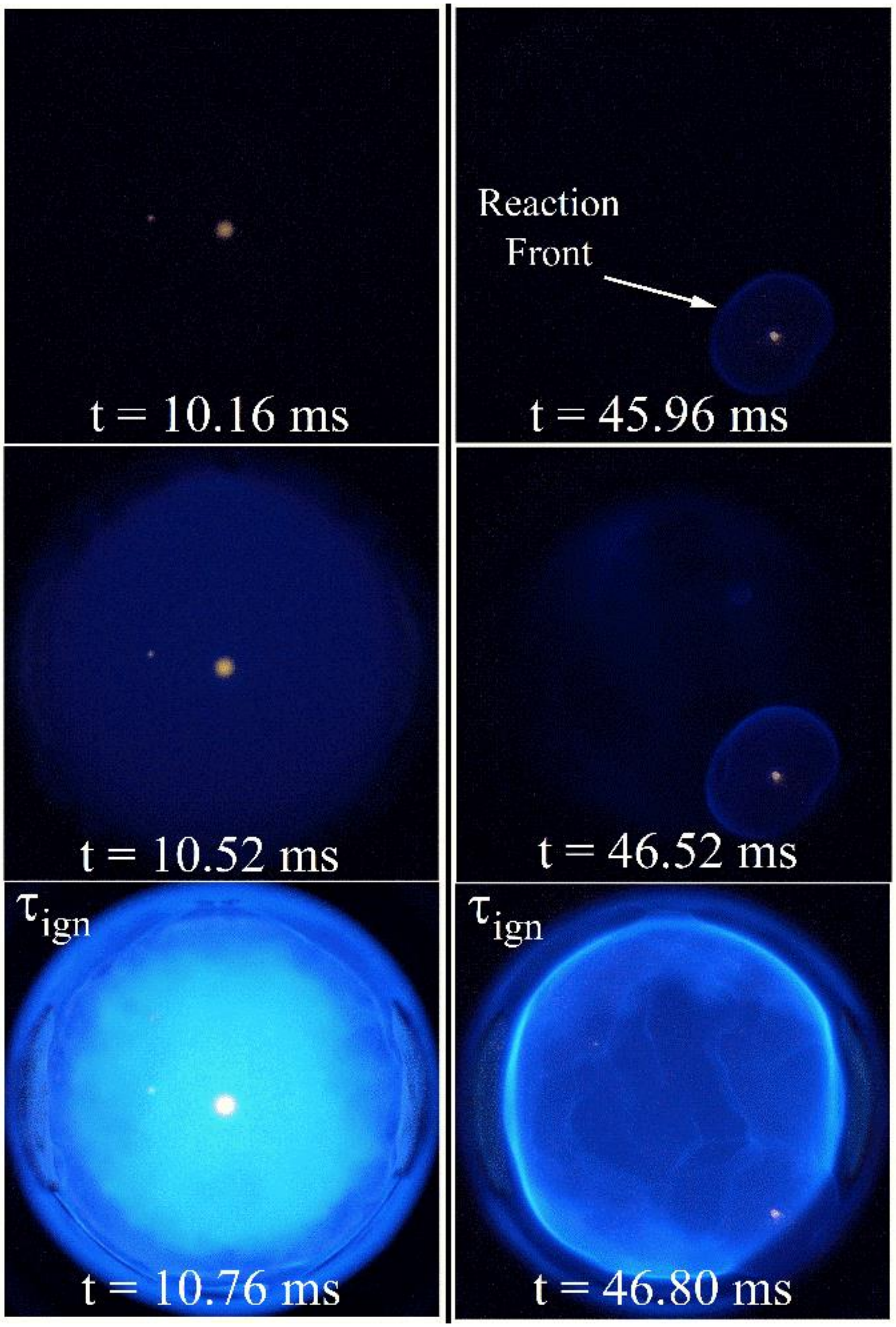

Figure 4.8: Imaging results from typical inhomogeneous/weak ignition (right column) and homogeneous/strong ignition (left column) UM-RCF experiments for stoichiometric propane mixtures with N_2/O_2 of 7.5. The results exhibited similar characteristics as the results presented in **Chapter 3** for fuel lean propane mixtures.

For the TU-RCM, lower levels of dilution were used than with the UM-RCF experiments (3.76:1 inert gas to O_2 ratio compared with 7.5:1). The lower levels of dilution combined with the pressures of 20 atm and 25 atm and temperatures of 750 K, 850 K, and 900 K were selected because the two-zone model predictions indicated the core region would have comparable or slower ignition delay times compared with the thermal boundary layer. **Figure 4.9a** shows the experimental conditions relative to the different ignition regimes and the NTC region. Most of the experimental conditions were within regions where weak autoignition behavior is expected, meaning care must be taken when interpreting the imaging data to distinguish between boundary layers and other thermal gradients created by fluid mixing. The measured IDT data are compared with single- and two-zone (with $V_{core}/V_{annulus}$ = 90%) model predictions in **Figure 4.9b** for the 20 atm conditions and **Figure 4.9c** for the 25 atm conditions. The model still performed well at predicting ignition within the TU-RCM (within 35% across conditions) but showed greater difference than the strong ignition conditions studied in the UM-RCF. The largest differences were observed at the 750 K conditions at both 20 and 25 atm, but these still fell within the uncertainty for the single-zone model. Two-zone model predictions were within 5% of the IDTs predicted by the single-zone model.

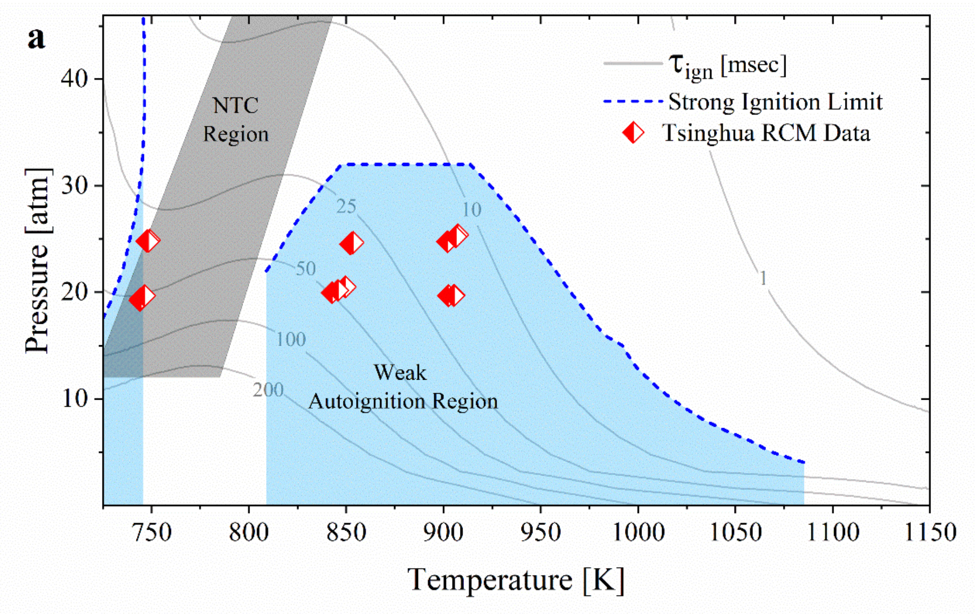

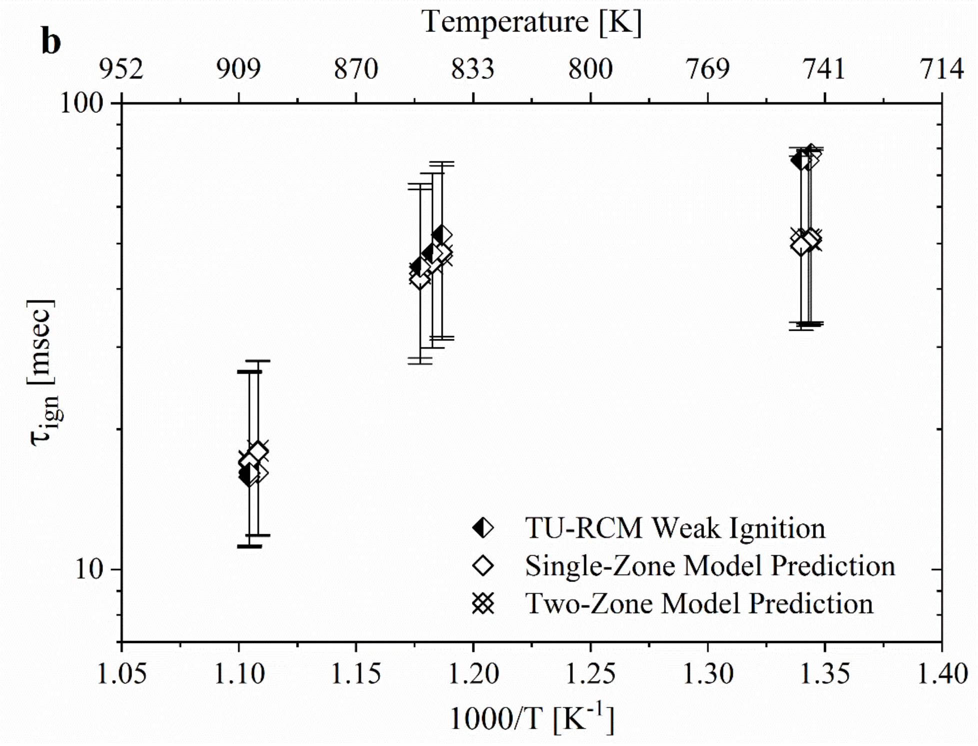

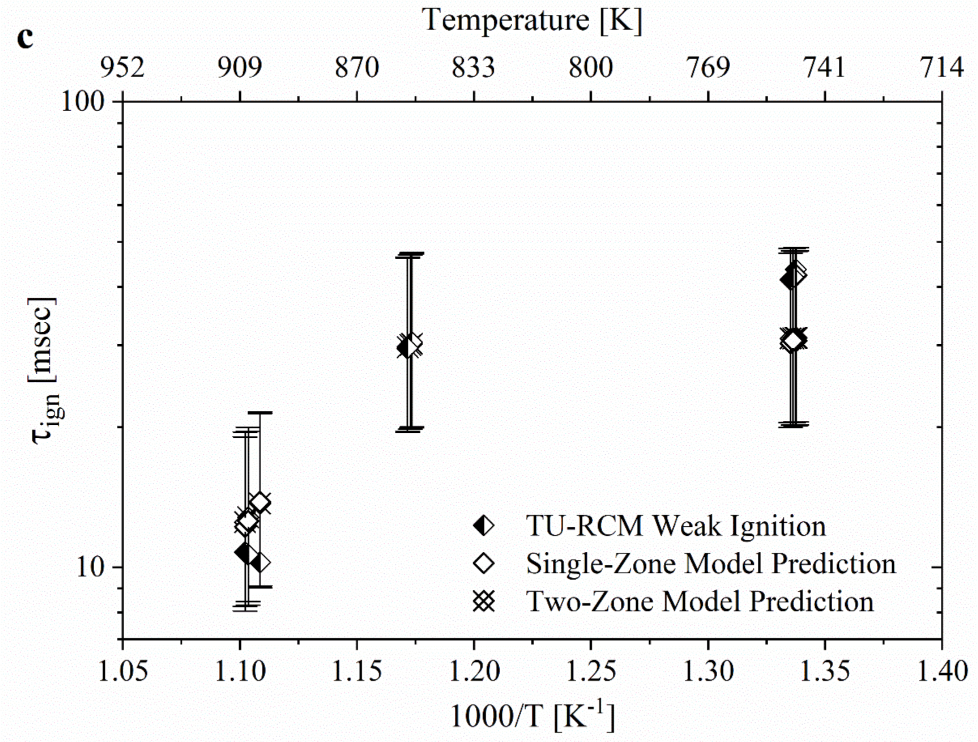

Figure 4.9: (a) Ignition regime diagram and TU-RCM experimental results at (b) 20 atm and (c) 25 atm for propane mixtures with $\phi = 1.0$ and air levels of dilution ($N_2/O_2 = 3.73$).

Figure 4.10 and **Figure 4.11** show ignition imaging data from three temperature conditions for P = 20 atm and P = 25 atm, respectively. Six frames from each series of images are shown for each experimental condition. The last frame in each series is the time of ignition based on the magnitude and spatial extent of the intensity in the test section. The IDT based on image intensity correlates virtually identically (within <1%) with the IDT based on pressure time history data for each condition. In each image sequence, spatially inhomogeneous reaction is observed before volumetric ignition occurs (characterized by the maximum emission intensity during the experiment). These characteristics of mixed ignition are expected based on the ignition regime of the experiments (see **Figure 4.9a**). However, there are key differences in the observed inhomogeneities that may be attributable to NTC effects in the thermal boundary layer. At the T = 750 K and 850 K conditions, the imaging captures an increase in chemiluminescence prior to the time of volumetric ignition (based on the observation of maximum intensity). Specifically, the distribution of the chemiluminescence within the chamber is around the periphery, i.e., annulus of the test chamber. This behavior is especially pronounced in **Figure 4.11(b)**, where an almost circular core region with negligible chemiluminescence is surrounded by a brighter region of gas. The imaging indicates the annulus is reacting more quickly than the core, despite the higher temperature of the core region. **Figure 4.10(b)** also shows two zones within the reaction chamber, with a darker core region near the center of the test section, surrounded by gases with intense blue emission. At the lower temperature of T = 750 K the effects are less distinct; as seen in **Figure 4.10(a)** and **Figure 4.11(a)**; however, ignition does initiate in the near wall region for both pressures at 750 K. The distinction between the 750 K and 850 K imaging may be, in part, due to the reduced impact of NTC chemistry at lower pressure and the limited temperature region of NTC chemistry (see **Figure 4.2**). At the T = 900 K conditions shown in **Figure 4.10(c)** and **Figure 4.11(c)**, no chemiluminescence is observed prior to ignition, and ignition starts for both conditions within the core region indicating that NTC behavior is not significantly impacting the experiments. It is also important to note the difference in time scales for the different temperature conditions. At 900 K, where NTC effects are expected to be less influential, the ignition process (from start of the first ignition site to volumetric ignition throughout the test section) takes less than 35 μs. At the lower temperatures, chemiluminescence is observed over 400 μs before volumetric ignition. The difference in observed IDT ~0.5 ms for experimental conditions affect by NTC and the thermal boundary layer is consistent with expectations based on the two zone modeling results, which predicted differences in IDT of ~5 ms between the two zones (see **Figure 4.5** and **Table 4.3**).

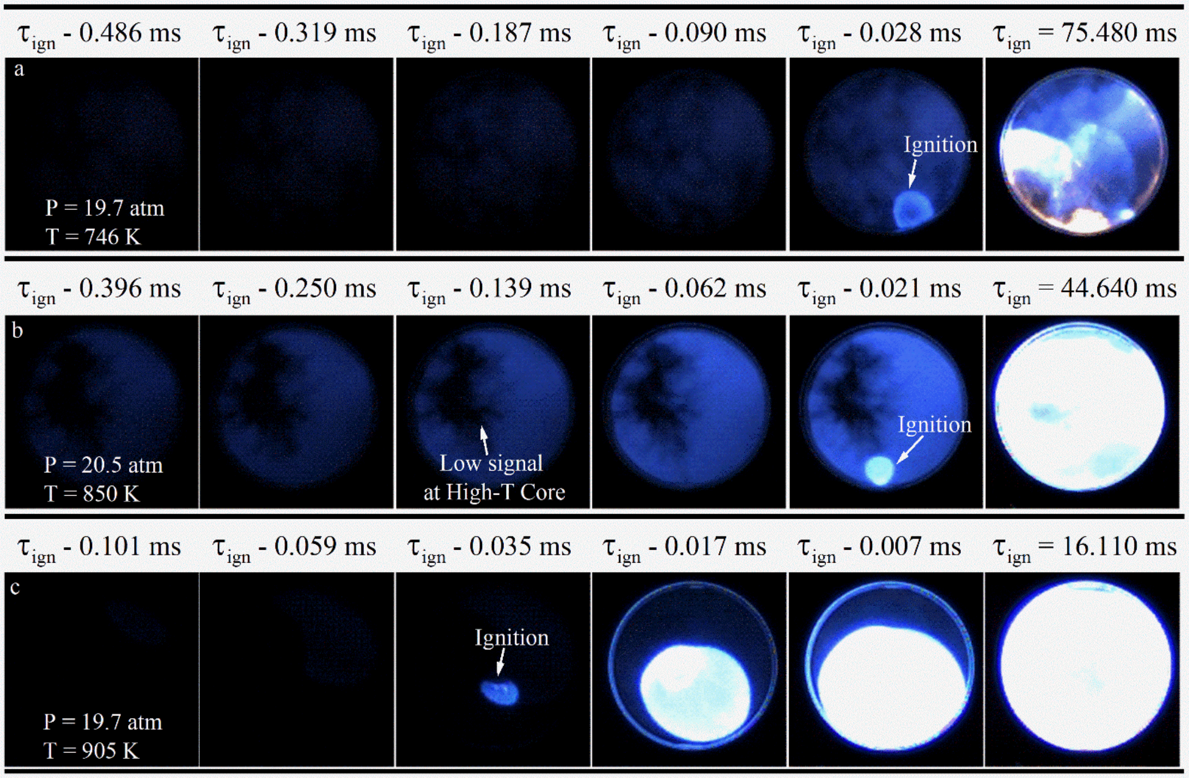

Figure 4.10: Ignition behavior observed at (a) 750 K, (b) 850 K, and (c) 900 K for the P = 20 atm stoichiometric propane-air experiments just before and at the point of ignition.

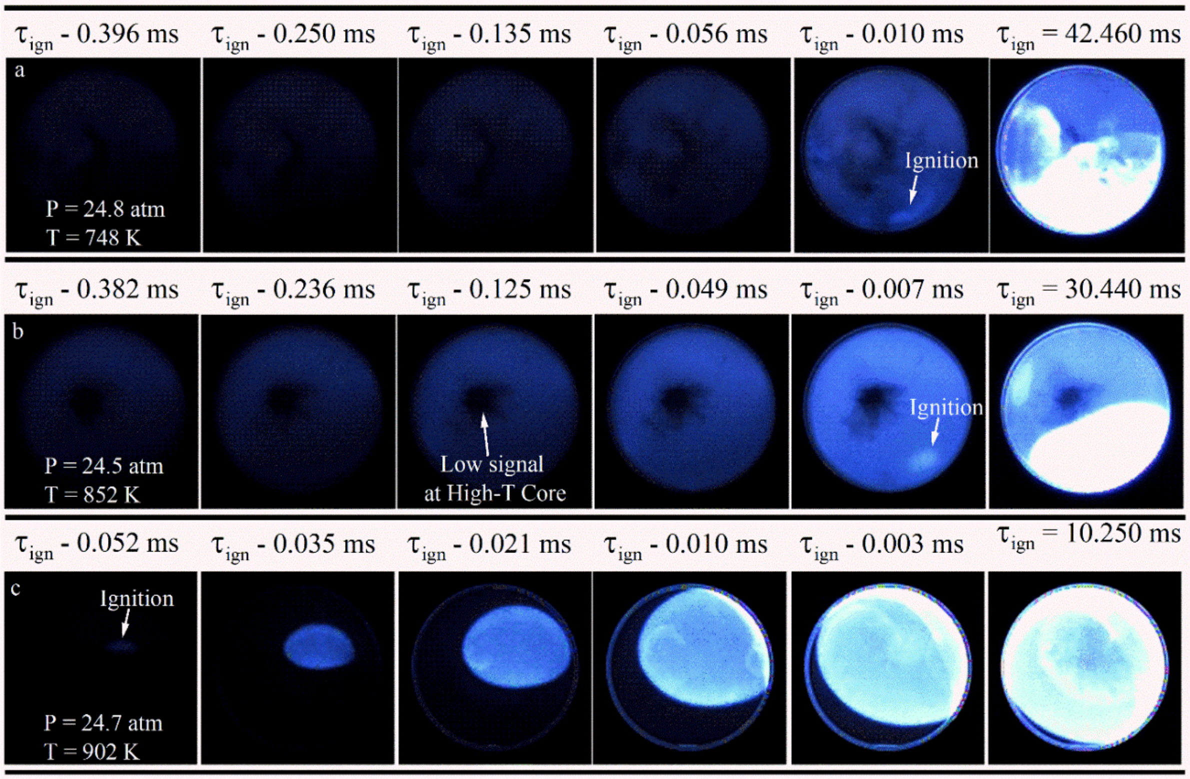

Figure 4.11: Ignition behavior observed at (a) 750 K, (b) 850 K, and (c) 900 K for the P = 25 atm stoichiometric propane-air experiments just before and at the point of ignition.

4.4.1 Ignition Delay Time Measurements

Ignition delay time results for the experimental ignition studies are shown in **Figure 4.7(b)** and **Figure 4.9(b)** and **Figure 4.9(c)** with comparisons to single-zone Chemkin model predictions and two-zone Cantera model prediction both using the Healy et al. [8] mechanism. Modeling uncertainty was assigned by variations in the A-factor for the top three reactions identified by sensitivity analysis using the same procedure as outlined in **Chapter 3**. Overall, the model predictions and experimental measurements agree well with one another, with the experimental measurements falling within the mechanism uncertainty at all studied conditions. The largest disagreement between mechanism predictions and experimental measurement is at the lowest temperatures, with the model underpredicting the measured IDT but the experimental data are still within the uncertainty bounds of the model.

It would be expected that a higher discrepancy between the experimental observations and modeling predictions would be observed at the 850 K conditions in the TU-RCM based on the chemiluminescence distribution within the chamber prior to ignition. However, the increase in chemiluminescence prior to ignition does not appear to meaningfully impact the experimental measurements relative to IDT predictions from the model. Both the 20 atm and 25 atm experiments at 850 K agree well with the model predictions as shown in **Figure 4.9**(**b)** and **Figure 4.9**(**c)**, suggesting that the additional chemiluminescence outside of the core region may not have a large effect on the ignition behavior of the mixture at these conditions.

4.5 Conclusions

While the modeling approach used here is simplified, key aspects of physical experiments are captured by the two-zone balloon model, including the thermal boundary layers present in all RCM and shock tube experiments and the fixed volume of many ignition experiments. The modeling results included initial temperatures and temperature gradients consistent with expectations of RCM and shock tube studies, where wall temperatures are typically ~298 K. Of course, in a physical experiment, the thickness of the boundary layer will evolve as a function of time and will be affected by fluid motion. Facilities with smaller test volumes and higher surface areas would be expected to have boundary layers that are a larger fraction of the total volume of the test sections. However, the two-zone model results indicate that IDT data from RCMs and shock tubes with larger volumes and comparatively smaller boundary layers will also be affected by NTC chemistry if the cooler boundary layer ignites before the core region of the test sections. The results of the modeling study here showed that all facilities, regardless of volume, are impacted to some extent by NTC behavior for specific state and mixture conditions.

The experimental results provide evidence to support the hypothesis that lower temperatures in thermal boundary layers combined with NTC chemistry are yielding observable effects during ignition experiments. The high-speed imaging data indicate increased reactivity outside of the core region of the test section for some state conditions (namely chemiluminescence in the annular region of the test section); effects that are not apparent at higher temperatures. However, while spatially distributed ignition behavior was observed, the IDTs based on conventional pressure and chemiluminescence were within the uncertainties of model and experimental values.

The results of the current work demonstrate NTC behavior is an important part of the dialog on interpretation of ignition data and additional studies are warranted. Measuring thermal boundary layers within experimental setups is a key step in quantifying the potential impact, as well as developing methods to quantify NTC effects on experimental data (e.g., possible corrections to temperatures assigned to experimentally measured IDT data or the use of two-zone and other higher-fidelity models to interpret experimental data). Adding spatial fidelity to the balloon model used here is a direction to improve the accuracy of the simulation; however, the two-zone model serves as a valuable means to consider limiting behavior, i.e., the maximum impact NTC behavior can have. Additional modeling of a more sensitive NTC fuel, like *n*-heptane, can provide additional quantitative understanding. Non-dimensionalizing system parameters to understand more broadly which fuels, conditions, and dimensions are likely to be convolved with NTC effects on boundary layers can be used to identify IDT data (past, present, and future) impacted by NTC behavior and revise experimental uncertainties accordingly. Ultimately, the results presented here show NTC chemistry and thermal boundary layers can play a measurable role on IDT measurements, and experimental data reported in the NTC region can be convolved with boundary layer effects that may be biasing experimental data.

4.6 References

[1] E.L. Petersen, M. Lamnaouer, J. de Vries, H. Curran, J. Simmie, M. Fikri, C. Schulz, G. Bourque, Discrepancies between shock tube and rapid compression machine ignition at low temperatures and high pressures, Shock Waves 26 (2009) 739 – 744.

[2] K.-Y. Lam, Z. Hong, D.F. Davidson, R.K. Hanson, Shock tube ignition delay time measurements in propane/O2/argon mixtures at near-constant-volume conditions, Proceedings of the Combustion Institute, Volume 33, Issue 1, 2011, Pages 251-258.

[3] Matthew F. Campbell, Shengkai Wang, David F. Davidson, Ronald K. Hanson, Shock tube study of normal heptane first-stage ignition near 3.5 atm, Combustion and Flame, Volume 198, 2018, Pages 376-392.

[4] J.F. Griffiths, D.J. Rose, M. Schreiber, J. Meyer, K.F. Knoche, Novel features of end-gas autoignition revealed by computational fluid dynamics, Combustion and Flame, Volume 91, Issue 2, 1992, Pages 209-212.

[5] Gaurav Mittal, Mandhapati P. Raju, Chih-Jen Sung, CFD modeling of two-stage ignition in a rapid compression machine: Assessment of zero-dimensional approach, Combustion and Flame, Volume 157, Issue 7, 2010, Pages 1316-1324.

[6] Jagannath Jayachandran, Fokion N. Egolfopoulos, Thermal and Ludwig–Soret diffusion effects on near-boundary ignition behavior of reacting mixtures, Proceedings of the Combustion Institute, Volume 36, Issue 1, 2017, Pages 1505-1511.

[7] Peng Dai, Zheng Chen, Shiyi Chen, Yiguang Ju, Numerical experiments on reaction front propagation in n-heptane/air mixture with temperature gradient, Proceedings of the Combustion Institute, Volume 35, Issue 3, 2015, Pages 3045-3052.

[8] D. Healy, D.M. Kalitan, C.J. Aul, E.L. Petersen, G. Bourque, H.J. Curran, Oxidation of C1 – C5 alkane quinternary natural gas mixtures at high pressures, Energy Fuels 24 (3) (2010) 1521 – 1528.

[9] Ponnuthurai Gokulakrishnan, Casey C. Fuller, Michael S. Klassen, Richard G. Joklik, Yash N. Kochar, Sarah N. Vaden, Timothy C. Lieuwen, Jerry M. Seitzman, Experiments and modeling of propane combustion with vitiation, Combustion and Flame, Volume 161, Issue 8, 2014, Pages 2038-2053.

[10] University of California at San Diego, Chemical-kinetic mechanisms for combustion applications, Mechanical and Aerospace Engineering (Combustion Research), University of California at San Diego, San Diego mechanism web page. http://combustion.ucsd.edu, 2021.

[11] Maximilien Cord, Benoit Husson, Juan Carlos Lizardo Huerta, Olivier Herbinet, Pierre-Alexandre Glaude, René Fournet, Baptiste Sirjean, Frédérique Battin-Leclerc, Manuel Ruiz-Lopez, Zhandong Wang, Mingfeng Xie, Zhanjun Cheng, and Fei Qi, Study of the Low Temperature Oxidation of Propane, The Journal of Physical Chemistry A 2012 116 (50), 12214-12228.

[12] Jiankun Shao, Rishav Choudhary, Adam J. Susa, David F. Davidson, Ronald K. Hanson, High-speed imaging of n-heptane ignition in a high-pressure shock tube, Proceedings of the Combustion Institute, Volume 38, Issue 1, 2021, Pages 911-918.

[13] Gregory E. Bogin, Eric Osecky, Matthew A. Ratcliff, Jon Luecke, Xin He, Bradley T. Zigler, and Anthony M. Dean, Ignition Quality Tester (IQT) Investigation of the Negative Temperature Coefficient Region of Alkane Autoignition, Energy & Fuels 2013 27 (3), 1632-1642.

[14] Peng Zhang, Weiqi Ji, Tanjin He, Xin He, Zhi Wang, Bin Yang, Chung K. Law, First-stage ignition delay in the negative temperature coefficient behavior: Experiment and simulation, Combustion and Flame, Volume 167, 2016, Pages 14-23.

[15] Moez Ben Houidi, Julien Sotton, Marc Bellenoue, Interpretation of auto-ignition delays from RCM in the presence of temperature heterogeneities: Impact on combustion regimes and negative temperature coefficient behavior, Fuel, Volume 186, 2016, Pages 476-495.

[16] Yunliang Qi, Yingdi Wang, Yanfei Li, Jianxin Wang, Xin He, Zhi Wang, Auto-ignition characteristics of end-gas in a rapid compression machine under super-knock conditions, Combustion and Flame, Volume 205, 2019, Pages 378-388.

[17] Wei Liu, Yunliang Qi, Ridong Zhang, Zhi Wang, Flame propagation and auto-ignition behavior of *iso*-octane across the negative temperature coefficient (NTC) region on a rapid compression machine, Combustion and Flame, Volume 235, 2022, 111688, https://doi.org/10.1016/j.combustflame.2021.111688.

[18] CHEMKIN-PRO 15112, Reaction Design: San Diego, 2011.

[19] David G. Goodwin, Raymond L. Speth, Harry K. Moffat, and Bryan W. Weber. Cantera: An object-oriented software toolkit for chemical kinetics, thermodynamics, and transport processes. https://www.cantera.org, 2021. Version 2.5.1.

[20] Haisheng Di, Xin He, Peng Zhang, Zhi Wang, Margaret S. Wooldridge, Chung K. Law, Cuiping Wang, Shijin Shuai, Jianxin Wang, Effects of buffer gas composition on low temperature ignition of *iso*-octane and n-heptane, Combustion and Flame, Volume 161, Issue 10, 2014, Pages 2531-2538.

[21] Yingdi Wang, Yunliang Qi, Wei Liu, Zhi Wang, Investigation of methanol ignition phenomena using a rapid compression machine, Combustion and Flame, Volume 211, 2020, Pages 147-157.

[22] M.T. Donovan, X. He, B.T. Zigler, T.R. Palmer, M.S. Wooldridge, A. Atreya, Demonstration of a free-piston rapid compression facility for the study of high temperature combustion phenomena, Combustion and Flame, Volume 137, Issue 3, 2004, Pages 351-365.

Chapter 5: Investigation of *iso*-Propyl Nitrate as a Detonation Improver

5.1 Introduction

Propagation of a combustion wave can occur at both subsonic speeds, known as deflagration, and supersonic speeds, known as detonation. The difference in velocity between a deflagration wave and a detonation wave is multiple orders of magnitude, with detonation wave velocities typically propagating in the range of 2 – 3 km/s compared with velocity rates on the order of m/s or cm/s typically observed for deflagration waves [1]. Additionally, the processes by which the waves propagate are fundamentally different. Deflagration is a result of heat and mass diffusion where the heat release from the reaction zone continuously preheats the reactants as they enter and are consumed in the reaction zone. In contrast, a detonation wave is characterized by a leading shock wave that is sustained by a reaction zone where the reaction rate due to heating from the leading shock is fast enough that both can travel at the same supersonic velocity.

Research into detonation phenomena is typically motivated by both an interest in the development of pulse detonation or rotating detonation engines (PDEs and RDEs), due to their higher theoretical efficiency relative to conventional combustion engines [2,3,4,5,6], as well as the need to identify the critical conditions necessary to initiate a detonation to ensure proper safety measures and risk-mitigation strategies are implemented when using and storing combustible materials [7,8,9,10].

As reviewed by Shepherd [8], the study of detonation has been of interest since its discovery by Berthelot and Vielle [11] and Mallard and Le Chatelier [12] in the late 19th century. Since then, a robust literature on detonation theory and experimental observations of detonation behavior continues to develop. One of the earliest descriptions of detonation wave behavior is the zero-dimensional Chapman – Jouguet (CJ) model [13,14] that proposed a theory for determining detonation wave velocity based on the thermodynamic properties of a mixture independent of wave structure without having to consider the kinetics occurring within the reaction zone. The classical CJ model was built upon by Zel'dovich [15], von Neumann [16], and Döring [17] (ZND) who proposed the one-dimensional model for detonation waves that includes a leading shock wave propagating at the detonation velocity followed by a reaction zone.

Further study revealed that detonation waves have a multi-dimensional structure that is non-uniform within the overall propagating wave structure itself, with the first evidence of this obtained by Campbell and Woodhead [18]. An example of this structure illustrated by Liu and Zhang [19] is provided in **Figure 5.1**. The movement of this structure along the length of a tube can be measured by placing foils coated in soot along the interior of the tube and allowing the detonation wave to pass over the foil, using a technique first applied by Denisov and Troshin [20]. As the detonation wave passes the foil, it leaves a two-dimensional imprint of the wave propagation on the soot foil that traces the position of the triple points of the detonation wave (the intersection between the incident shock, transverse shock, and Mach stem) along the front. The overall structure of the detonation wave is locally unsteady but somewhat periodic, allowing the wave to propagate at the stable detonation wave speed [10] despite the localized instabilities within the 3D structure itself. The width of the cells is known as the detonation cell size (λ), which is inversely related with the sensitivity of a mixture to detonation, i.e., a smaller cell size is associated with a mixture that will transition to detonation with a lower initiation energy. Measurement of the detonation cell size using soot foils is a well-established technique that has been widely used and reported [8,21,22]. An example of detonation cell structure measured using a soot foil is provided in **Figure 5.2**.

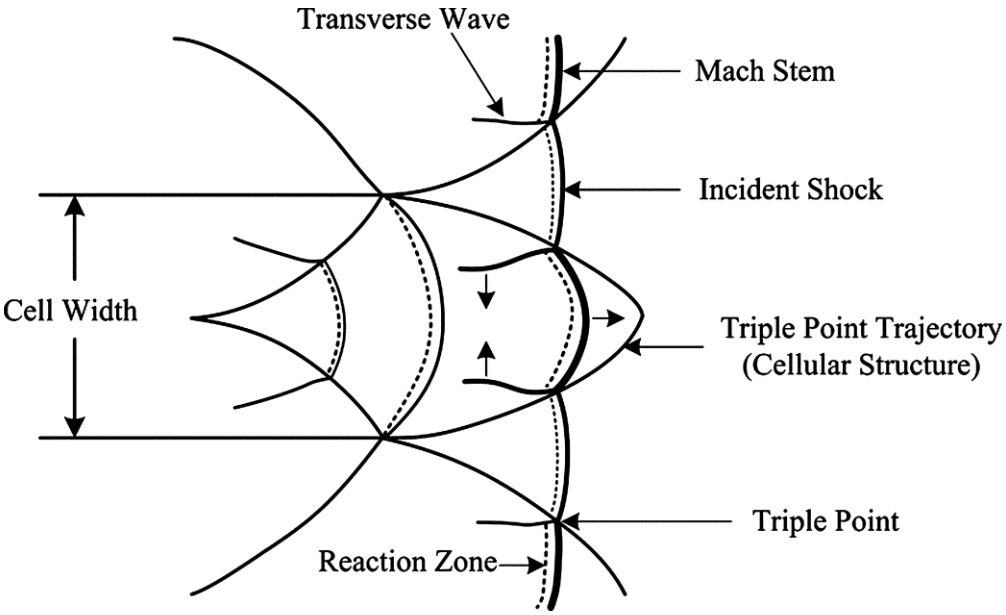

Figure 5.1: Example of the triple point trajectory of a detonation wave that forms detonation cell structure that can be measured experimentally using the soot-foil technique. Figure adapted from Liu and Zhang [19].

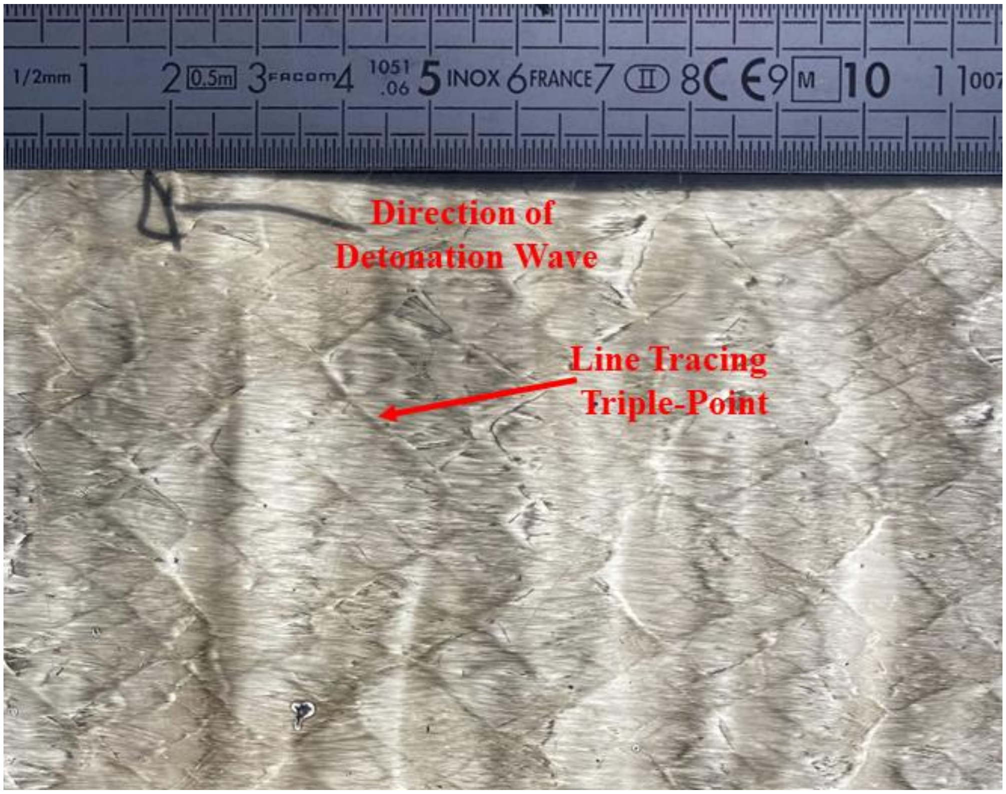

Figure 5.2: Example soot foil record of detonation cell structure measured in the present work of propane-oxygen mixture at an initial fill pressure of P_1 = 50 torr.

The characteristics of a detonation wave and the critical conditions required for transition to detonation of a mixture can be studied through both direct and indirect initiation of a detonation wave. Direct initiation of a detonation wave requires a large amount of energy that is typically provided by either an explosive or a strong shock wave that drives a shock-to-detonation transition (SDT) within the test gas, with a figure illustrating this process provided in **Figure 5.3**. Indirect initiation of a detonation wave requires much lower energy and can be accomplished using spark ignition [23]. The spark creates a flame that can be accelerated by inducing turbulence as the flame propagates until the overpressure waves generated by the turbulence lead to conditions where the mixture can detonate in a process known as deflagration-to-detonation transition (DDT), with a figure illustrating this process provided in **Figure 5.4**. Both SDT and DDT studies are important for identifying the critical conditions that will lead to mixture detonation and how changes in mixture composition impact the detonation sensitivity. Detonation sensitivity is quantified in this study by critical thermodynamic conditions (pressure and temperature) that lead to detonation in a shock tube.

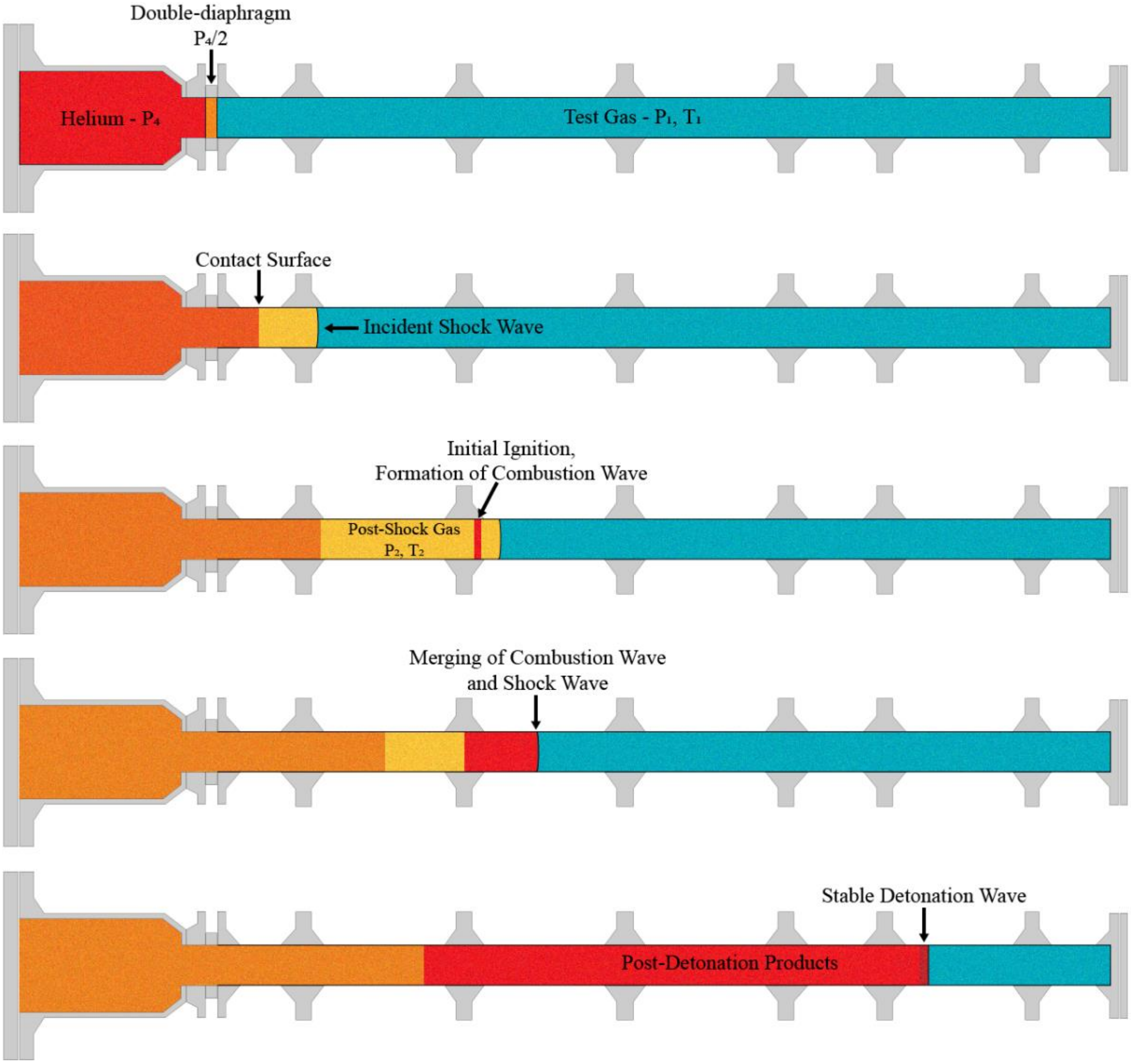

Figure 5.3: Typical shock-to-detonation transition (SDT) behavior observed in shock tube studies of detonation using a shock wave to initiate the detonation.

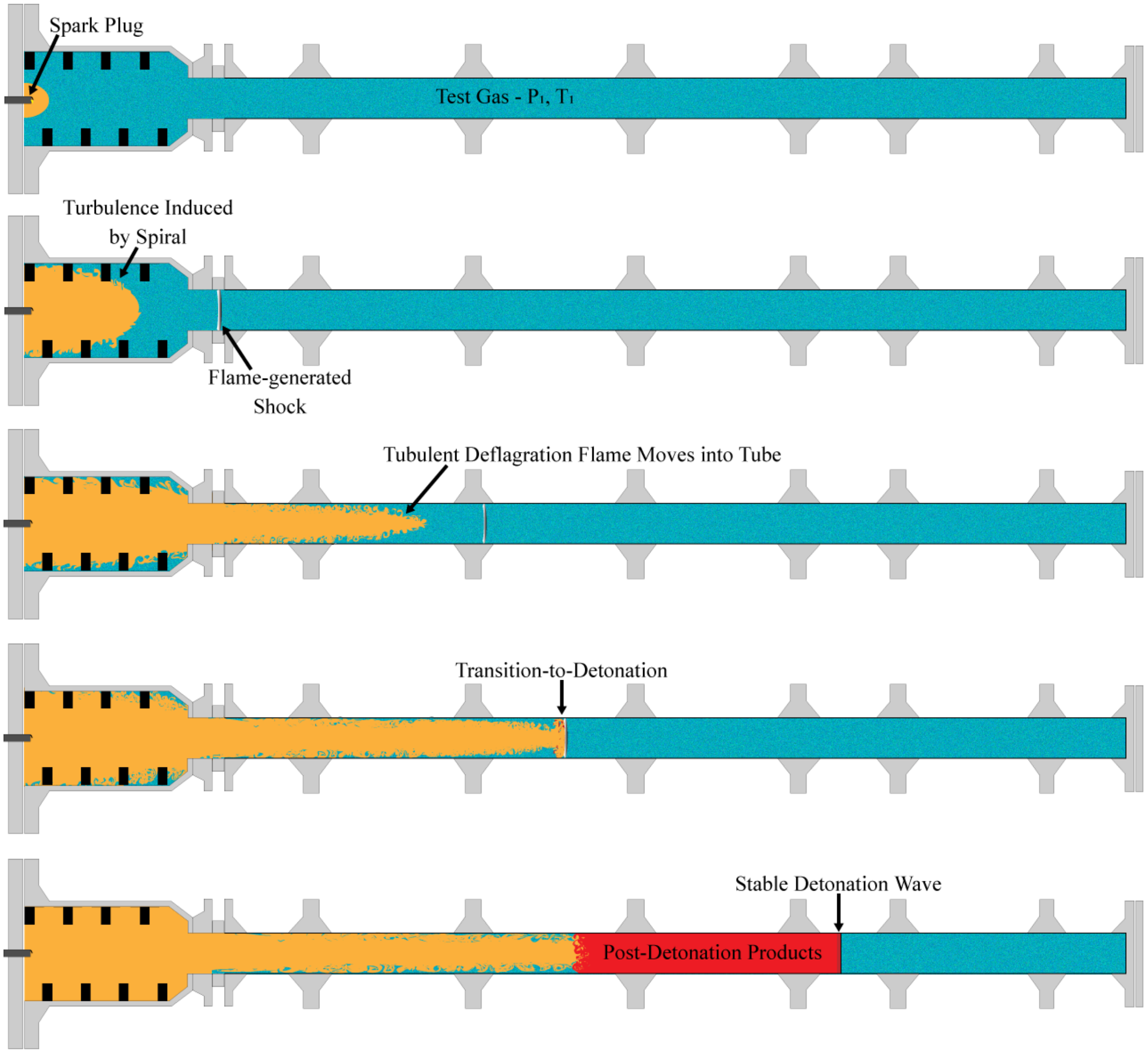

Figure 5.4: Typical deflagration-to-detonation transition (DDT) behavior observed in shock tube studies of detonation initiated by a spark plug and spiral to create a turbulent flame leading to detonation.

Key parameters can be measured in both SDT and DDT experiments to characterize the detonation wave and the mixture's sensitivity to detonation. The SDT measurements provide a highly controlled environment where a single shock wave is used to generate a detonation wave. By calculating the post-shock pressure and temperature conditions required for formation of a detonation wave, SDT experiments can identify the critical conditions necessary for a given mixture to transit to detonation. Conversely, in DDT experiments, the transition to detonation relies on turbulence and overpressure waves formed during flame propagation, making it much more difficult to identify the critical pressure and temperatures responsible for detonation. In this instance, the distance within the tube required for a mixture to transit to detonation, known as the run-up length, becomes the parameter of interest. Understanding how the run-up length changes in response to changes in mixture composition and initial conditions of the test gas is important to quantify since detonation engines typically operate through DDT as opposed to direct initiation phenomena that require much more initiation energy. Both SDT and DDT experiments can also be used to measure the cell size of a detonation wave to provide an additional metric of the detonation sensitivity of a mixture.

Detonation properties differ between fuel mixtures, with the present work focusing on the impact of adding 10% *iso*-propyl nitrate to stoichiometric mixtures of propane. Propane is an important component of natural gas blends, widely available, and easy to transport and store. For these reasons, the combustion behavior of propane has been widely studied experimentally spanning autoignition studies at a range of temperatures, pressures, and experimental facilities as discussed in **Chapter 3** [24] and **Chapter 4**. Beyond autoignition behavior, the detonation properties of propane are similar to those of JP-10 and kerosene that are suitable fuels for use in PDEs and RDEs, making it a useful model fuel for detonation studies [25,26,27,28,29,30]. Increasing the sensitivity of such fuels to detonation is an important research topic due to the limited space within a detonation engine for the transition to detonation to occur [2,31,32]. Methods for reduction in the run-up length and initiation energy required for a fuel mixture to transit to detonation are a major driver behind research into the impact of detonation sensitizers on fuel mixtures.

Despite the similarity of propane to typical PDE fuels and the existing literature on the detonation behavior of propane, there have been no previous studies exploring the impact of sensitizers on the detonation of propane. Alkyl nitrates have been used as monopropellants and fuel additives and have received a renewed interest as an alternative to the most used monopropellant, hydrazine, due to its high toxicity [33,34]. With the expectation that use of hydrazine will be heavily restricted in Europe in the coming years [35] the identification of "green" alternatives is an important technical challenge. Specifically, *iso*-propyl nitrate (IPN) is of interest due to its utilization prior to hydrazine, low toxicity, and low cost [36,37]. Only two previous studies on the detonation properties of IPN in a two-phase medium have been conducted [38,39], and the present work focuses on blends in the gas phase. Based on these factors, the goal of the present work is to determine whether IPN is an effective detonation sensitizer for propane mixtures and identify the critical conditions required for the initiation of detonation in propane-IPN fuel mixtures.

5.2 Methodology

5.2.1 Experimental Setup

The detonation tube at CNRS-ICARE, as shown in **Figure 5.5** and **Figure 5.6**, is a 7.8 cm diameter shock tube equipped with a series of shock detectors and PCB transducers at 20 points along the tube allowing for high temporal fidelity in measuring both wave propagation speed and changes in pressure over time. The tube can be configured for both SDT and DDT experiments. For SDT experiments, the tube is separated into a driver section filled with helium (high pressure denoted by P_4) and a driven section filled with the test gas of interest (low pressure denoted by P_1). The driver section has an internal diameter of 11.5 cm and a length of 165 cm, while the driven section has a length of 4.3 m for its 7.8 cm inner diameter. A removable double-diaphragm membrane, with the same 7.8 cm inner diameter and a length of 7.8 cm, separates the two sections to allow for the rapid depressurization of the driver gas to form a shock wave. In the DDT configuration, the membranes in the double diaphragm are removed and the entire tube is pressurized to the same initial pressure. A spark plug is inserted at the large end of the tube to initiate a flame while a spiral is inserted into the larger 11.5 cm diameter area to induce turbulence. Detonation cell size can be measured under both configurations using a 21 cm x 27 cm soot foil placed along the walls at the end of the tube. The remainder of this chapter will focus on the SDT configuration and results quantifying the impact of IPN on the critical conditions required for detonation.

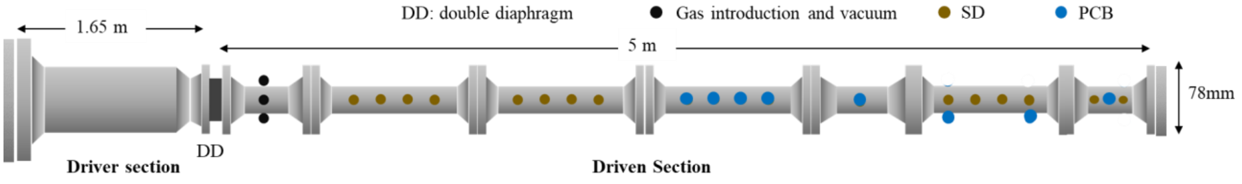

Figure 5.5: CNRS shock tube configuration for transition-to-detonation experiments. The shock tube has 20 locations where either shock detectors (SD), for high temporal fidelity detection of wave position, and PCB detectors (PCB 113B24), to measure changes in pressure.

Figure 5.6: Shock tube setup at CNRS-ICARE.

The test gas mixtures were prepared using two methods: mass flowmeters (to introduce the gas phase components directly) and the partial pressure method using a mixing tank when the addition of IPN was required. In the first method, three MKS Instruments Mass-Flo Controllers were used for propane, oxygen, and nitrogen individually. Each of the flowmeters was calibrated for its corresponding gas, and mixture composition was confirmed using a micro-gas chromatograph with three TCD detectors setup to analyze the species listed in **Table 5.1** below. The second method introduced the gas components and IPN using partial pressures method, ensuring that the composition of IPN was below 50% of its vapor pressure to avoid condensation within the reservoirs. These mixtures were allowed to sit overnight to ensure homogeneous mixture composition, which was also confirmed using the micro-GC. Pressures within the reservoir and shock tube were monitored with two MKS manometers for low pressure (0-100 torr, MKS Type 626AX12TBE) and higher pressures (100-1000 torr, MKS Type 626AX13TBE).

Table 5.1: Micro-GC columns and carrier gases used to analyze mixture composition of test gases used in each experiment.

GC Module	A	B	C
Carrier Gases	Argon	Helium	Helium
Columns	Molsieve	Molsieve	PoraPlot Q
Species Analyzed	H2, O2, N2	CH4, CO	COS, H2S, CO2, C2 and C3 species

5.2.2 Experimental Conditions

The experiments presented in this study used fuel mixtures of both propane (C_3H_8) and propane + 10% IPN ($iC_3H_7NO_3$) at stoichiometric conditions ($\phi = 1.0$) with N_2 dilution rates between 0 (O_2 only) and 1.5. A summary of the mixture compositions studied in the SDT configuration is provided in **Table 5.2**. The purities of the compounds used in each mixture are:

- Propane (Propane N25, Air Liquide, > 99.5%)
- *iso*-Propyl Nitrate (IPN, Sigma Aldrich, > 98%)
- Oxygen (ALPHAGAZ 1 O_2, Air Liquide, > 99.995%)
- Nitrogen (ALPHAGAZ 2 N_2, Air Liquide, > 99.9999%)

Table 5.2: Experimental mixture compositions for the detonation studies in the CNRS-ICARE detonation tube.

Mixture Number	Fuel	ϕ	N_2/O_2
1	C3H8	1.0	0
2	90% C3H8 + 10% IPN	1.0	0
3	C3H8	1.0	1.5
4	90% C3H8 + 10% IPN	1.0	1.5

SDT experiments for both propane and propane + 10% IPN were conducted at two initial fill pressures of P_1 = 50 torr and P_1 = 100 torr at ambient initial temperature (T_1 = ~294 K). The driver pressure, P_4, was varied from 2 to 19 bar to identify the critical conditions behind an incident shock wave (P_2 and T_2) required to initiate a detonation.

5.2.3 Computational Setup

The detonation velocity based on Chapman-Jouguet theory and the post-shock pressure and temperature conditions were calculated using Cosilab [40] as the equilibrium and post-shock condition solver. Shock wave velocity was measured directly using the wave position over time as measured by the shock and PCB detectors in the shock tube. This velocity was then used to calculate the P_2 and T_2 conditions behind the incident shock wave using mass, energy, and momentum conservation equations.

5.3 Discussion/Results

5.3.1 Wave Speed Measurements

The velocity of the wave propagation within the shock tube are calculated based on the wave position over time ($\Delta x/\Delta t$) observed by the SD and PCB detectors as the wave moves along the tube. The SD detectors are particularly well suited for high temporal fidelity measurements with low uncertainty due to their rise time of 0.4 μs and 0.75 mm^2 area. However, their high sensitivity makes them unsuitable for pressure measurements, which are captured using PCB detectors (PCB 113B24). An example of the typical sensor responses is illustrated in **Figure 5.7** showing the passage of a stable detonation wave down the length of the tube.

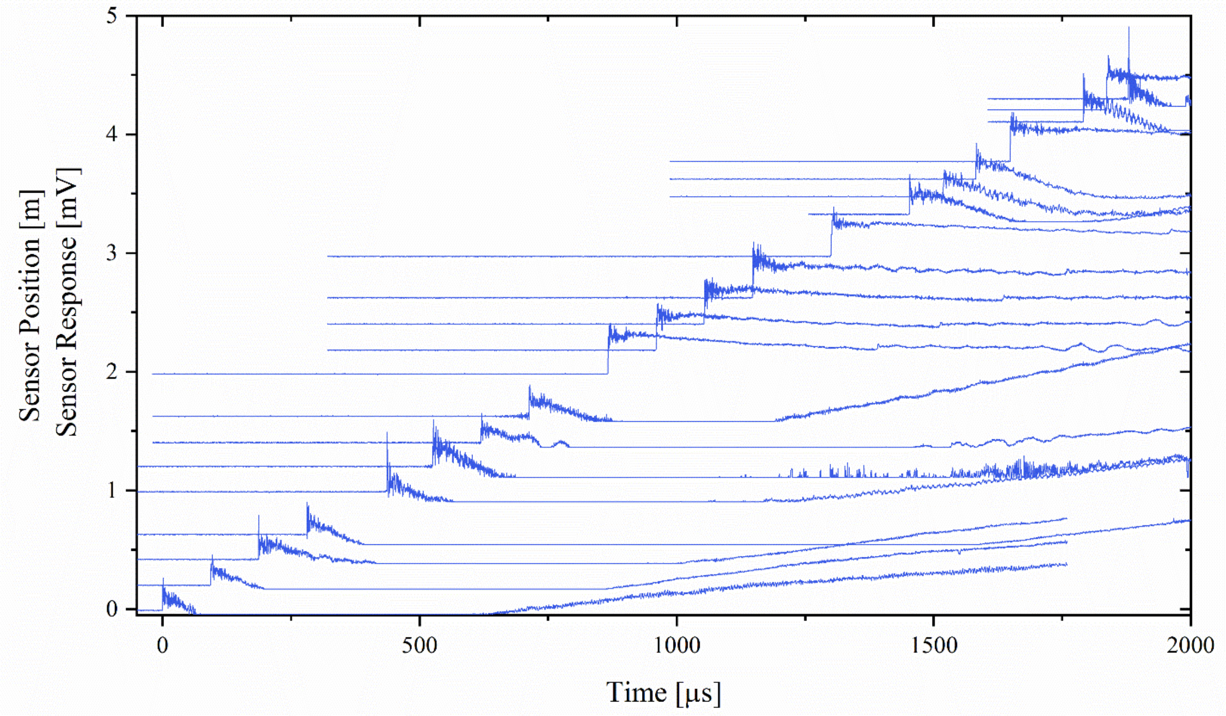

Figure 5.7: Sensor response to the passage of a stable detonation wave at each of the 20 SD/PCB detectors. The baseline sensor responses prior to the passage of the wave are located at the sensor position along the tube. The sharp increase in readout indicates the arrival of the wave, with the sensor response in mV relative to the baseline sensor position reading.

A trajectory fit of the measured velocities was calculated for each experiment, allowing for the assigning of a single wave velocity based on the speed of either the shock wave or detonation wave at the end of the tube to ensure consistency in measurement location between each experiment. The time of arrival for each wave is determined by the steep rise in electrical signals measured by the sensors. Based on this time and the position of the sensors, a polynomial fit is calculated to define the trajectory ($x_{detector} = f(t_{detector})$) and the velocity of the wave is deduced at each sensor position along the tube. A single velocity is assigned to each experiment based on the trajectory fit average across the location of the final three detectors in the shock tube to ensure a consistent point of comparison between experiments.

5.3.2 Shock-to-Detonation Transition

Each experiment is described as exhibiting one of three different types of behavior based on the observed velocities at each SD/PCB location along the shock tube:

- **Non-reactive shock wave (NRSW)** – no transition to detonation observed behind the incident shock, meaning the shock wave did not have enough energy to directly initiate a detonation.
- **Shock-to-detonation transition (SDT)** – a transition-to-detonation was observed after SD7, creating an overdriven detonation wave unable to stabilize within the full length of the shock tube. The overdriven detonation waves are typically hundreds of m/s faster than the predicted CJ detonation velocity.
- **Stable detonation** – a transition-to-detonation wave observed before SD7, creating a stable detonation wave within the full length of the shock tube. The stable detonation waves are slightly lower than the predicted CJ detonation velocity.

The conditions where these three behaviors are observed is dependent on the driver pressure, P_4, with P_4 values below the critical condition unable to initiate a detonation and P_4 values above the critical condition typically leading to either a stable or overdriven detonation wave. The impact that increasing P_4 has on the wave velocity of each experimental condition is shown in **Figure 5.8** and **Figure 5.9**. These results identify a clear pattern in response to increases in P_4, with the experiments at low P_4 values exhibiting non-reactive shock waves that increase in speed in response to increases in P_4 until the critical condition is reached. After the critical condition, there is a zone of uncertainty where all three behaviors (NRSW, SDT, detonation) may be observed until the strength of the shock wave reaches a point where it reliably produces either a stable detonation wave or a transition to detonation. The results for the experimentally observed stable detonation wave velocity measurements agree very well with those predicted from CJ calculations (D_{CJ}).

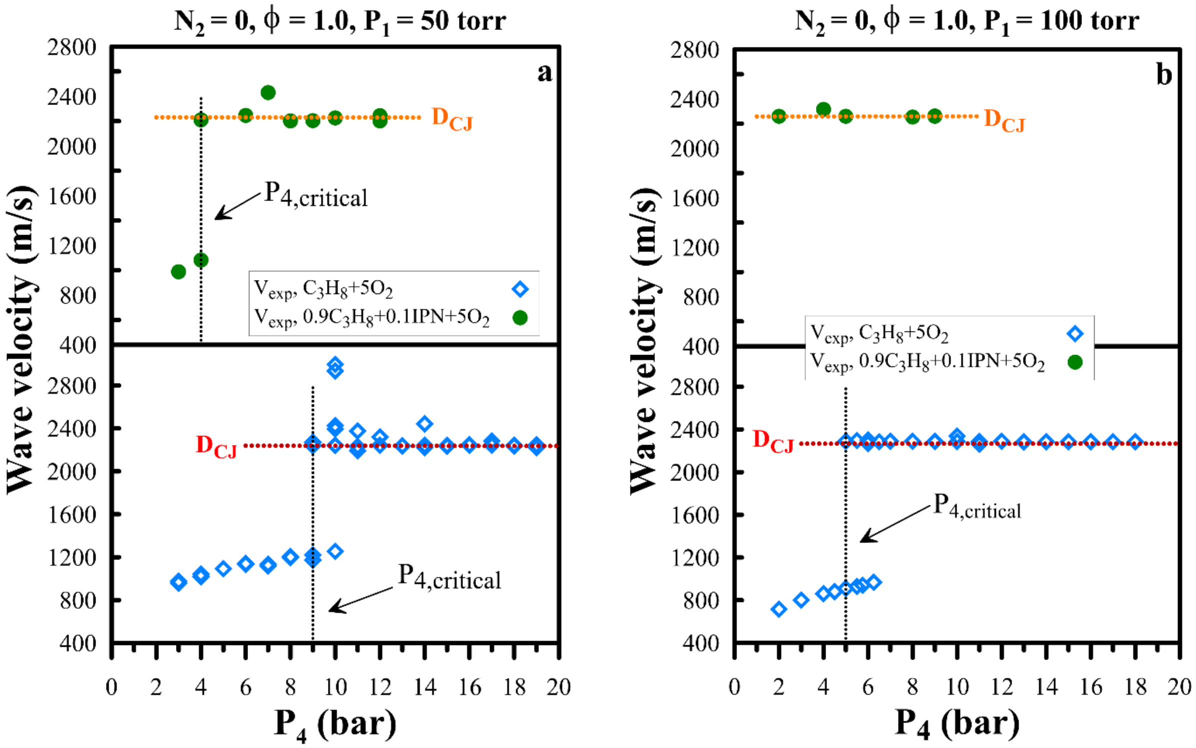

Figure 5.8: Change in wave velocity measurements in response to changes in driver pressure that show the impact of the addition of IPN on critical driver pressure, $P_{4,critical}$, for stoichiometric fuel + O_2 mixtures at (a) P_1 = 50 torr and (b) P_1 = 100 torr. Stable detonation velocity values above $P_{4,critical}$ also show good agreement with the theoretical CJ detonation velocity (D_{CJ}).

The addition of 10% IPN to the fuel mixture is shown to consistently decrease the critical conditions required to initiate a detonation across conditions both with and without additional nitrogen dilution. As shown in **Figure 5.8**, the minimum P_4 required to detonate ($P_{4,crit}$) for stoichiometric fuel + O_2 mixtures decreases from 9 bar to 4 bar at a fill pressure of P_1 = 50 torr and from 5 bar to below the minimum driver pressure of 2 bar at a fill pressure of P_1 = 100 torr. At the stoichiometric mixture conditions with a nitrogen dilution ratio (N_2/O_2) of 1.5, there is a less dramatic decrease, with the P_1 = 50 torr $P_{4,crit}$ decreasing from 10 bar to 8 bar with the addition of IPN and the P_1 = 100 torr condition decreasing from 11.5 bar to 9 bar. These results are summarized with the other key critical conditions in **Table 5.3**. A summary of the initial conditions and results for each experiment are provided in **Appendix D**.

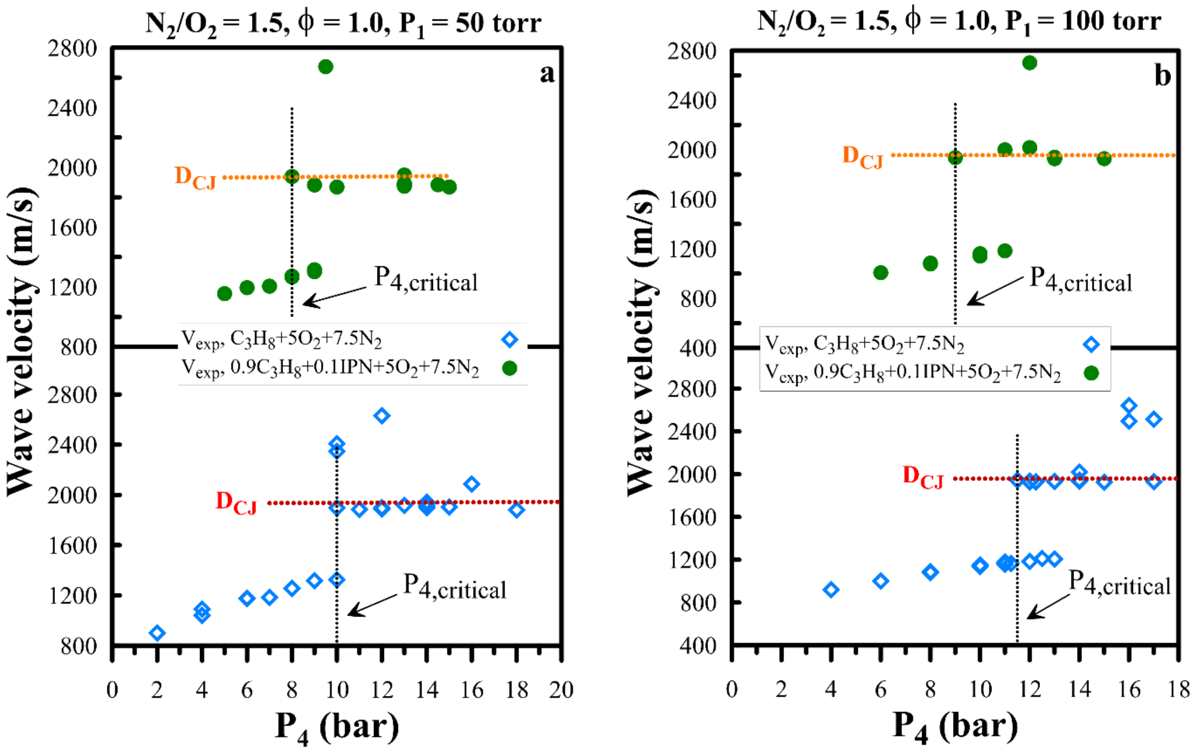

Figure 5.9: Change in wave velocity measurements in response to changes in driver pressure that show the impact of the addition of IPN on critical driver pressure, $P_{4,critical}$, for stoichiometric fuel + O_2 + N_2 mixtures at (a) P_1 = 50 torr and (b) P_1 = 100 torr with a nitrogen dilution rate $N_2/O_2 = 1.5$. Stable detonation velocity values above $P_{4,critical}$ also show good agreement with the theoretical CJ detonation velocity (D_{CJ}).

While change in the $P_{4,crit}$ value is a useful indicator of change in a mixture's sensitivity to detonation, it does quantify the specific pressure and temperature conditions necessary for that transition to occur. Additionally, near the critical region, differences in the membrane bursting process between experiments can impact the strength of the incident shock wave leading to higher uncertainties in the definition of the $P_{4,crit}$ region. To calculate the P and T values behind the incident shock, it is necessary to utilize gas dynamic equations to determine the pressure and temperature conditions behind the incident shock, referred to as P_2 and T_2, and are based on the velocity of the incident shock wave at the critical condition prior to its transition to detonation.

Similar to what is observed in the decrease of $P_{4,crit}$, the minimum pressure and temperature conditions behind the incident shock ($P_{2,crit}$ and $T_{2,crit}$) are also reduced in response to the addition of IPN, with these results summarized in **Table 5.3**. For the stoichiometric fuel/O_2 mixtures, the addition of IPN decreases $P_{2,crit}$ by ~0.2 bar and $T_{2,crit}$ by ~80 K at P_1 = 50 torr, with $P_{2,crit}$ and $T_{2,crit}$ results at P_1 = 100 torr unavailable since the critical conditions occurred below the minimum P_4

possible in the experimental setup. At the stoichiometric mixture conditions where $N_2/O_2 = 1.5$, the addition of IPN shows a less dramatic decrease in $P_{2,crit}$ of ~0.1 bar and $T_{2,crit}$ by ~50 K at P_1 = 50 torr, with $P_{2,crit}$ decreasing by ~0.1 bar and $T_{2,crit}$ by ~40 K when P1 = 100 torr.

Table 5.3: Comparison of the critical conditions for transition-to-detonation for C_3H_8 and C_3H_8 + IPN fuel mixtures for nitrogen dilution (N_2/O_2) and initial fill conditions (P_1).

Fuel	N_2/O_2	P_1 (torr)	$P_{4,critical}$ (bar)	$P_{2,critical}$ (bar)	$T_{2,critical}$ (K)
C_3H_8	0	50	9	1.22	806.2
90% C_3H_8 + 10% IPN			4	1.02	727.6
C_3H_8	0	100	5	1.38	610.6
90% C_3H_8 + 10% IPN			Transition point below minimum P_4		
C_3H_8	1.5	50	10	1.31	972.6
90% C_3H_8 + 10% IPN			8	1.22	924.2
C_3H_8	1.5	100	11.5	2.00	832.2
90% C_3H_8 + 10% IPN			9	1.88	794.5

5.3.3 Detonation Cell Size

The detonation cell structure was measured using a soot-covered foil placed along the walls at the end of the shock tube. The cell size (λ) is inversely related to the sensitivity of a mixture to detonation, with smaller cell sizes indicating that a mixture has a higher sensitivity to detonation. Cell sizes provide a point of comparison between mixtures using various fuels, mixture compositions, and initial conditions. Unfortunately, cell size and resolution for the $N_2/O_2 = 1.5$ conditions presented in this work were too large to be consistently measured within the shock tube, yielding inconclusive results that were not statistically significant enough to assign a cell size value. Therefore, the cell size results presented are only for the fuel/O_2 experiments, which provided appropriate resolution to assign cell size values with appropriate uncertainties.

An example of a typical soot foil measurement for detonation cell size is shown in **Figure 5.10**. The structure from cell-to-cell is somewhat irregular, meaning there is variation in the cell size between cells as the wave passes over the soot foil. This irregularity makes the ability to measure many cells important to assigning a meaningful λ value for each mixture condition. In this case, over 150 cells were measured for each cell size assigned to the four mixture conditions reported in the present study with results reported as the cell size and associated standard deviation at each condition.

Figure 5.10: Example of typical soot foil results used to measure detonation cell size.

At certain conditions, the transition to detonation was also captured in the region where the soot foil was located. An example is shown in **Figure 5.11** where the transition to detonation is indicated by a region of small detonation cells spreading after a region of streamlines where no cellular structure is observed. These initial cells have a significantly smaller λ than those recorded for a stable detonation wave, despite having the same initial mixture conditions. This discrepancy is due to the overdriven nature of the detonation wave immediately following transition to detonation, with a much higher wave velocity than that predicted by D_{CJ}. Given additional time for the wave to propagate, the wave would relax to a velocity slightly below D_{CJ} (as observed under the stable detonation conditions for the same mixture) and yield larger cell sizes accordingly.

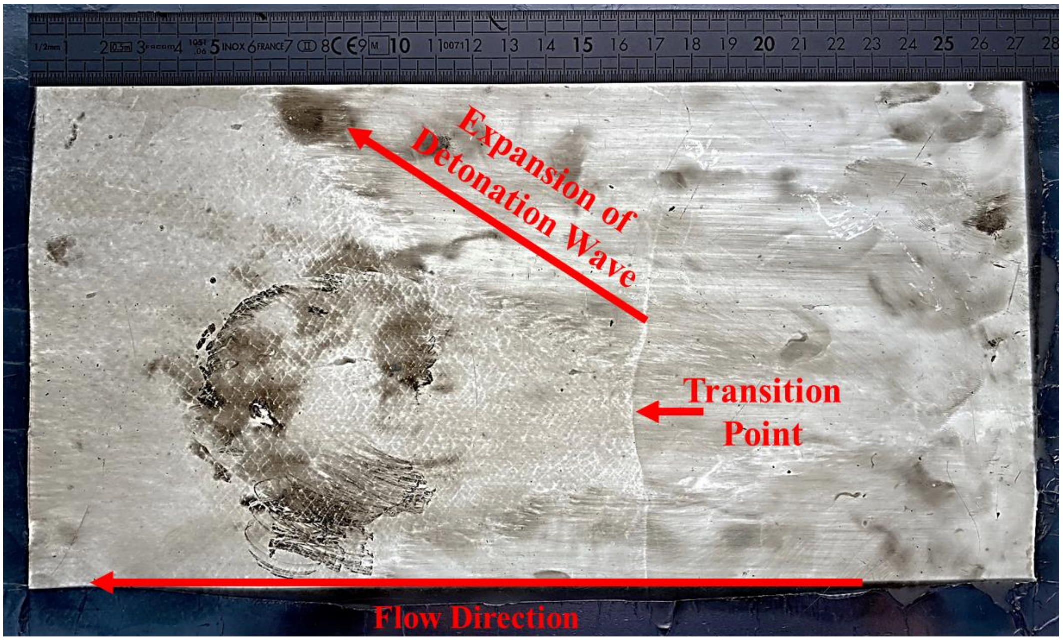

Figure 5.11: Transition to detonation captured by the soot foil showing the transition point and the expansion of the detonation wave within the tube. The change in cell size structure is also of interest, with the detonation cells expanding slightly as the wave forms due to the initially overdriven detonation wave beginning to relax to the D_{CJ} condition.

Figure 5.12 shows how average cell size was impacted by the addition of IPN to the stoichiometric C3H8/O2 mixtures, with the results also provided in

Table 5.4. There is a consistent decrease in the cell size at both P_1 = 50 torr and P_1 = 100 torr in response to the addition of 10% IPN. The average cell size decreased by 2.31 mm at P_1 = 50 torr and 1.1 mm at P_1 = 100 torr. The smaller decrease in the higher-pressure condition is expected due to the smaller initial average cell size. It is important to note that the standard deviation in these measurements reported does lead to overlap in assigned λ values for mixtures with and without IPN. Due to the irregularity of the cells, overlap in measured cell size is expected between the 0% IPN and 10% IPN conditions. The decrease in average cell size indicates that the overall distribution of these values has shifted to a lower value indicating an increase in the detonation sensitivity of these mixtures. (Note that the uncertainty bars shown in the figure are indicative of standard deviation within the distribution and are not representative of experimental uncertainty.)

Table 5.4: Impact of the addition of 10% IPN to the fuel mixture on the detonation cell size at P_1 = 50 torr and P_1 = 100 torr with associated standard deviations in cell size measurement.

Fuel	P_1 (torr)	Cell Size, λ (mm)	σ (mm)
C_3H_8	50	11.6	±3.13
90% C_3H_8 + 10% IPN		9.29	±2.31
C_3H_8	100	4.83	±1.32
90% C_3H_8 + 10% IPN		3.73	±0.82

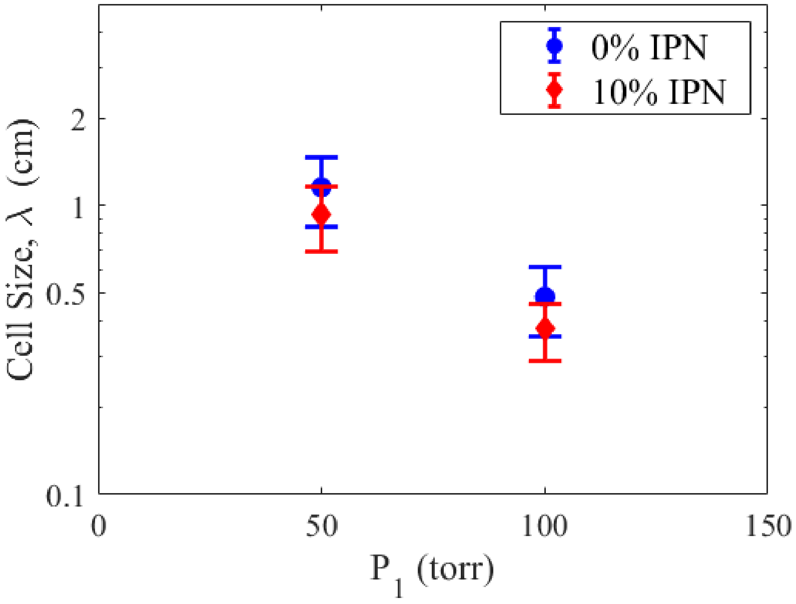

Figure 5.12: Impact of the addition of 10% IPN on cell size for P_1 = 50 torr and P_1 = 100 torr for stoichiometric $C_3H_8 + O_2$ mixtures.

5.4 Conclusions and Future Work

Detonation behavior is an exciting research area with much room to grow in its scope, from the increasing research into the development of detonation engines to the kinetics research into identifying viable fuels and sensitizers for engines and understanding their fundamental kinetics. This work indicates that IPN shows promise as one of these potential sensitizers. IPN at 10% fuel concentration increased the sensitivity of propane mixtures to detonation, and its use as an additive resulted in a decrease in $P_{4,crit}$, $P_{2,crit}$, and $T_{2,crit}$ necessary for each mixture to initiate a detonation. In addition, the increase of IPN also led to a decrease in the average cell size observed under SDT experiments. The conditions necessary for the onset of detonation behind a shock wave have been identified for both P_1 = 50 torr and P_1 = 100 torr for each of the mixtures of interest.

Future work is expected to involve a kinetic analysis of the role of IPN in increasing the sensitivity to detonation of propane, specifically for the autoignition kinetics occurring behind the incident shock wave that led to the characteristic coupling between shock wave and reaction zone that comprise a detonation wave. Beyond this, DDT experiments for these mixture conditions are currently being conducted to supplement the existing work to provide a better understanding of the impact of IPN as an additive using a transition process that is more common in real-world applications.

5.5 References

[1] Bo Zhang, Hong Liu, Bingjian Yan, Hoi Dick Ng, Experimental study of detonation limits in methane-oxygen mixtures: Determining tube scale and initial pressure effects, Fuel, Volume 259, 2020, 116220.

[2] G.D. Roy, S.M. Frolov, A.A. Borisov, D.W. Netzer, Pulse detonation propulsion: challenges, current status, and future perspective, Progress in Energy and Combustion Science, Volume 30, Issue 6, 2004, Pages 545-672.

[3] Kailasanath, K. (2009). Research on Pulse Detonation Combustion Systems: A Status Report. 47th AIAA Aerospace Sciences Meeting including the New Horizons Forum and Aerospace Exposition. 10.2514/6.2009-631.

[4] Fedor A. Bykovskii, Sergey A. Zhdan, and Evgenii F. Vedernikov, Continuous Spin Detonations, Journal of Propulsion and Power 2006 22:6, 1204-1216

[5] Frank K. Lu and Eric M. Braun, Rotating Detonation Wave Propulsion: Experimental Challenges, Modeling, and Engine Concepts, Journal of Propulsion and Power 2014 30:5, 1125-1142.

[6] Piotr Wolański, Detonative propulsion, Proceedings of the Combustion Institute, Volume 34, Issue 1, 2013, Pages 125-158.

[7] N. Chaumeix, B. Imbert, L. Catoire & C. -E. Paillard (2014) The Onset of Detonation Behind Shock Waves of Moderate Intensity in Gas Phase, Combustion Science and Technology, 186:4-5, 607-620.

[8] J.E. Shepherd, Detonation in gases, Proceedings of the Combustion Institute, Volume 32, Issue 1, 2009, Pages 83-98.

[9] S.B. Dorofeev, V.P. Sidorov, A.E. Dvoinishnikov, W. Breitung, Deflagration to detonation transition in large confined volume of lean hydrogen-air mixtures, Combustion and Flame, Volume 104, Issues 1–2, 1996, Pages 95-110.

[10] A. A. Vasil'ev, Cell Size as the Main Geometric Parameter of a Multifront Detonation Wave Journal of Propulsion and Power 2006 22:6, 1245-1260.

[11] M. Bertherlot, P. Vielle, Ann. de Phys. et Chim., 28 (v) (1881), p. 289.

[12] E. Mallard, H.L. Le Chatelier, Annales des Mines, 8 (iv) (1881), pp. 274-618.

[13] D.L. Chapman, “On the Rate of Explosion of Gases,” Phil. Mag., Vol. 47, pp. 90 – 103, 1899.

[14] E. Jouguet, J. Mathematique, p. 347, 1905; p. 6, 1906.

[15] Y.B. Zel'dovich, The Theory of the Propagation of Detonation in Gaseous Systems, Expt. Theor. Phys. S.S.S.R., Vol. 10, p. 542, 1940; Translation, NACA TM 1261, 1950.

[16] J. von Neumann, Theory of Detonation Waves, Prof. Report No. 238, April 1942; OSRD Report No. 549, 1942.

[17] W. Döring, On the detonation process in gases, Ann. Phys. Lpz., Vol. 43, pp. 421 – 436, 1943.

[18] C. Campbell and D.W. Woodhead, J. Chem. Soc., p. 3010, 1926; p. 1572, 1927.

[19] Lijuan Liu, Qi Zhang, Numerical study of cellular structure in detonation of a stoichiometric mixture of vapor JP-10 in air using a quasi-detailed chemical kinetic model, Aerospace Science and Technology, Volume 91, 2019, Pages 669-678.

[20] Y.H. Denisov and Y.K. Troshin, Dokl. Akad. Sci. S.S.S.R., Vol. 125, p. 110, 1959; translation, Phys. Chem. Sect., Vol. 125, p. 217, 1960.

[21] K. Kuo, Principles of Combustion, John Wiley and Sons, Inc., New York, 2005.

[22] Rémy Mével, Dmitry Davidenko, Fabien Lafosse, Nabiha Chaumeix, Gabrielle Dupré, Claude-Étienne Paillard, Joseph E. Shepherd, Detonation in hydrogen–nitrous oxide–diluent mixtures: An experimental and numerical study, Combustion and Flame, Volume 162, Issue 5, 2015, Pages 1638-1649.

[23] P.F. Pinard, A.J. Higgins, J.H.S. Lee, The effects of NO2 addition on deflagration-to-detonation transition, Combustion and Flame, Volume 136, Issues 1–2, 2004, Pages 146-154.

[24] Miles A. Burnett, Margaret S. Wooldridge, An experimental investigation of flame and autoignition behavior of propane, Combustion and Flame, Volume 224, 2021, Pages 24-32.

[25] O.G. Penyazkov, K.A. Ragotner, A.J. Dean, B. Varatharajan, Autoignition of propane–air mixtures behind reflected shock waves, Proceedings of the Combustion Institute, Volume 30, Issue 2, 2005, Pages 1941-1947.

[26] R. Akbar, P.A. Thibault, P.O. Harris, L.-S. Lussier, F. Zhang, S.B. Murray, in: 36th AIAA/ASME/SAE/ASEE Joint Propulsion Conference and Exhibit Proceedings, Huntsville, AL, 2000.

[27] David C. Bull, John E. Elsworth, Geoffrey Hooper, Initiation of spherical detonation in hydrocarbon/air mixtures, Acta Astronautica, Volume 5, Issues 11–12, 1978, Pages 997-1008.

[28] C.J Brown, G.O Thomas, Experimental studies of shock-induced ignition and transition to detonation in ethylene and propane mixtures, Combustion and Flame, Volume 117, Issue 4, 1999, Pages 861-870.

[29] Frolov, S.M., Smetanyuk, V.A., Shamshin, I.O. et al. Cyclic Detonation of the Ternary Gas Mixture Propane–Oxygen–Steam for Producing Highly Superheated Steam. Dokl Phys Chem 490, 14–17 (2020).

[30] M. Silvestrini, B. Genova, G. Parisi, F.J. Leon Trujillo,

Flame acceleration and DDT run-up distance for smooth and obstacles filled tubes, Journal of Loss Prevention in the Process Industries, Volume 21, Issue 5, 2008, Pages 555-562.

[31] Harris PG, Farinaccio R, Stowe R, Higgins RA, Thibault JP, Laviolette J. The effect of DDT distance on impulse in a detonation tube. 37th Joint Propulsion Conference (2001), paper 3467.

[32] Jianzhong Li, Penggang Zhang, Li Yuan, Zhenhua Pan, Yuejin Zhu, Flame propagation and detonation initiation distance of ethylene/oxygen in narrow gap, Applied Thermal Engineering, Volume 110, 2017, Pages 1274-1282.

[33] Angela Mbugua, Aman Satija, Robert P. Lucht, Sally Bane, Ignition and combustion characterization of single nitromethane and isopropyl nitrate monopropellant droplets under high-temperature and quasi-steady conditions, Combustion and Flame, Volume 212, 2020, Pages 295-308.

[34] Mark E. Fuller and C. Franklin Goldsmith, Shock Tube Laser Schlieren Study of the Pyrolysis of Isopropyl Nitrate, The Journal of Physical Chemistry A 2019 123 (28), 5866-5876.

[35] Naumann, Clemens ; Kick, Thomas ; Methling, Torsten ; Braun-Unkhoff, Marina ; Riedel, Uwe, ETHENE/NITROUS OXIDE MIXTURES AS GREEN PROPELLANT TO SUBSTITUTE HYDRAZINE: REACTION MECHANISM VALIDATION, International journal of energetic materials and chemical propulsion, vol. 19, no. 1. pp. 65–71.

[36] Anirudha Ambekar, Sheshadri Sreedhara, Arindrajit Chowdhury, Burn rate characterization of *iso*-propyl nitrate – A neglected monopropellant, Combustion and Flame, Volume 162, Issue 3, 2015, Pages 836-845.

[37] Umakant Swami, Anirudha Ambekar, Dhananjay Gondge, Sheshadri Sreedhara, Arindrajit Chowdhury, Burn rate characterization of desensitized isopropyl nitrate blends, Combustion and Flame, Volume 190, 2018, Pages 454-466.

[38] Liu, Q., Bai, C., Dai, W. et al. Deflagration-to-detonation transition in isopropyl nitrate mist/air mixtures. Combust Explos Shock Waves 47, 448 (2011).

[39] Zhang, F., Akbar, R., Thibault, P. et al. Effects of nitrates on hydrocarbon-air flames and detonations. Shock Waves 10, 457–466 (2001).

[40] COSILAB, The combustion simulation laboratory, version 4.1.2, Rotexo GmbH & Co. KG, Haan, Germany (2018)

Chapter 6: Conclusions and Recommendations for Future Work

6.1 Conclusions

Providing experimental data on fundamental combustion behavior is important to accurately quantify the reaction behavior of diverse fuels, to validate current understanding of chemical kinetics, and to develop new theory. Understanding and addressing the existing knowledge gaps in the mechanisms and methods used to predict fuel behavior is crucial to the design of applications that utilize alternative fuels and advanced combustion strategies. The work in this dissertation provides high-fidelity benchmark data for significant fuels and additives and identifies discrepancies in fundamental understanding, especially at low-temperature conditions.

iso-Propanol has been identified as a promising alternative sustainable fuel and is an important reference alcohol. The pyrolysis study of *iso*-propanol is the first to quantify major stable intermediate species formed at the temperatures and pressures considered. Pyrolysis studies are crucial to understanding combustion behavior, since thermal decomposition reactions are one of the classes of reactions that initiate the combustion process, and speciation data provide the most difficult test case for elementary reaction rates. While the model and experimental data generally showed good agreement (e.g., typically within a factor of 4), important discrepancies of greater than an order of magnitude were identified including the overprediction of *iso*-propanol consumption at the highest temperature T = 1193 K condition and the underprediction of ethane production at the lowest temperature T = 965 K condition. Additional modeling and sensitivity analyses identified the most important reactions for the conditions studied were 2-C_3H_7OH (+M) and H-atom abstraction reactions from 2-C_3H_7OH by key radicals, OH and CH_3. While the speciation data provide valuable new data on the overall reaction pathways, the discrepancies between the model predications and the experimental data indicate additional studies to quantify the overall reaction rates and branching fractions of these reactions are necessary to improve quantitative accuracy.

Two studies on propane ignition at low-temperature combustion conditions identified sources of scatter observed in experimental facilities due to complex ignition behavior associated with autoignition regimes. Two categories of thermal gradients, local temperature differences and thermal boundary layers spanning the negative temperature coefficient (NTC) region, were evaluated in detail using experiments, computational methods, and theory. The autoignition regime data demonstrated that ignition delay time (IDT) measurements in regions where mixed ignition was observed were systematically faster than those predicted by models based predominantly on elementary reaction chemistry with limited to no spatial effects. The results added to the growing body of data showing that mixed ignition behavior is an explanation for some of the higher rates of scatter observed in the low-temperature region for propane and other fuels. Additionally, the results provided additional evidence of the Sankaran Criterion's utility as a tool for use in experimental design by providing *a priori* predictions of observed ignition behavior and for *post-mortem* interpretation of experimental and computational data. The IDT and high-speed imaging results on the impact of thermal boundary layers on ignition of NTC fuels suggest the change in temperature near the walls of unheated reaction chambers may impact ignition characteristics. While the magnitude of the impact NTC behavior can have compared with model predictions could not be quantified, the study clearly showed the complex interactions of NTC behavior and thermal boundary layers with mixing. Such convolution and interactions are not currently considered when interpreting IDT data in the NTC region. Systematic and/or random bias are likely being introduced to IDT data in the NTC region, and consequently, impacting reaction mechanism development to some extent. The magnitude of the effects on reaction chemistry is an important subject for future work and improved understanding.

Measurements of the detonation wave speed, cell size, and critical conditions provided the first experimental evidence of *iso*-propyl nitrate (IPN) as a detonation sensitizer for propane in the gas phase. The addition of 10% IPN led to a decrease in the critical conditions necessary for detonation of propane-oxygen mixtures with and without additional nitrogen dilution at $P = 50$ and 100 torr. The results indicate that IPN is a promising detonation sensitizer for applications relevant to pulse and rotating detonation engines.

6.2 Recommendations for Future Work

The data presented in this work provide information useful to improving fundamental understanding of combustion chemistry and identify knowledge gaps that should be the focus of future studies. Discrepancies between the speciation data and model predictions for *iso*-propanol suggest some existing elementary reaction rates may need revision to account for the overprediction of *iso*-propanol consumption at intermediate temperature (T = 1193 K) and the underprediction of ethane production at low temperatures (T = 965 K). Several novel and interesting approaches utilizing machine learning for mechanism optimization have been presented recently, and their application in optimizing rate coefficients based on speciation data is an area that may help identify the classes and specific reactions in need of higher fidelity consideration.

Inhomogeneous ignition characteristics were identified as a source of uncertainty in lower temperature ignition studies for propane, and additional work validating the Sankaran Criterion for fuels beyond those previously studied would prove useful in confirming its effectiveness as an *a priori* method of autoignition, especially for the most common fuels of interest in low temperature combustion applications. The combustion of NTC fuels at low temperatures and within the NTC region remains a complex phenomenon requiring additional experimental and modeling studies to fully understand its impact on scatter in reported ignition delay time data. A logical next step in an NTC study would be increasing or decreasing the thermal boundary layer by cooling or heating the chamber walls prior to the experiment and/or changing the size of the test section and quantifying how the ignition behavior changes in response to these changing properties of the thermal boundary layers. This would provide useful experimental data on the magnitude of the impact of thermal boundary layers on NTC fuel ignition studies.

Finally, additional work on IPN as a detonation sensitizer is in progress at the Centre National de la Recherche Scientifique – Institut de Combustion, Aérothermique, Réactivité et Environnement (CNRS-ICARE) with studies on deflagration-to-detonation transition (DDT) behavior underway following the identification of the critical conditions required to initiate a detonation in the SDT configuration. The results will provide more data on detonation cell size for a range of initial fill pressure conditions and show how the addition of IPN impacts the run-up length required for DDT to occur. Kinetic analysis on how IPN sensitizes propane to detonation is underway, specifically on how the two fuels interact when the critical conditions for detonation fall within the NTC region for propane. A comparison study on the impact of IPN on the detonation properties of a non-NTC fuel would provide useful kinetic data on the role of NTC behavior in transition to detonation. As such, studies on the impact of IPN on propylene (C_3H_6) are currently being explored. Beyond this, further studies on how detonation behavior responds to changes in concentration of IPN in the fuel mixture and changes to the equivalence ratio are recommended, and further comparison of IPN ignition characteristics with other detonation enhancing components would be of interest to understand chemical and gas dynamic interactions

Appendices

Appendix A: Supplemental Material for Chapter 2

Table A.1: Gas chromatograph program conditions used to detect small hydrocarbons produced during *iso*-propanol pyrolysis.

Column	**Length (m)**	**ID (mm)**	**Carrier Gas**	**Temperature Program**	**Detector**
CP-Porabond Q	25	0.53	He (31 cm/s)	40°C (2 min) ↑ 6°C/min to 160°C (hold 3 min)	FID

Table A.2: Gas calibrations and associated uncertainties used to determine species concentration in *iso*-propanol pyrolysis gas sampling experiments conducted in 2019.

Species	**ppm/mV^2**	**Uncertainty (%)**
Methane	14.911	±7
Ethene	7.777	±5
Ethane	7.616	±5
Propene	5.015	±20
Acetaldehyde	13.687	±10
Acetone	7.278	±10
iso-Propanol	5.369	±10

Table A.3: Gas calibrations and associated uncertainties used to determine species concentration in *iso*-propanol pyrolysis gas sampling experiments conducted in 2020. (These calibrations were updated following a prolonged shutdown due to COVID-19.)

Species	**ppm/mV^2**	**Uncertainty (%)**
Methane	14.953	±10
Ethene	7.223	±10
Ethane	7.961	±15
Propene	5.015	±20
Acetaldehyde	13.472	±10
Acetone	5.599	±25
iso-Propanol	5.056	±25

Table A.4: Gas calibrations and associated uncertainties based on peak height instead of integrated area due to overlap between the peaks associated with ethene and acetylene at high temperature conditions.

Species	ppm/mV	Uncertainty (%)
Ethene	14.407	±10
Acetylene	7.150	±15

Table A.5: List of the chemicals used for study of *iso*-propanol pyrolysis experiments and as reference compounds for GC calibration.

Chemical	Formula	Source	Purity
iso-Propanol	2-C_3H_7OH	Sigma-Aldrich	>99.9%
Nitrogen	N_2	PurityPlus	>99.999%
Argon	Ar	PurityPlus	>99.999%
Acetone	CH_3COCH_3	Sigma-Aldrich	>99.9%
Acetaldehyde	CH_3CHO	Alfa Aesar	>99.0%
Propene	C_3H_6	Sigma-Aldrich	>99.0%
Ethane	C_2H_6	PurityPlus	>99.0%
Ethene	C_2H_4	PurityPlus	>99.90%
Acetylene	C_2H_2	PurityPlus	>99.6%
Methane	CH_4	PurityPlus	>99.99%

Table A.6: Test gas mixture composition (mole fraction) results for all *iso*-propanol pyrolysis experiments conducted in the UM-RCF.

Run	2-C3H7OH (%)	Ar (%)	N2 (%)
1	1.5%	9.6%	88.9%
2	1.5%	9.6%	88.9%
3	1.5%	9.5%	89.0%
4	1.5%	9.5%	89.0%
5	1.5%	9.5%	89.0%
6	1.5%	9.5%	89.0%
7	1.5%	9.6%	89.0%
8	1.5%	9.6%	89.0%
9	1.5%	9.6%	88.9%
10	1.5%	9.6%	88.9%
11	1.5%	9.6%	88.9%

12	1.5%	9.6%	88.9%
13	1.5%	9.6%	88.9%
14	1.5%	9.6%	88.9%
15	1.5%	9.6%	88.9%
16	1.5%	29.1%	69.4%
17	1.5%	29.1%	69.4%
18	1.5%	29.1%	69.4%
19	1.5%	29.1%	69.4%
20	1.5%	29.1%	69.4%
21	1.5%	29.1%	69.4%
22	1.5%	29.1%	69.4%
23	1.5%	29.2%	69.4%
24	1.5%	29.1%	69.4%
25	1.5%	29.1%	69.4%
26	1.5%	29.1%	69.4%
27	1.5%	29.1%	69.4%
28	1.5%	29.1%	69.4%
29	1.5%	29.1%	69.4%
30	1.5%	29.1%	69.4%
31	1.5%	29.1%	69.4%
32	1.5%	29.2%	69.4%
33	1.5%	29.2%	69.4%
34	1.5%	29.1%	69.4%
35	1.5%	29.1%	69.4%
36	1.5%	29.2%	69.3%
37	1.5%	29.2%	69.3%
38	1.5%	29.1%	69.4%
39	1.5%	29.2%	69.3%
40	1.5%	29.2%	69.3%
41	1.5%	29.2%	69.3%
42	1.5%	29.2%	69.3%
43	1.5%	29.2%	69.3%
44	1.5%	29.2%	69.3%
45	1.5%	29.2%	69.3%
46	1.5%	29.2%	69.3%
47	1.5%	29.2%	69.3%
48	1.5%	50.6%	47.9%
49	1.5%	50.7%	47.8%
50	1.5%	50.7%	47.8%

51	1.5%	50.8%	47.8%
52	1.5%	50.8%	47.8%
53	1.5%	50.7%	47.8%
54	1.5%	50.7%	47.8%
55	1.5%	50.7%	47.8%
56	1.5%	50.7%	47.8%
57	1.5%	50.7%	47.8%
58	1.5%	50.7%	47.8%
59	1.5%	50.7%	47.8%
60	1.5%	50.7%	47.8%
61	1.5%	50.7%	47.8%
62	1.5%	50.7%	47.8%
63	1.5%	50.7%	47.8%

Table A.7: Thermodynamic state conditions and their associated uncertainties for all *iso*-propanol pyrolysis experiments conducted in the UM-RCF.

Run	P (atm)	P Uncert. (atm)	T (K)	T Uncert. (K)	Sample Time (ms)	Sample Uncert. (ms)
1	5.2	±0.1	967	±1	6.7	±1.5
2	5.0	±0.1	956	±1	26.9	±1.6
3	5.4	±0.1	972	±1	8.8	±1.6
4	5.1	±0.1	961	±1	29.0	±1.6
5	5.7	±0.1	986	±1	1.6	±1.7
6	5.2	±0.1	964	±1	42.0	±1.7
7	5.2	±0.1	965	±2	41.6	±1.6
8	5.1	±0.1	964	±2	41.6	±1.7
9	5.0	±0.1	957	±1	34.8	±1.7
10	5.5	±0.1	978	±1	0.4	±1.7
11	5.3	±0.1	968	±1	15.3	±1.7
12	5.5	±0.1	976	±1	0.3	±1.7
13	4.6	±0.1	938	±1	40.0	±1.6
14	4.8	±0.1	949	±1	15.1	±1.6
15	5.0	±0.1	954	±1	28.5	±1.6
16	4.5	±0.1	1071	±3	3.9	±1.7
17	4.3	±0.1	1055	±3	18.5	±1.7
18	4.5	±0.1	1067	±4	11.7	±1.8
19	4.2	±0.1	1051	±4	31.3	±1.7

20	4.6	±0.1	1075	±3	3.6	±1.6
21	4.5	±0.1	1072	±4	4.7	±1.6
22	4.2	±0.1	1053	±4	24.3	±1.6
23	4.1	±0.1	1048	±7	44.3	±1.7
24	4.5	±0.1	1073	±3	4.0	±1.7
25	4.4	±0.1	1064	±3	11.4	±1.7
26	4.3	±0.1	1061	±4	18.8	±1.6
27	4.1	±0.1	1043	±4	43.6	±1.6
28	4.1	±0.1	1045	±6	31.6	±1.7
29	4.5	±0.1	1071	±4	4.1	±1.6
30	4.5	±0.1	1074	±4	3.8	±1.6
31	4.4	±0.1	1064	±4	11.3	±1.6
32	4.6	±0.1	1076	±3	3.4	±1.6
33	4.4	±0.1	1065	±3	11.4	±1.6
34	4.4	±0.1	1062	±3	19.2	±1.7
35	4.2	±0.1	1053	±3	31.5	±1.7
36	4.3	±0.1	1061	±3	18.5	±1.6
37	4.2	±0.1	1051	±3	30.7	±1.6
38	4.1	±0.1	1046	±6	44.3	±1.7
39	9.5	±0.1	1061	±1	1.2	±1.7
40	9.0	±0.1	1045	±1	28.4	±1.7
41	10.2	±0.1	1083	±2	2.0	±1.6
42	9.6	±0.1	1076	±2	29.4	±1.6
43	10.6	±0.1	1088	±2	1.9	±1.6
44	9.9	±0.1	1071	±2	29.2	±1.6
45	9.8	±0.1	1068	±1	42.2	±1.6
46	10.3	±0.1	1081	±2	8.8	±1.6
47	10.1	±0.1	1076	±2	16.1	±1.6
48	4.3	±0.1	1201	±2	1.5	±1.6
49	3.9	±0.1	1164	±4	40.7	±1.5
50	4.7	±0.1	1175	±4	40.2	±1.7
51	4.6	±0.1	1157	±2	28.8	±1.6
52	4.7	±0.1	1174	±4	28.7	±1.7
53	4.6	±0.1	1164	±4	40.4	±1.8
54	5.2	±0.1	1205	±4	9.8	±1.7
55	5.3	±0.1	1207	±5	2.9	±1.7
56	5.0	±0.1	1191	±2	16.9	±1.7
57	5.6	±0.1	1227	±4	2.3	±1.7
58	5.0	±0.1	1186	±2	7.0	±1.7

59	5.2	±0.1	1205	±5	9.5	±1.6
60	5.1	±0.1	1194	±9	15.8	±1.7
61	5.2	±0.1	1199	±4	9.0	±1.6
62	5.3	±0.1	1204	±2	1.4	±1.6
63	5.0	±0.1	1186	±2	15.4	±1.6

Table A.8: Mole Fraction (MF) concentration results for *iso*-propanol and the intermediate species measured for all *iso*-propanol pyrolysis experiments conducted in the UM-RCF.

Run	**$2\text{-}C_3H_7OH$ (MF)**	**CH_3COCH_3 (MF)**	**CH_3CHO (MF)**	**C_3H_6 (MF)**	**C_2H_6 (MF)**	**C_2H_4 (MF)**	**C_2H_2 (MF)**	**CH_4 (MF)**
1	1.22E-02	1.97E-04	1.14E-05	1.46E-04	0.00E+00	0.00E+00	0.00E+00	1.61E-05
2	8.98E-03	7.74E-04	1.14E-04	4.99E-04	2.13E-05	5.81E-05	0.00E+00	1.57E-04
3	1.22E-02	3.49E-04	5.14E-05	2.49E-04	0.00E+00	3.23E-06	0.00E+00	4.26E-05
4	7.77E-03	7.11E-04	1.03E-04	4.82E-04	2.39E-05	6.69E-05	0.00E+00	1.82E-04
5	1.37E-02	3.64E-05	0.00E+00	6.43E-05	0.00E+00	0.00E+00	0.00E+00	0.00E+00
6	8.45E-03	1.08E-03	1.59E-04	6.83E-04	3.99E-05	1.18E-04	0.00E+00	3.02E-04
7	8.13E-03	1.01E-03	1.47E-04	6.33E-04	3.50E-05	1.02E-04	0.00E+00	2.82E-04
8	8.42E-03	1.04E-03	1.50E-04	6.26E-04	3.59E-05	1.05E-04	0.00E+00	2.81E-04
9	9.96E-03	1.26E-03	1.84E-04	7.65E-04	4.17E-05	1.21E-04	0.00E+00	3.02E-04
10	1.14E-02	1.09E-05	0.00E+00	6.79E-05	0.00E+00	0.00E+00	0.00E+00	0.00E+00
11	1.16E-02	8.73E-04	1.36E-04	5.95E-04	1.37E-05	3.83E-05	0.00E+00	1.28E-04
12	1.15E-02	4.73E-05	0.00E+00	7.03E-05	0.00E+00	0.00E+00	0.00E+00	0.00E+00
13	1.05E-02	9.81E-04	1.43E-04	6.25E-04	2.16E-05	6.40E-05	0.00E+00	1.76E-04
14	1.09E-02	2.66E-04	3.24E-05	2.24E-04	3.02E-05	3.02E-05	0.00E+00	3.02E-05
15	1.03E-02	1.10E-03	1.68E-04	6.98E-04	2.99E-05	8.14E-05	0.00E+00	2.13E-04
16	1.03E-02	8.86E-04	1.22E-04	6.06E-04	2.98E-05	5.78E-05	0.00E+00	2.18E-04
17	7.67E-03	1.27E-03	1.91E-04	9.90E-04	6.16E-05	1.85E-04	0.00E+00	4.94E-04
18	8.78E-03	1.52E-03	2.38E-04	1.15E-03	7.22E-05	2.07E-04	0.00E+00	5.13E-04
19	6.89E-03	1.54E-03	2.26E-04	1.29E-03	9.12E-05	3.08E-04	0.00E+00	7.47E-04
20	1.02E-02	1.11E-03	1.63E-04	8.61E-04	4.40E-05	1.01E-04	0.00E+00	2.78E-04
21	1.08E-02	1.36E-03	2.24E-04	9.87E-04	5.07E-05	1.21E-04	0.00E+00	3.26E-04
22	7.94E-03	1.56E-03	2.27E-04	1.23E-03	8.29E-05	2.66E-04	0.00E+00	6.48E-04
23	7.39E-03	1.63E-03	2.52E-04	1.41E-03	1.04E-04	3.72E-04	0.00E+00	9.05E-04
24	1.08E-02	1.31E-03	2.12E-04	9.45E-04	4.81E-05	1.12E-04	0.00E+00	3.15E-04
25	8.77E-03	1.26E-03	1.93E-04	9.99E-04	6.13E-05	1.72E-04	0.00E+00	4.42E-04
26	9.03E-03	1.49E-03	2.31E-04	1.13E-03	7.57E-05	2.36E-04	0.00E+00	5.83E-04
27	8.45E-03	1.72E-03	2.49E-04	1.39E-03	9.95E-05	3.57E-04	0.00E+00	8.51E-04
28	8.71E-03	1.61E-03	2.47E-04	1.20E-03	7.41E-05	2.50E-04	0.00E+00	6.39E-04
29	1.11E-02	1.05E-03	1.68E-04	7.57E-04	3.73E-05	7.76E-05	0.00E+00	2.60E-04
30	1.02E-02	1.14E-03	1.97E-04	8.82E-04	4.46E-05	9.58E-05	0.00E+00	2.94E-04

31	8.94E-03	1.25E-03	1.91E-04	1.04E-03	6.76E-05	1.84E-04	0.00E+00	4.68E-04
32	1.09E-02	1.18E-03	1.93E-04	8.95E-04	4.32E-05	9.39E-05	0.00E+00	2.84E-04
33	7.60E-03	1.16E-03	1.69E-04	9.62E-04	5.97E-05	1.66E-04	0.00E+00	4.30E-04
34	8.09E-03	1.31E-03	2.19E-04	1.03E-03	6.43E-05	1.93E-04	0.00E+00	5.16E-04
35	7.52E-03	1.48E-03	2.09E-04	1.19E-03	8.00E-05	2.67E-04	0.00E+00	6.71E-04
36	8.34E-03	1.29E-03	1.84E-04	1.00E-03	6.52E-05	1.96E-04	0.00E+00	5.33E-04
37	7.12E-03	1.42E-03	2.06E-04	1.18E-03	7.95E-05	2.64E-04	0.00E+00	6.67E-04
38	7.17E-03	1.37E-03	2.23E-04	1.12E-03	7.34E-05	2.55E-04	0.00E+00	6.66E-04
39	1.06E-02	5.52E-04	9.66E-05	4.29E-04	1.59E-05	2.76E-05	0.00E+00	1.24E-04
40	7.11E-03	1.03E-03	1.90E-04	9.11E-04	4.65E-05	1.48E-04	0.00E+00	4.83E-04
41	9.66E-03	3.84E-04	7.53E-05	3.54E-04	1.39E-05	2.56E-05	0.00E+00	1.09E-04
42	5.84E-03	9.20E-04	1.99E-04	9.86E-04	5.68E-05	1.73E-04	0.00E+00	5.54E-04
43	9.88E-03	6.07E-04	1.22E-04	5.52E-04	2.42E-05	4.47E-05	0.00E+00	1.77E-04
44	6.23E-03	9.90E-04	2.17E-04	1.08E-03	6.20E-05	1.85E-04	0.00E+00	5.95E-04
45	5.88E-03	1.29E-03	2.70E-04	1.37E-03	8.85E-05	2.91E-04	0.00E+00	9.02E-04
46	8.20E-03	1.01E-03	2.03E-04	9.02E-04	5.03E-05	1.29E-04	0.00E+00	4.24E-04
47	6.51E-03	1.08E-03	2.28E-04	1.08E-03	6.34E-05	1.79E-04	0.00E+00	5.68E-04
48	8.61E-03	1.04E-03	3.90E-04	1.55E-03	1.93E-04	2.61E-04	3.20E-05	7.11E-04
49	4.57E-03	9.14E-04	3.95E-04	2.28E-03	5.19E-04	1.22E-03	1.56E-04	2.94E-03
50	4.02E-03	9.50E-04	4.07E-04	2.34E-03	5.53E-04	1.36E-03	1.80E-04	3.34E-03
51	5.90E-03	1.24E-03	4.69E-04	2.35E-03	4.08E-04	9.61E-04	1.15E-04	2.46E-03
52	4.45E-03	1.22E-03	5.11E-04	2.86E-03	6.82E-04	1.67E-03	2.17E-04	4.06E-03
53	4.73E-03	1.01E-03	4.24E-04	2.39E-03	5.50E-04	1.36E-03	1.74E-04	3.35E-03
54	6.10E-03	1.04E-03	4.75E-04	2.09E-03	4.41E-04	7.92E-04	1.05E-04	1.98E-03
55	7.01E-03	1.53E-03	6.17E-04	2.38E-03	3.96E-04	5.75E-04	7.15E-05	1.53E-03
56	4.97E-03	9.84E-04	4.53E-04	2.20E-03	5.16E-04	1.05E-03	1.39E-04	2.60E-03
57	8.67E-03	1.22E-03	3.32E-04	1.44E-03	1.36E-04	2.18E-04	2.13E-05	6.74E-04
58	6.74E-03	1.32E-03	5.05E-04	2.22E-03	3.54E-04	6.20E-04	7.45E-05	1.66E-03
59	5.51E-03	1.10E-03	5.30E-04	2.37E-03	5.68E-04	1.03E-03	1.40E-04	2.54E-03
60	5.37E-03	9.44E-04	4.27E-04	2.13E-03	4.58E-04	9.09E-04	1.20E-04	2.28E-03
61	5.82E-03	1.25E-03	5.04E-04	2.34E-03	4.81E-04	9.12E-04	1.17E-04	2.31E-03
62	8.15E-03	1.41E-03	4.65E-04	1.88E-03	2.46E-04	3.50E-04	4.12E-05	1.01E-03
63	5.09E-03	1.20E-03	5.22E-04	2.51E-03	5.46E-04	1.13E-03	1.46E-04	2.84E-03

Table A.9: Percent differences between the experimental observations for each species and the model predictions for those species at the four conditions of interest in the present work.

Time (msec)	CH_4	C_2H_2	C_2H_4	C_2H_6	C_3H_6	CH_3CHO	CH_3COCH_3	2-C_3H_7OH
	965 K 5.2 atm							
< 10	-68%	N/A	96%	N/A	115%	-36%	-28%	-19%
10 – 30	-12%	N/A	-62%	2223%	145%	135%	51%	-33%
>30	33%	N/A	-125%	3235%	159%	157%	83%	-35%
	1067 K 4.4 atm							
< 10	-57%	N/A	-19%	204%	29%	-18%	-16%	-14%
10 – 30	-57%	N/A	-27%	216%	-12%	-52%	-37%	-20%
>30	-51%	N/A	-23%	250%	-21%	-58%	-38%	-18%
	1074 K 10.0 atm							
< 10	-77%	N/A	-68%	121%	-25%	-54%	-61%	-18%
10 – 30	-73%	N/A	-68%	149%	-43%	-67%	-67%	-19%
>30	-63%	N/A	-57%	241%	-36%	-62%	-62%	-16%
	1193 K 5.1 atm							
< 10	-69%	-62%	43%	-9%	-26%	-53%	-71%	245%
10 – 30	-59%	-50%	70%	-21%	-19%	-43%	-74%	1412%
>30	-58%	-49%	67%	-28%	-18%	-42%	-76%	3279%

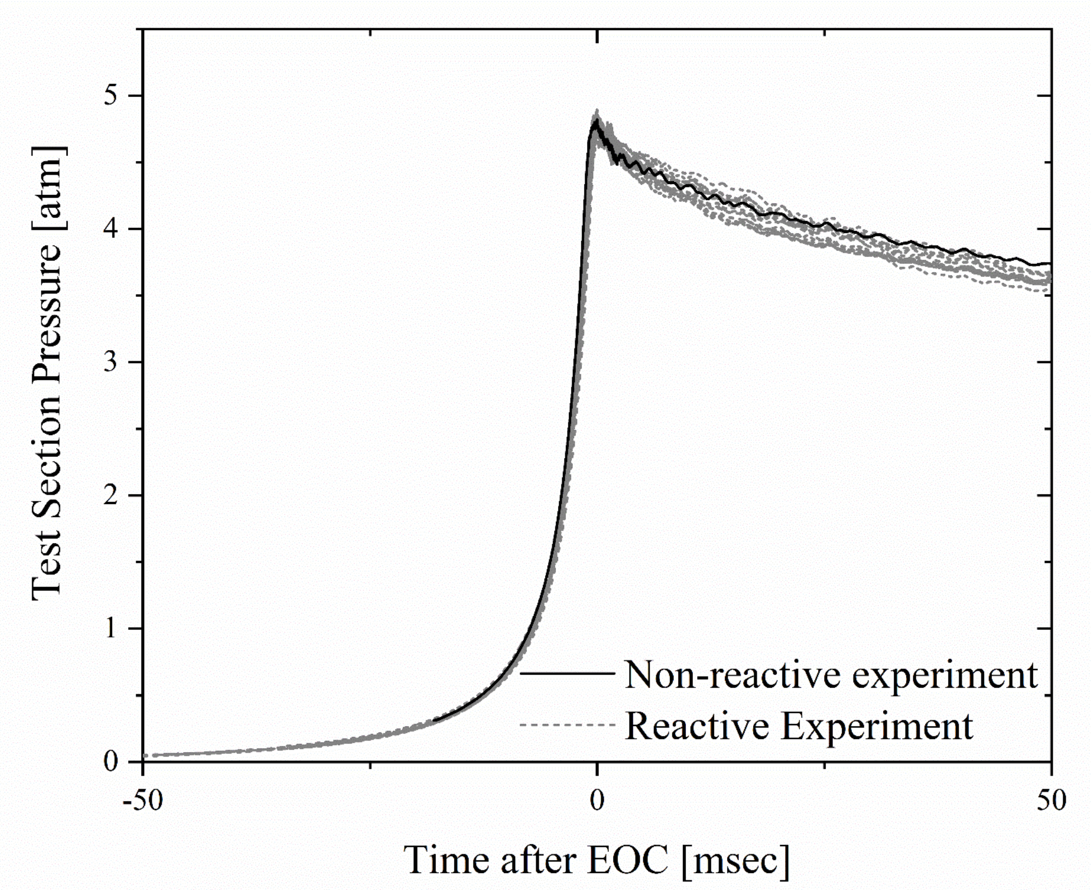

Figure A.1: Comparison between reactive and non-reactive experimental pressure traces. Reactive conditions of T=1090K and P=4.8 atm for 1.5% *iso*-propanol, 69.3% nitrogen, and 29.2% argon. Non-reactive conditions targeting T=1090K and P=4.8 atm for 88.6% nitrogen, and 11.4% argon.

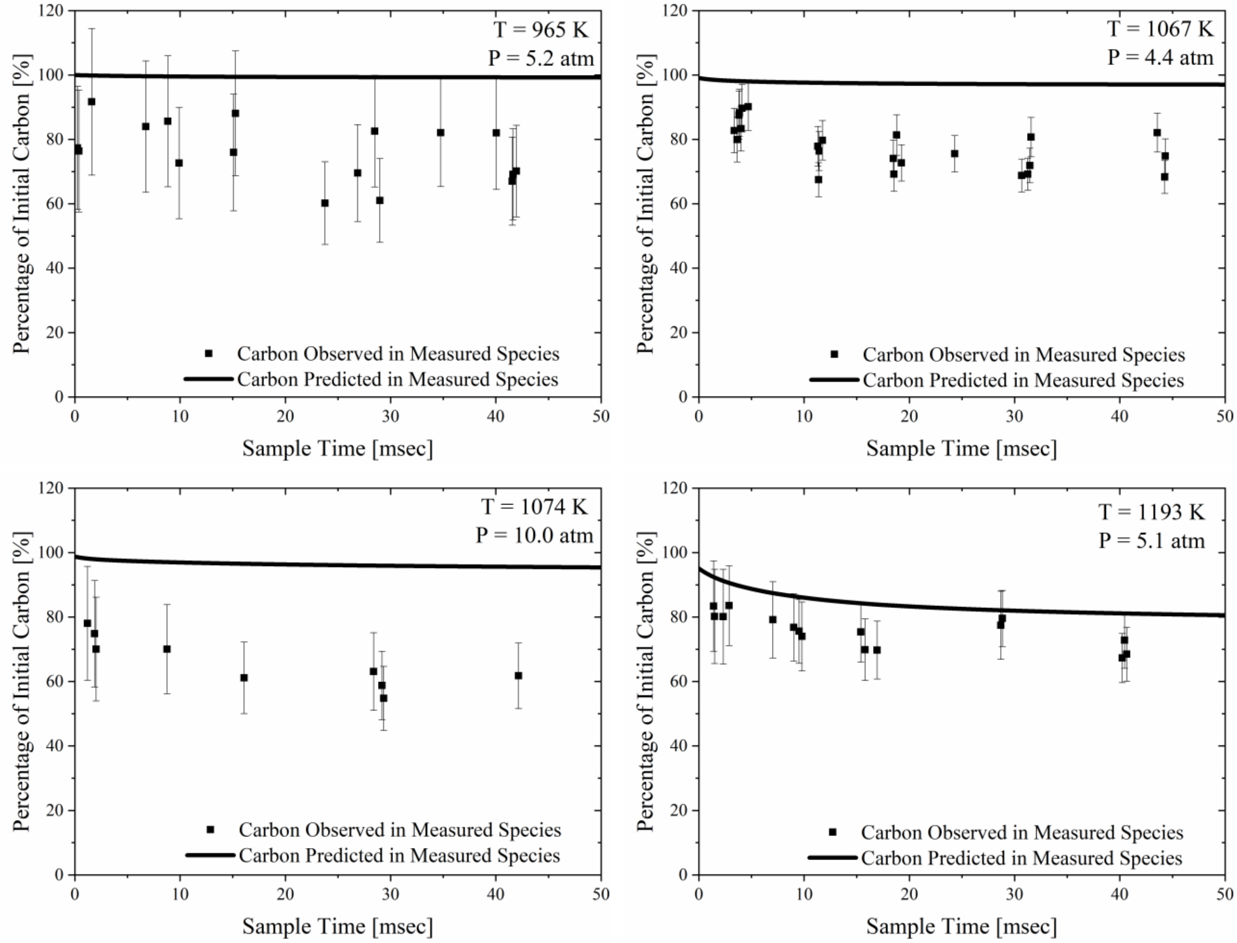

Figure A.2: Carbon balance comparison between model predictions and experimental results for all intermediate species measured and *iso*-propanol at the four conditions of interest studied in the UM-RCF.

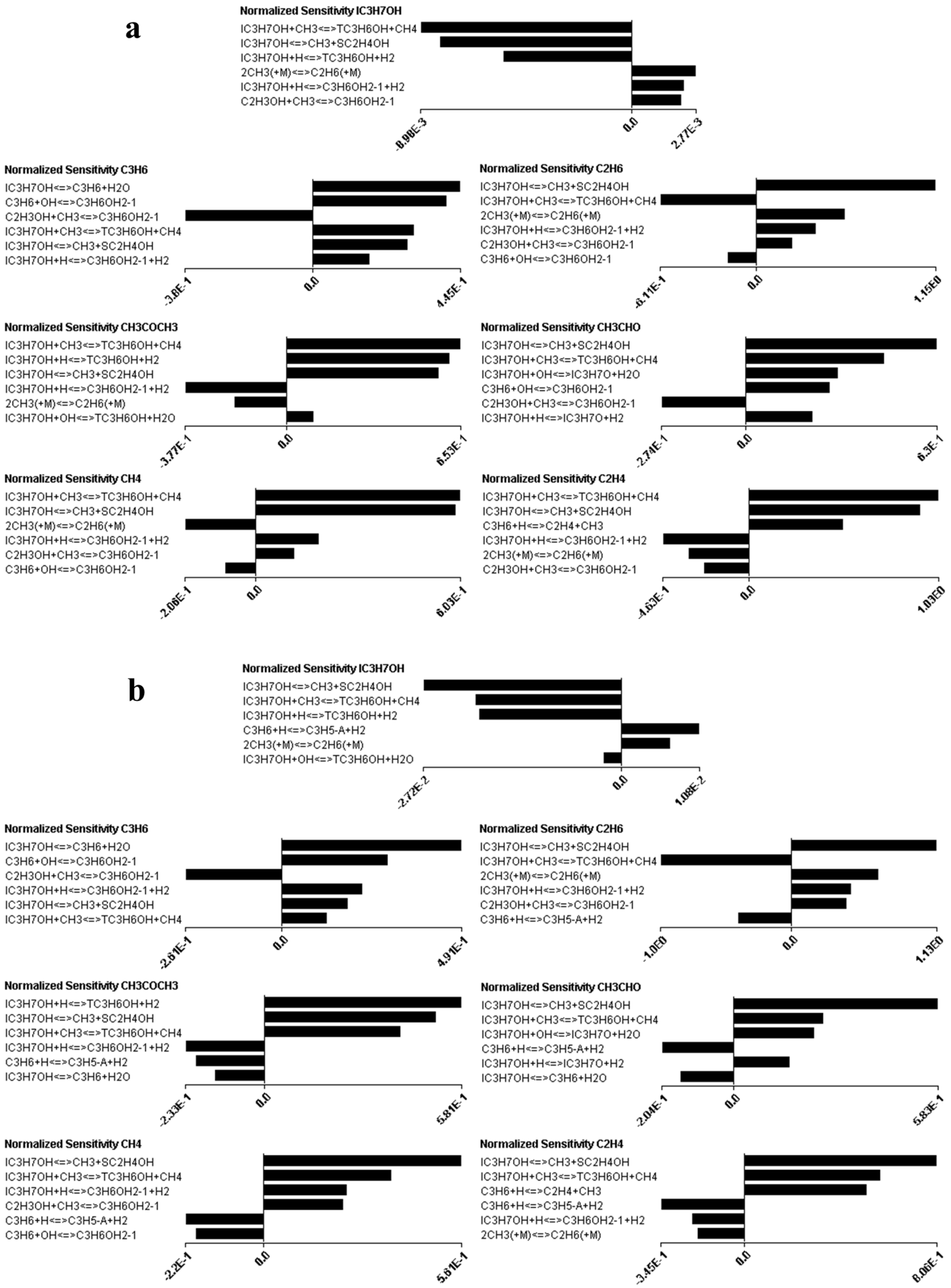

Figure A.3: Sensitivity analyses of major species at (a) 5 ms and (b) 25 ms after EOC at T = 965 K and P = 5.2 atm for 1.5% *iso*-propanol, 9.6% argon, and 88.9% nitrogen.

]

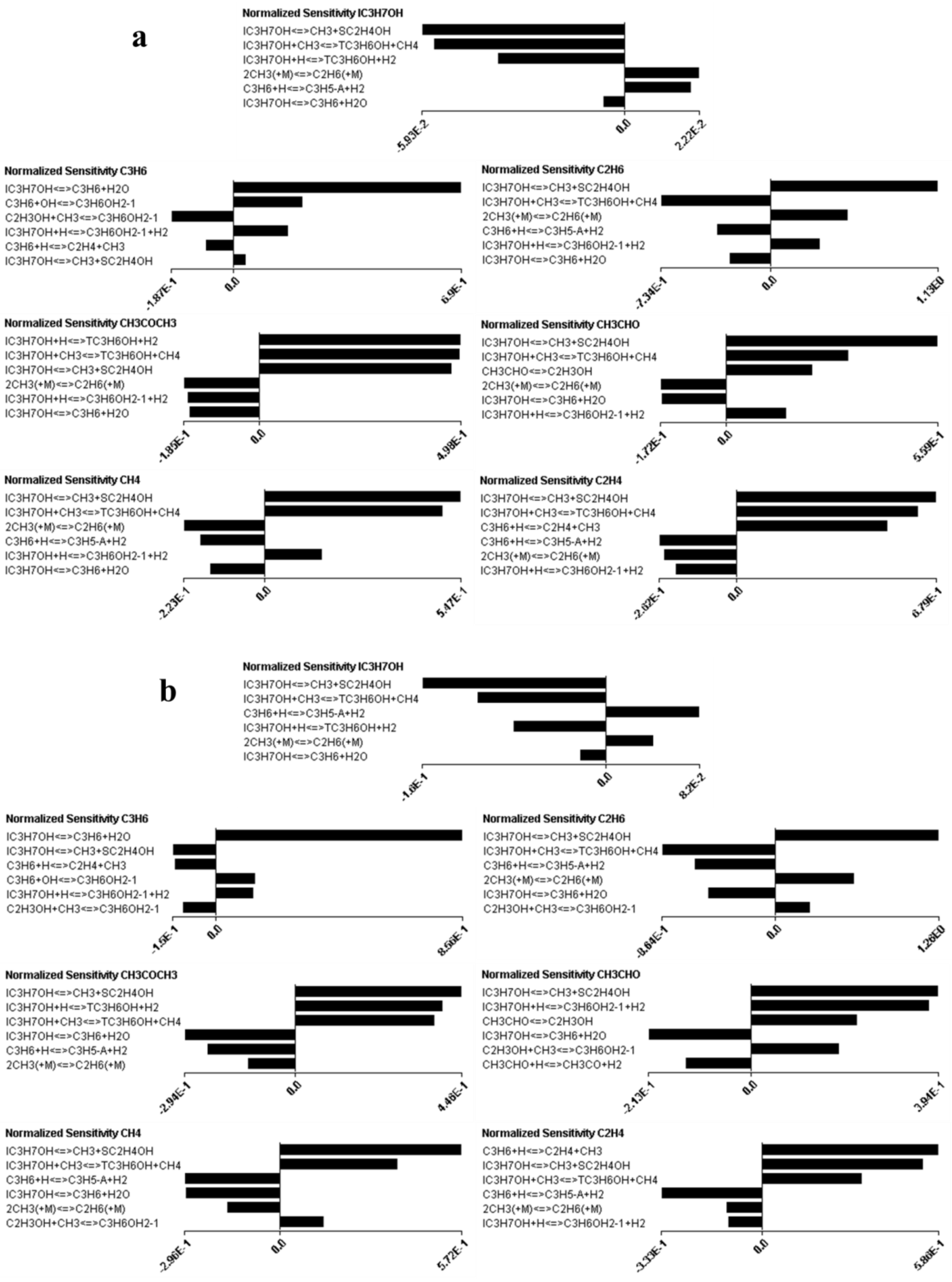

Figure A.4: Sensitivity analyses of major species at (a) 5 ms and (b) 25 ms after EOC at T = 1067 K and P = 4.4 atm for 1.5% *iso*-propanol, 29.1% argon, and 69.4% nitrogen.

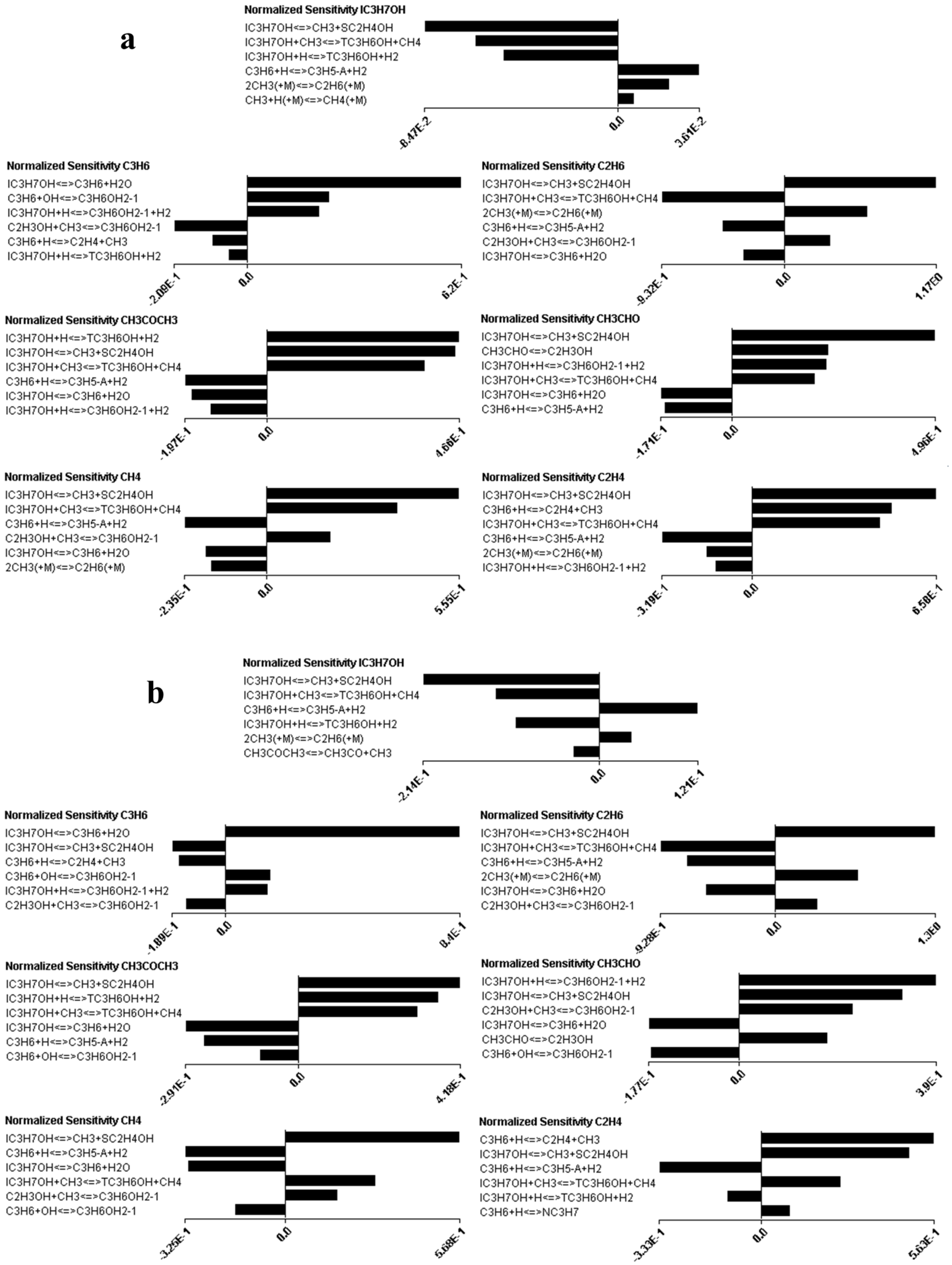

Figure A.5: Sensitivity analyses of major species at (a) 5 ms and (b) 25 ms after EOC at T = 1074 K and P = 10.0 atm for 1.5% *iso*-propanol, 29.2% argon, and 69.3% nitrogen.

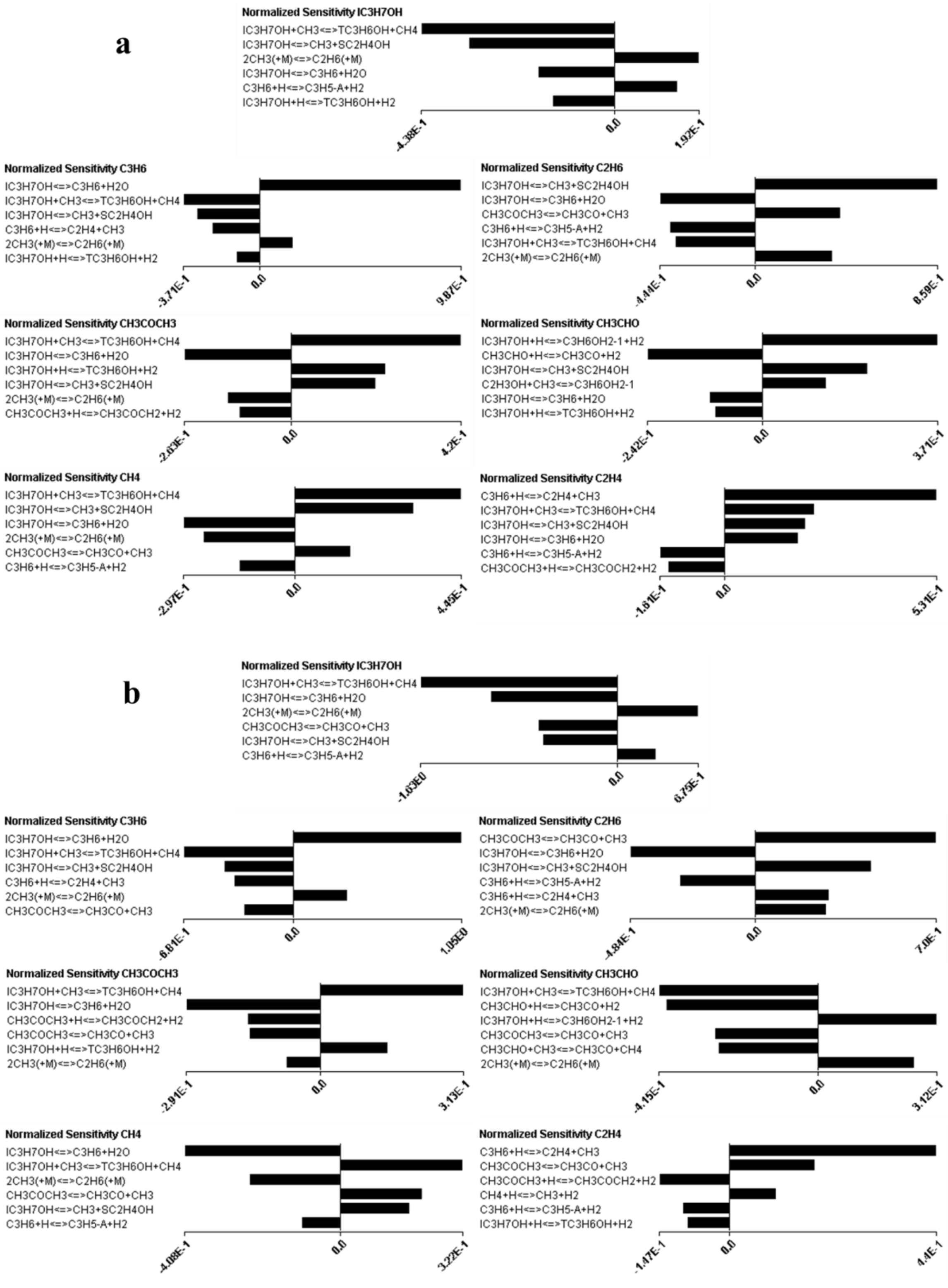

Figure A.6: Sensitivity analyses of major species at (a) 5 ms and (b) 25 ms after EOC at T = 1193 K and P = 5.1 atm for 1.5% *iso*-propanol, 50.7% argon, and 47.8% nitrogen.

Appendix B: Supplemental Material for Chapter 3

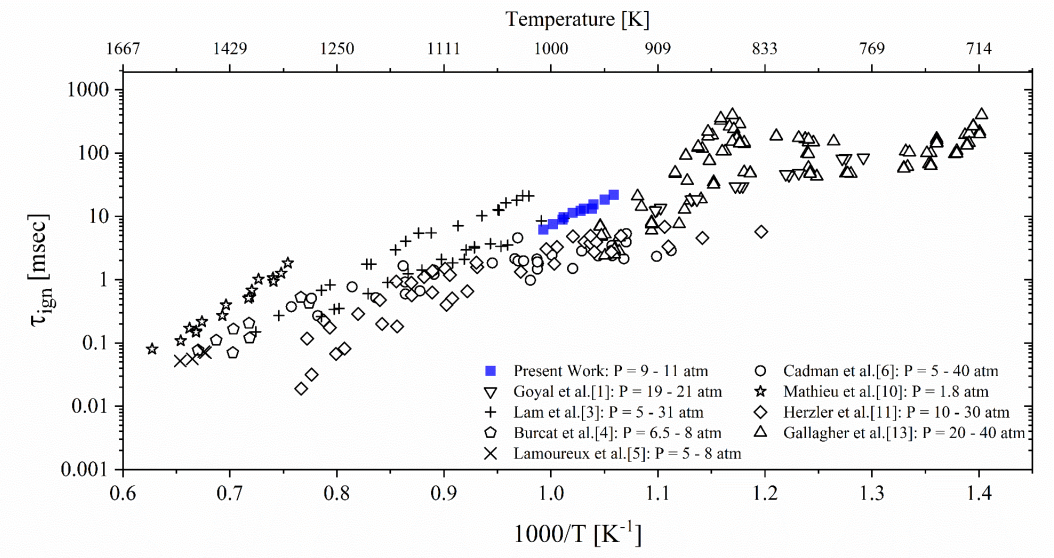

Figure B.1: Summary of unscaled autoignition delay time results for propane/air mixtures at ϕ=0.5. The references for each set of data can be found in the references section for Chapter 3.

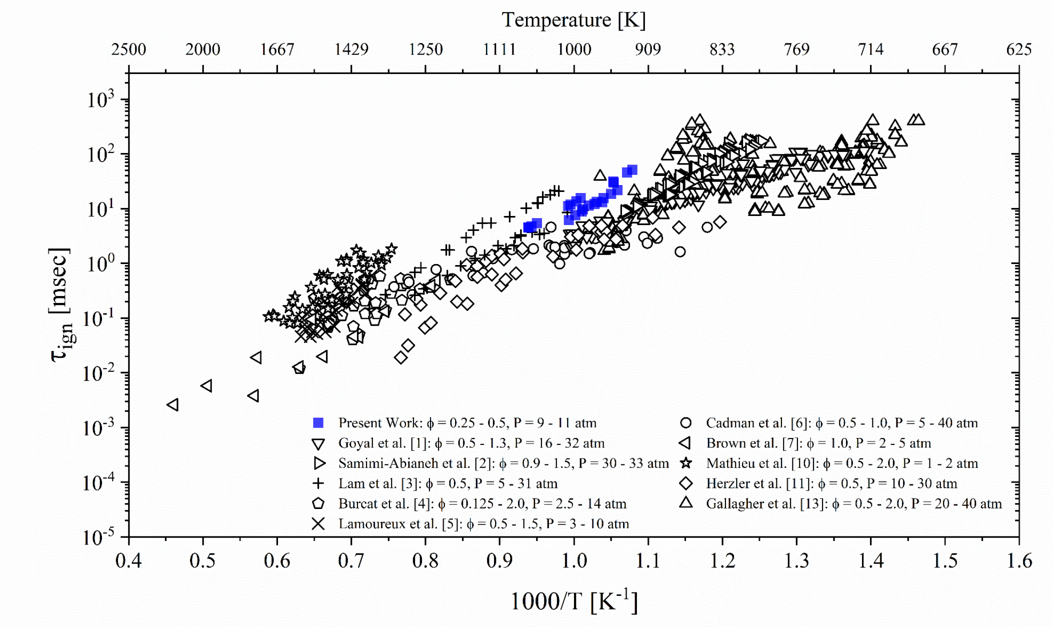

Figure B.2: Summary of unscaled autoignition delay time results for propane/air mixtures including all equivalence ratios. The references for each set of data can be found in the references section for Chapter 3.

Table B.1: Thermodynamic state conditions, test gas mixture composition and autoignition delay time results for all propane/air experiments conducted in the UM-RCF.

					Mole Fraction				
ϕ	P (atm)	T (K)	1000/T	IDT (ms)	C_3H_8	O_2	CO_2	Ar	N_2
0.5	10.4	989	1.011	8.9	0.020	0.206	0.000	0.055	0.719
0.5	10.9	998	1.002	7.6	0.020	0.206	0.000	0.055	0.719
0.5	11.3	1007	0.993	6.1	0.020	0.206	0.000	0.055	0.719
0.5	10.1	980	1.020	11.4	0.020	0.206	0.000	0.054	0.719
0.5	9.7	970	1.031	13.2	0.020	0.206	0.000	0.055	0.719
0.5	9.9	973	1.028	12.2	0.020	0.206	0.000	0.054	0.719
0.5	10.5	988	1.012	9.7	0.020	0.206	0.000	0.054	0.719
0.5	10.7	963	1.038	13.1	0.020	0.206	0.016	0.000	0.757
0.5	9.9	945	1.059	21.9	0.020	0.206	0.016	0.000	0.757
0.5	10.1	952	1.050	18.5	0.020	0.206	0.014	0.000	0.759
0.5	10.5	962	1.040	15.4	0.021	0.206	0.014	0.000	0.759
0.25	10.1	1005	0.996	11.8	0.010	0.208	0.000	0.017	0.765
0.25	10.2	1008	0.992	11.1	0.010	0.208	0.000	0.017	0.765
0.25	9.5	990	1.009	15.6	0.010	0.208	0.000	0.017	0.765
0.25	9.7	997	1.003	13.6	0.010	0.208	0.000	0.017	0.765
0.25	10.0	1053	0.950	5.4	0.010	0.208	0.000	0.120	0.661
0.25	10.3	1061	0.943	4.7	0.010	0.208	0.000	0.120	0.661
0.25	10.4	1066	0.938	4.6	0.010	0.208	0.000	0.120	0.661
0.25	10.4	1066	0.938	4.5	0.010	0.208	0.000	0.120	0.661
0.25	8.9	927	1.078	51.4	0.010	0.208	0.064	0.000	0.718
0.25	9.8	950	1.053	31.3	0.010	0.208	0.064	0.000	0.718
0.25	9.8	949	1.053	29.6	0.010	0.208	0.064	0.000	0.718
0.25	9.1	933	1.072	45.5	0.010	0.208	0.064	0.000	0.718

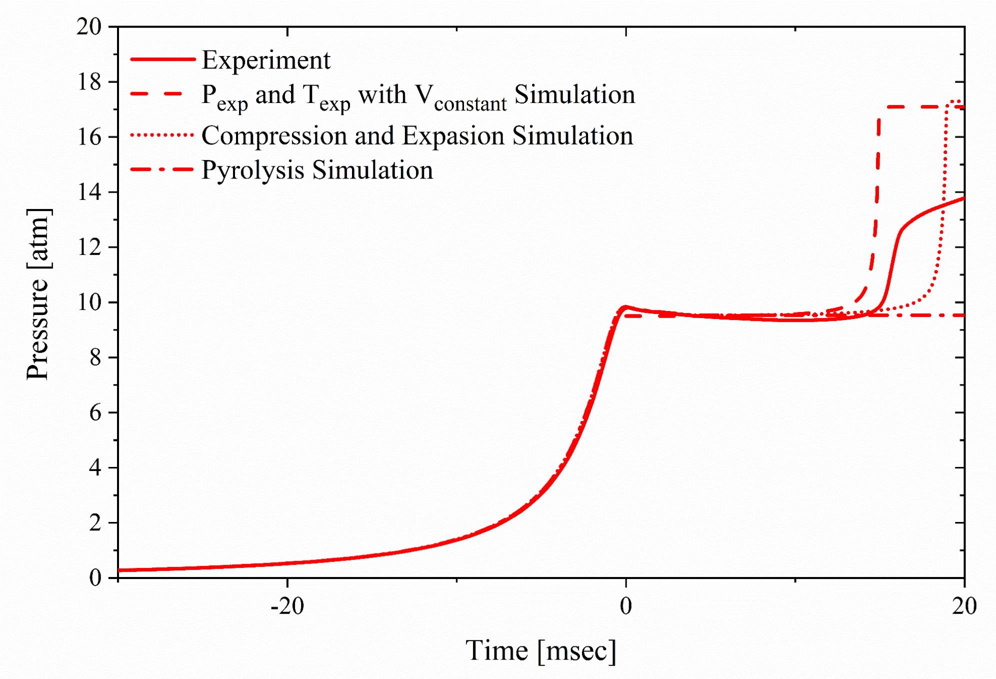

Figure B.3: Comparison of measured (solid lines) and simulated pressure histories for propane/air mixtures at P = 9.5 atm, T = 990 K, and ϕ = 0.25. Simulations using constant volume (dashed line), compression and expansion (dotted line), and non-igniting conditions (dash-dot line) are included for comparison with the experimental results.

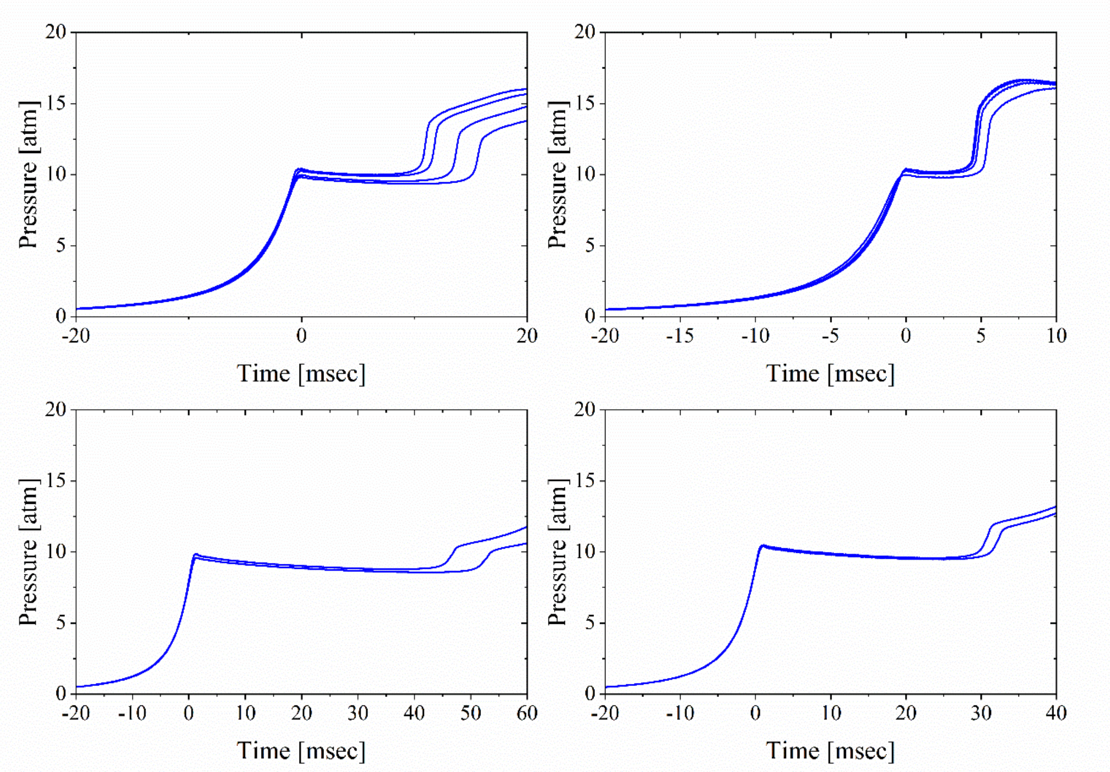

Figure B.4: Pressure traces for all strong ignition experiments conducted at ϕ = 0.25 including compression stroke and ignition delay time.

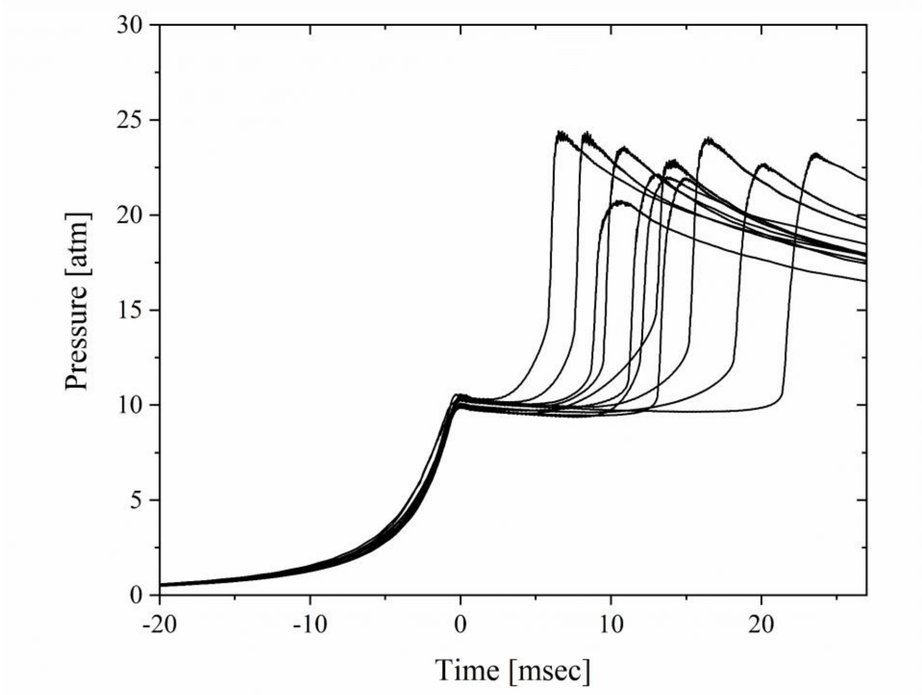

Figure B.5: Pressure traces for all mixed ignition experiments conducted at $\phi = 0.5$ including compression stroke and ignition delay time.

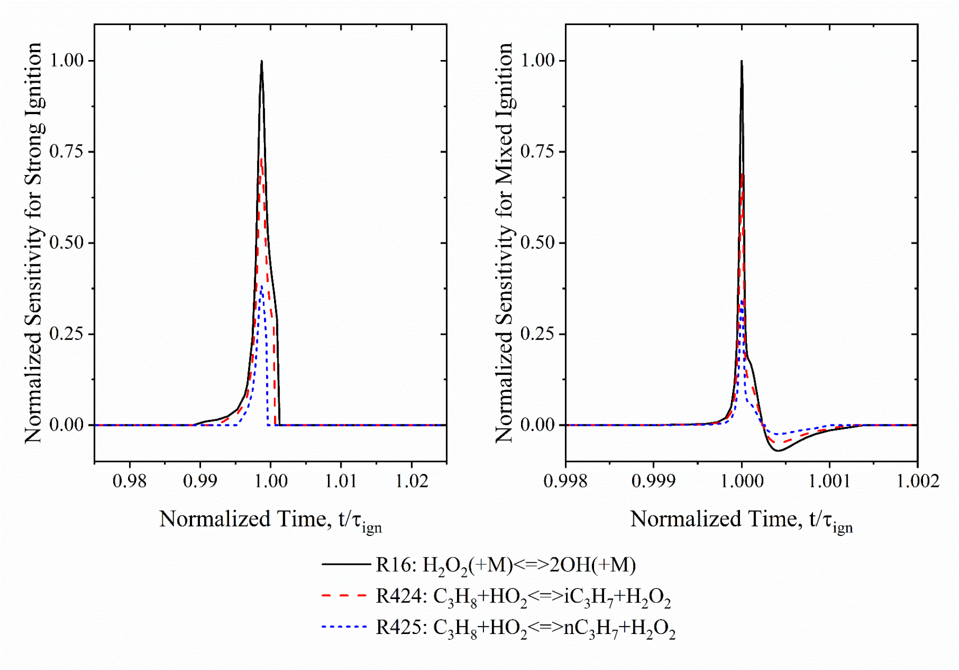

(a) (b)

Figure B.6: Results of CHEMKIN OH sensitivity analysis at typical strong ignition and mixed ignition conditions. Results were normalized based on the maximum sensitivity from the top reaction (R16) in each simulation, and time was normalized based on ignition delay time. The conditions shown in (a) were P = 10 atm, T = 1000 K, and $\phi = 0.25$, and the conditions shown in (b) are P = 10 atm, T = 950 K, and $\phi = 0.5$.

Appendix C: Supplemental Material for Chapter 4

Table C.1: Thermodynamic state conditions, test gas mixture composition, and autoignition delay time results for all propane experiments with a nitrogen dilution of 7.5 conducted in the UM-RCF.

					Mole Fraction				
ϕ	**P (atm)**	**T (K)**	**1000/T**	**IDT (ms)**	**C_3H_8**	**O_2**	**CO_2**	**Ar**	**N_2**
1.0	9.5	911	1.097642	46.71	0.023	0.115	0.051	0	0.811
1.0	9.5	911	1.097194	46.82	0.023	0.115	0.051	0	0.811
1.0	9.6	915	1.092464	43.46	0.023	0.115	0.051	0	0.811
1.0	9.4	980	1.020076	13.58	0.023	0.115	0	0.108	0.754
1.0	9.9	992	1.007697	10.84	0.023	0.115	0	0.108	0.754
1.0	10.0	992	1.00765	10.28	0.023	0.116	0	0.108	0.753
1.0	9.8	1040	0.961462	5.31	0.023	0.116	0	0.215	0.646
1.0	10.0	1044	0.957762	4.8	0.023	0.116	0	0.215	0.646

Table C.2: Thermodynamic state conditions, test gas mixture composition, and autoignition delay time results for propane/air experiments conducted in the TU-RCM.

					Mole Fraction			
ϕ	**P (atm)**	**T (K)**	**1000/T**	**IDT (ms)**	**C_3H_8**	**O_2**	**Ar**	**N_2**
1.0	19.2	744	1.344122	77.88	0.040	0.202	0.217	0.541
1.0	19.4	745	1.343039	75.32	0.040	0.202	0.217	0.541
1.0	19.7	746	1.339854	75.48	0.040	0.202	0.217	0.541
1.0	20.0	843	1.186606	52.17	0.040	0.202	0.590	0.168
1.0	20.2	846	1.182494	47.66	0.040	0.202	0.590	0.168
1.0	20.5	849	1.177288	44.64	0.040	0.202	0.590	0.168
1.0	19.7	902	1.108107	16.11	0.040	0.202	0.697	0.061
1.0	19.7	905	1.104594	16.11	0.040	0.202	0.697	0.061
1.0	19.7	905	1.10446	15.8	0.040	0.202	0.697	0.061
1.0	24.8	748	1.337793	42.35	0.040	0.202	0.217	0.541
1.0	24.8	748	1.337506	43.59	0.040	0.202	0.217	0.541
1.0	24.8	748	1.337345	42.46	0.040	0.202	0.217	0.541
1.0	24.8	748	1.336345	41.98	0.040	0.202	0.217	0.541
1.0	24.9	749	1.335292	41.42	0.040	0.202	0.217	0.541
1.0	24.5	852	1.173475	30.44	0.040	0.202	0.590	0.168
1.0	24.6	853	1.172869	30	0.040	0.202	0.590	0.168
1.0	24.7	853	1.171674	29.57	0.040	0.202	0.590	0.168
1.0	24.7	902	1.108623	10.25	0.040	0.202	0.697	0.061
1.0	25.2	906	1.103534	10.64	0.040	0.202	0.697	0.061
1.0	25.4	907	1.102256	10.77	0.040	0.202	0.697	0.061

Appendix D: Supplemental Material for Chapter 5

Table D.1: Initial P_4 and $P_4/2$, mixture conditions, thermodynamic state conditions before and after the passage of the shock wave, and the experimental wave and Chapman – Jouguet detonation velocity for the propane-oxygen mixtures with varying levels of nitrogen dilution.

			Mole Fraction									
Run	P_4 (bar)	$P_4/2$ (bar)	C_3H_8	O_2	N_2	ER	P_1 (bar)	T_1 (K)	P_2 (bar)	T_2 (K)	V_{exp} (m/s)	V_{CJ} (m/s)
1	10	5	0.168	0.832	0.000	1.01	0.067	293	1.319	853	1253	2243
2	10	5	0.169	0.831	0.000	1.01	0.067	294	7.770	2740	2996	2244
6	10	5	0.166	0.834	0.000	0.99	0.068	294	7.530	2671	2937	2235
7	11	5.5	0.165	0.835	0.000	0.99	0.068	294	4.910	1957	2375	2234
8	9	4.5	0.166	0.834	0.000	0.99	0.069	294	4.419	1796	2238	2236
9	8	4	0.170	0.830	0.000	1.02	0.069	295	1.237	807	1195	2249
15	4	2	0.166	0.834	0.000	0.99	0.068	294	0.909	698	1041	2235
16	3	1.5	0.166	0.834	0.000	0.99	0.068	295	0.797	654	977	2235
18	12	6	0.167	0.833	0.000	1.00	0.068	294	4.678	1888	2320	2238
19	19	9.5	0.166	0.834	0.000	0.99	0.068	293	4.376	1804	2245	2235
20	6	3	0.166	0.834	0.000	1.00	0.068	294	1.084	763	1133	2236
21	5	2.5	0.167	0.833	0.000	1.00	0.067	293	0.993	734	1093	2238
22	13	6.5	0.167	0.833	0.000	1.00	0.068	294	4.347	1791	2235	2238
23	14	7	0.166	0.834	0.000	1.00	0.068	294	5.190	2036	2443	2237
24	15	7.5	0.166	0.834	0.000	0.99	0.068	294	4.358	1801	2242	2235
25	16	8	0.167	0.833	0.000	1.00	0.068	295	4.376	1805	2248	2238
26	17	8.5	0.166	0.834	0.000	1.00	0.068	294	4.374	1802	2244	2237
27	18	9	0.166	0.834	0.000	1.00	0.068	295	4.361	1801	2244	2237
28	19	9.5	0.164	0.836	0.000	0.98	0.068	293	4.306	1779	2221	2232
29	19	9.5	0.166	0.834	0.000	1.00	0.068	294	4.376	1804	2246	2236
30	12	6	0.165	0.835	0.000	0.99	0.068	294	4.367	1805	2244	2233
31	18	9	0.166	0.834	0.000	0.99	0.068	293	4.337	1794	2236	2236
32	17	7.5	0.165	0.835	0.000	0.99	0.068	294	4.518	1850	2283	2233
33	15	7.5	0.165	0.835	0.000	0.99	0.068	295	4.326	1794	2234	2232
34	11	5.5	0.166	0.834	0.000	1.00	0.068	295	4.321	1789	2232	2236
35	11	5.5	0.166	0.834	0.000	1.00	0.068	293	4.176	1744	2193	2236
36	10	5	0.167	0.833	0.000	1.00	0.068	294	5.142	2015	2427	2239
37	10	5	0.167	0.833	0.000	1.00	0.068	294	4.394	1800	2244	2239
38	9	4.5	0.167	0.833	0.000	1.00	0.068	294	4.459	1827	2268	2239
39	8	4	0.167	0.833	0.000	1.00	0.068	294	1.228	817	1205	2238

41	8	4	0.167	0.833	0.000	1.00	0.068	294	1.225	813	1200	2239
42	6	3	0.166	0.834	0.000	0.99	0.068	294	1.101	769	1140	2236
43	4	2	0.165	0.835	0.000	0.99	0.068	294	0.872	683	1019	2232
44	3	1.5	0.166	0.834	0.000	1.00	0.068	294	0.768	641	958	2237
45	13	6.5	0.166	0.834	0.000	1.00	0.068	294	4.360	1797	2239	2237
47	16	8	0.167	0.833	0.000	1.00	0.068	294	4.375	1799	2243	2239
48	10	5	0.166	0.834	0.000	0.99	0.135	294	1.914	717	1068	2265
49	10	5	0.166	0.834	0.000	0.99	0.135	294	9.499	1911	2338	2266
50	10	5	0.167	0.833	0.000	1.00	0.135	294	1.943	723	1077	2269
51	11	5.5	0.166	0.834	0.000	0.99	0.135	294	8.843	1822	2261	2266
52	9	4.5	0.166	0.834	0.000	0.99	0.135	294	9.070	1852	2287	2266
53	8	4	0.167	0.833	0.000	1.00	0.136	294	9.108	1852	2288	2268
54	7	3.5	0.167	0.833	0.000	1.00	0.136	294	9.129	1853	2290	2269
55	6	3	0.166	0.834	0.000	0.99	0.135	294	8.924	1829	2267	2266
56	5	2.5	0.166	0.834	0.000	1.00	0.135	294	9.092	1853	2289	2267
57	4	2	0.166	0.834	0.000	1.00	0.135	294	1.233	579	861	2267
58	3	1.5	0.166	0.834	0.000	0.99	0.135	294	1.057	543	801	2265
59	2	1	0.166	0.834	0.000	0.99	0.135	294	0.836	493	715	2266
60	12	6	0.166	0.834	0.000	0.99	0.135	294	9.041	1853	2288	2266
61	13	6.5	0.165	0.835	0.000	0.99	0.135	294	9.025	1850	2284	2265
62	7	3.5	0.166	0.834	0.000	1.00	0.068	294	1.051	751	1117	2238
63	4.5	2.25	0.167	0.833	0.000	1.00	0.135	294	1.284	590	879	2268
64	5.5	2.75	0.166	0.834	0.000	0.99	0.135	294	9.150	1863	2296	2265
65	5.75	2.75	0.166	0.834	0.000	1.00	0.135	294	1.473	630	941	2266
66	6.5	5.25	0.166	0.834	0.000	0.99	0.135	294	9.061	1849	2285	2266
68	15	7.5	0.166	0.834	0.000	1.00	0.135	294	9.047	1848	2284	2267
69	16	8	0.166	0.834	0.000	1.00	0.135	294	9.048	1848	2284	2267
70	17	8.5	0.166	0.834	0.000	1.00	0.135	294	9.050	1849	2285	2266
71	18	9	0.166	0.834	0.000	1.00	0.135	294	9.007	1847	2284	2267
72	7	3.5	0.166	0.834	0.000	1.00	0.068	293	1.084	764	1134	2237
73	10	5	0.166	0.834	0.000	0.99	0.068	293	4.981	1978	2394	2235
74	14	7	0.166	0.834	0.000	1.00	0.068	294	4.279	1774	2221	2238
75	10	5	0.166	0.834	0.000	1.00	0.135	294	12.324	2312	2661	2267
76	10	5	0.167	0.833	0.000	1.00	0.135	294	2.039	740	1102	2268
77	11	5.5	0.167	0.833	0.000	1.00	0.135	294	9.040	1843	2282	2269
78	9	4.5	0.180	0.820	0.000	1.10	0.068	294	1.175	785	1174	2281
79	9	4.5	0.167	0.833	0.000	1.00	0.068	294	1.261	827	1219	2238
80	9	4.5	0.166	0.834	0.000	1.00	0.068	294	4.480	1833	2271	2238
81	9	4.5	0.166	0.834	0.000	1.00	0.068	294	4.367	1802	2245	2237
82	14	7	0.167	0.833	0.000	1.00	0.068	295	4.373	1798	2243	2240
83	14	7	0.166	0.834	0.000	0.99	0.135	294	9.024	1848	2284	2266
84	10	5	0.165	0.835	0.000	0.99	0.068	295	4.362	1801	2242	2234
85	10	5	0.166	0.834	0.000	1.00	0.134	295	9.016	1850	2286	2266

86	5	2.5	0.167	0.833	0.000	1.00	0.135	294	1.381	611	911	2269
87	5.5	2.75	0.166	0.834	0.000	1.00	0.136	294	1.446	622	929	2268
88	6	3	0.166	0.834	0.000	1.00	0.134	294	9.117	1867	2301	2268
89	6.25	3.125	0.166	0.834	0.000	1.00	0.135	295	1.560	648	967	2266
90	11	5.5	0.166	0.834	0.000	1.00	0.135	295	9.028	1850	2285	2266
91	11	5.5	0.166	0.834	0.000	0.99	0.135	295	9.045	1853	2288	2265
92	13	6.5	0.166	0.834	0.000	1.00	0.135	295	9.024	1846	2283	2266
93	13	6.5	0.166	0.834	0.000	1.00	0.134	295	8.999	1848	2285	2268
94	9	4.5	0.165	0.835	0.000	0.99	0.135	295	9.041	1855	2288	2264
95	9	4.5	0.167	0.833	0.000	1.00	0.135	295	9.031	1849	2286	2268
96	16	9	0.041	0.205	0.754	1.01	0.135	295	2.418	994	1314	1769
97	18	9	0.040	0.199	0.761	1.00	0.135	295	2.553	1032	1350	1758
98	18	9	0.062	0.306	0.632	1.02	0.135	295	4.991	1534	1837	1899
99	12	6	0.063	0.313	0.624	1.01	0.135	295	2.084	868	1200	1905
100	15	7.5	0.063	0.310	0.628	1.01	0.135	295	9.295	2423	2492	1902
101	16	8	0.063	0.311	0.626	1.01	0.135	295	9.448	2450	2510	1902
102	14	7	0.062	0.311	0.627	1.01	0.135	295	5.394	1621	1909	1901
104	12	6	0.090	0.448	0.462	1.01	0.135	295	6.105	1651	1986	2023
105	10	5	0.091	0.452	0.457	1.01	0.135	295	6.352	1693	2023	2026
106	8	4	0.091	0.451	0.458	1.01	0.135	295	6.330	1691	2020	2025
107	8	4	0.075	0.371	0.554	1.01	0.134	295	1.704	760	1080	1960
108	12	6	0.074	0.368	0.558	1.01	0.135	295	5.647	1622	1934	1958
109	10	5	0.075	0.368	0.557	1.01	0.134	295	1.895	807	1137	1959
110	11	5.5	0.074	0.368	0.558	1.01	0.135	296	1.973	825	1158	1955
111	11	5.5	0.075	0.368	0.557	1.01	0.135	296	2.038	839	1175	1958
112	12	6	0.075	0.371	0.554	1.01	0.135	295	2.062	846	1184	1960
113	13	6.5	0.075	0.369	0.556	1.02	0.134	295	5.609	1618	1931	1960
114	12.5	6	0.074	0.367	0.559	1.01	0.135	296	2.169	872	1212	1956
116	12.25	6.125	0.073	0.364	0.563	1.00	0.135	296	5.587	1619	1927	1951
117	12.25	6.125	0.074	0.367	0.559	1.01	0.134	296	5.599	1620	1931	1955
118	12	6	0.074	0.368	0.558	1.01	0.135	296	5.600	1617	1929	1957
119	14	7	0.074	0.370	0.556	1.00	0.135	295	5.715	1636	1944	1957
120	16	8	0.074	0.368	0.559	1.00	0.135	295	9.475	2382	2495	1955
121	16	8	0.074	0.369	0.557	1.01	0.135	295	10.658	2601	2641	1958
122	17	8.5	0.074	0.368	0.558	1.01	0.134	295	9.606	2409	2515	1956
123	17	8.5	0.075	0.370	0.555	1.01	0.135	295	5.625	1618	1931	1961
124	15	7.5	0.075	0.371	0.554	1.02	0.135	295	5.583	1609	1924	1962
125	11.5	5.75	0.075	0.371	0.554	1.02	0.135	295	5.707	1632	1943	1962
126	11	5.5	0.073	0.366	0.562	0.99	0.135	295	2.048	845	1180	1950
127	11.25	5.625	0.074	0.367	0.559	1.00	0.135	295	1.996	832	1166	1955
128	6	3	0.074	0.367	0.559	1.01	0.135	295	1.462	698	1001	1956
129	4	2	0.075	0.368	0.557	1.01	0.135	295	1.227	637	920	1959
130	15	7.5	0.076	0.372	0.553	1.02	0.068	295	2.744	1585	1905	1942

131	14	7	0.073	0.367	0.561	0.99	0.068	296	2.833	1624	1931	1930
132	13	6.5	0.077	0.375	0.549	1.02	0.067	296	2.773	1595	1916	1946
133	12	6	0.075	0.371	0.554	1.02	0.068	295	5.307	2580	2630	1940
134	12	6	0.076	0.373	0.552	1.02	0.068	295	2.729	1566	1889	1942
135	16	8	0.076	0.373	0.551	1.02	0.068	295	3.313	1811	2087	1942
136	18	9	0.076	0.373	0.551	1.02	0.068	295	2.690	1554	1880	1945
137	10	5	0.075	0.365	0.561	1.03	0.068	296	2.727	1577	1897	1938
138	10	5	0.075	0.365	0.561	1.03	0.068	295	1.311	973	1325	1938
139	12	6	0.076	0.371	0.553	1.02	0.068	295	2.743	1577	1899	1943
140	10	5	0.075	0.368	0.557	1.01	0.134	295	1.943	819	1151	1959
141	8	4	0.075	0.369	0.556	1.01	0.134	296	1.736	768	1089	1959
142	8	4	0.168	0.832	0.000	1.01	0.068	295	5.861	2214	2590	2243
143	9	4.5	0.168	0.832	0.000	1.01	0.068	296	4.412	1803	2248	2241
144	7	3.5	0.168	0.832	0.000	1.01	0.068	296	4.374	1797	2243	2241
145	4	2	0.076	0.369	0.555	1.03	0.068	296	0.880	767	1090	1943
146	6	3	0.072	0.362	0.565	1.00	0.068	296	1.025	844	1179	1926
147	8	4	0.073	0.365	0.561	1.00	0.068	296	2.763	1592	1906	1932
148	10	5	0.075	0.371	0.553	1.01	0.068	295	4.473	2249	2409	1940
149	13	6.5	0.076	0.369	0.556	1.02	0.135	295	2.160	867	1208	1963
150	14	7	0.075	0.368	0.557	1.02	0.134	296	5.620	1621	1933	1959
151	14	7	0.075	0.369	0.555	1.02	0.068	296	2.733	1579	1899	1940
152	14	7	0.075	0.368	0.557	1.02	0.134	296	5.632	1620	1934	1962
153	14	7	0.076	0.371	0.552	1.03	0.069	296	2.911	1629	1943	1945
154	14	7	0.076	0.368	0.557	1.03	0.135	295	6.176	1725	2020	1964
155	14	7	0.076	0.370	0.554	1.03	0.068	295	2.775	1594	1914	1945
208	2	1	0.074	0.370	0.556	0.99	0.067	295	0.584	623	899	1932
209	4	2	0.074	0.370	0.556	0.99	0.067	295	0.792	731	1042	1932
210	6	3	0.074	0.370	0.556	0.99	0.067	295	1.016	840	1175	1932
211	8	4	0.074	0.370	0.556	0.99	0.067	294	1.159	911	1256	1932
212	10	5	0.074	0.370	0.556	0.99	0.067	294	4.167	2168	2347	1932
213	12	6	0.074	0.370	0.556	0.99	0.067	294	2.681	1573	1890	1932
214	9	4.5	0.074	0.370	0.556	0.99	0.067	295	1.281	967	1318	1932
215	7	3.5	0.074	0.370	0.556	0.99	0.067	294	1.029	847	1183	1932
217	11	5.5	0.074	0.370	0.556	0.99	0.067	295	2.666	1567	1885	1932

Table D.2: Initial P_4 and $P_4/2$, mixture conditions, thermodynamic state conditions before and after the passage of the shock wave, and the experimental wave and Chapman – Jouguet detonation velocity for the propane + 10% IPN-oxygen mixtures with varying levels of nitrogen dilution.

			Mole Fraction										
Run	**P_4 (bar)**	**$P_4/2$ (bar)**	**IPN**	**C_3H_8**	**O_2**	**N_2**	**ER**	**P_1 (bar)**	**T_1 (K)**	**P_2 (bar)**	**T_2 (K)**	**V_{exp} (m/s)**	**V_{CJ} (m/s)**
156	10	5	0.017	0.156	0.826	0.000	1.01	0.067	294	4.404	1778	2227	2236
157	8	4	0.017	0.156	0.826	0.000	1.01	0.067	294	4.317	1750	2202	2236
158	7	3.5	0.017	0.156	0.826	0.000	1.01	0.067	294	5.278	2016	2430	2236
159	6	3	0.017	0.156	0.826	0.000	1.01	0.067	294	4.523	1801	2247	2236
160	4	2	0.017	0.154	0.829	0.000	0.99	0.067	294	4.345	1766	2211	2227
162	3	1.5	0.017	0.154	0.829	0.000	0.99	0.067	294	0.839	662	987	2227
163	4	2	0.017	0.154	0.829	0.000	0.99	0.067	294	1.015	728	1082	2227
164	5	2.5	0.017	0.154	0.829	0.000	0.99	0.067	294	1.076	750	1113	2227
165	12	6	0.017	0.154	0.829	0.000	0.99	0.067	294	4.322	1758	2203	2227
166	12	6	0.017	0.154	0.829	0.000	0.99	0.067	294	4.363	1765	2210	2227
167	12	6	0.017	0.154	0.829	0.000	0.99	0.067	294	4.488	1804	2244	2227
168	12	6	0.017	0.154	0.829	0.000	0.99	0.067	294	4.351	1765	2210	2227
169	9	4.5	0.017	0.154	0.829	0.000	1.00	0.067	294	4.335	1759	2205	2228
170	2	1	0.017	0.154	0.829	0.000	1.00	0.134	294	9.117	1821	2260	2258
171	4	2	0.017	0.154	0.829	0.000	1.00	0.135	294	9.595	1887	2316	2258
172	5	2.5	0.017	0.154	0.829	0.000	1.00	0.135	294	9.124	1821	2259	2258
173	8	4	0.017	0.154	0.829	0.000	1.00	0.135	294	9.092	1813	2253	2259
174	9	4.5	0.017	0.154	0.829	0.000	1.00	0.135	294	9.145	1822	2261	2259
175	9	4.5	0.017	0.154	0.829	0.000	1.00	0.135	294	9.127	1819	2259	2259
176	9	4.5	0.017	0.154	0.829	0.000	1.00	0.135	294	9.159	1823	2261	2259
177	5	2.5	0.007	0.069	0.369	0.555	0.99	0.067	294	0.995	823	1155	1935
178	6	3	0.007	0.069	0.369	0.555	0.99	0.067	295	1.068	857	1195	1934
179	7	3.5	0.007	0.069	0.369	0.555	0.99	0.067	294	1.085	865	1204	1935
180	8	4	0.007	0.069	0.369	0.555	0.99	0.067	294	1.217	924	1271	1935
181	9	4.5	0.007	0.069	0.369	0.555	0.99	0.067	295	2.704	1560	1881	1934
182	8	4	0.007	0.069	0.369	0.555	0.99	0.067	294	2.877	1628	1938	1935
183	8	4	0.007	0.069	0.369	0.555	0.99	0.067	294	1.205	921	1268	1935
184	9	4.5	0.007	0.069	0.369	0.555	0.99	0.067	294	1.299	964	1315	1935
185	10	5	0.007	0.069	0.369	0.555	1.00	0.067	294	2.661	1545	1869	1935
186	9	4.5	0.007	0.069	0.369	0.555	1.00	0.067	294	1.272	952	1302	1935
187	9.5	4.5	0.007	0.069	0.369	0.555	1.00	0.067	295	5.526	2650	2673	1935
188	13	6.5	0.007	0.069	0.369	0.555	1.00	0.067	295	2.714	1562	1883	1935

189	13	6.5	0.007	0.069	0.369	0.555	1.00	0.067	295	2.734	1571	1891	1935
190	13	6.5	0.007	0.069	0.369	0.555	1.00	0.067	295	2.718	1561	1882	1935
191	6	3	0.007	0.069	0.369	0.555	1.00	0.134	295	1.499	703	1007	1956
192	8	4	0.007	0.069	0.369	0.555	1.00	0.135	294	1.757	765	1086	1957
193	9	4.5	0.007	0.069	0.369	0.555	1.00	0.134	294	5.734	1624	1935	1956
194	8	4	0.007	0.069	0.369	0.555	1.00	0.134	294	1.725	758	1077	1956
195	10	5	0.007	0.069	0.369	0.555	1.00	0.134	294	1.998	824	1156	1956
196	10	5	0.007	0.069	0.369	0.554	1.00	0.134	294	1.991	823	1155	1956
197	13	6.5	0.007	0.069	0.369	0.554	1.00	0.134	295	5.688	1615	1928	1956
198	11	5.5	0.007	0.069	0.369	0.554	1.00	0.134	295	2.093	847	1183	1956
199	12	6	0.007	0.069	0.369	0.554	1.00	0.134	295	11.299	2694	2701	1956
200	13	6.5	0.007	0.069	0.369	0.555	0.99	0.135	295	1.757	765	1085	1956
201	13	6.5	0.007	0.069	0.369	0.555	0.99	0.135	295	5.704	1616	1928	1956
202	13	6.5	0.007	0.069	0.369	0.555	0.99	0.135	294	5.772	1629	1939	1956
203	11	5.5	0.007	0.069	0.369	0.555	0.99	0.135	294	6.146	1704	2000	1956
204	10	5	0.007	0.069	0.369	0.555	0.99	0.135	294	1.948	811	1141	1955
205	10	5	0.007	0.069	0.369	0.555	0.99	0.135	294	2.016	828	1161	1955
206	15	7.5	0.007	0.069	0.369	0.555	0.99	0.135	294	5.694	1616	1928	1955
207	12	6	0.007	0.069	0.369	0.555	0.99	0.135	294	6.252	1725	2017	1955
218	15	7.5	0.007	0.069	0.370	0.555	0.99	0.067	294	3.846	1544	1868	1945
219	14.5	7.25	0.007	0.069	0.370	0.555	0.99	0.067	295	3.921	1564	1884	1945
220	13	6.5	0.007	0.069	0.370	0.555	0.99	0.067	295	4.192	1641	1948	1945
221	13	6.5	0.007	0.069	0.370	0.555	0.99	0.068	295	3.888	1550	1873	1945